MASTER

Magnetic and electrical properties of soft magnetic FeHfO thin films, and the thin film inductor

Rulkens, B.

Award date:
1997

Eindhoven University of Technology
Department of physics
Group Cooperative Phenomena

Philips Research Laboratories
Eindhoven
Group Magnetism

Magnetic and electrical properties of soft magnetic FeHfO thin films, and the thin film inductor

Bas Rulkens
March 1997

Report of a graduation research project carried out in the group Magnetism of Philips Research Laboratories Eindhoven in a collaboration with the group Cooperative Phenomena at the Eindhoven University of Technology (EUT).

Professor: Prof. Dr. Ir. W.J.M. De Jonge (EUT)

Supervisors: Dr. Ir. P.J.H. Bloemen (Philips Research)
Dr. Ir. H.J.M. Swagten (EUT)

Abstract

In this report the magnetic and electrical properties have been investigated of FeHfO thin films with thicknesses between 0.7 and 10.5 μm prepared by reactive sputtering in an Ar/O_2 mixture at various conditions. The oxygen flow is the most important parameter to adjust the electrical and magnetic properties. The optimal conditions give FeHfO samples with a saturation magnetization B_s of 1.1 T, a (relative) magnetic permeability μ_r at 100 kHz of 1500 and a resistivity ρ of about 1000 μΩcm. The magnetostriction constant λ_s being $5 \cdot 10^{-6}$ is too large to make this material suitable for application as flux guide material in magnetic recording heads. However, films with larger oxygen contents with resistivities near 10^5 μΩcm and permeabilities of approximately 200 are promising to be applied as separation oxide between the flux guide and the MRE in a read head so as to improve the efficiency of the thin film head.

With the HF-permeability set-up which is automatised and optimized during this graduation project, the frequency dependence of the permeability up to 200 MHz is investigated. The roll-off of the permeability of the FeHfO appears to be dominated by ferromagnetic resonance. Furthermore, it is shown that the permeability at low frequencies is caused by both rotation of magnetization and domain wall movements.

The FeHfO films that exhibit good or moderate soft magnetic properties show very small magneto resistance (MR) ratios. FeHfO films prepared with relatively large amounts of oxygen exhibit poor soft magnetic properties but show considerable magnetoresistance probably caused by spin dependent tunneling between Fe grains. It has been shown that the MR ratio of the films change from 2% at room temperature to 7% at 4.2 K, which can be described rather well by simple electrical circuit models assuming that spin dependent tunneling is the basic mechanism including spin-flip scattering processes to account for the strong temperature dependence.

A magnetic transmission line model has been developed to describe a thin film inductor consisting of a conducting coil sandwiched between two soft magnetic layers. It has provided considerable insight on the behaviour of the impedance and inductance as a function of different parameters and dimensions. The main conclusion is that the inductance L is proportional to $\sqrt{\mu}$ rather than to μ for normal coils with magnetic cores. Furthermore, the inductance does not scale with the cross sectional area a^2 but scales with the side length a, caused by the fact that the flux is concentrated near the conductor wires. These conclusions have been confirmed by experiments performed on inductors employing a 0.8 μm thick FeHfO thin film.

Technology assessment

The investigations carried during this graduation project in this report can be seen within the framework of two main fields of application: (1) soft magnetic materials and (2) magnetic field sensors.

(1) The research on soft magnetic materials in general has been motivated by different applications of these materials. In general, they are suitable for applications in the recording industry. In this report we restrict ourselves to the so-called nanocrystalline materials. Recently, FeCuNbSiB was discovered as a nanocrystalline material. These materials attract the attention to application engineers because of the high B_s (FeTaN, FeNbSiN) and can be used as a flux guide (yoke) in for example magnetic heads. High information densities of the tape lead to specified requirements on the write head which should be able to saturate the hard magnetic storage material on the tape: the saturation magnetization M_s and thus the saturation magnetic induction B_s of the flux guide or yoke material of the write head should be large. To obtain a high efficiency to produce flux or to pick up magnetic flux, the permeability should be as high as possible, implying a small magnetic uniaxial anisotropy. FeNbSiN does not show a large resistivity ρ.

On the contrary, FeHfO is one of the materials with a smaller B_s but with a large resistivity. It is composed of bcc-Fe nano-grains in an amorphous phase. The investigation of FeHfO has been motivated primarily by the potential use of this magnetic material as flux guide or core material in magnetic heads. The large resistivity provides a relatively large permeability also at large frequencies. This is a necessity for the application in the magnetic recording of video signals and in hard disk applications.

An important requirement for the use of FeHfO is an as small as possible magnetostriction. This is not only because a large magnetostriction can lead to a too large anisotropy, but also because the tape moving across the head can cause the so-called rubbing noise.

In the regime with large oxygen amounts in the FeHfO, the films exhibit a very large resistivity near 10^5 $\mu\Omega$cm combined with a not too small permeability of about 200. Such FeHfO films might be usable as separation oxide between the flux guide and the magnetoresistance element (MRE) in a read head, which may improve the efficiency of the thin film head enormously.

(2) In magnetic field sensors use is made of the effect of magnetoresistance: the resistance of a material changes by applying a magnetic field. An example of such a sensor is the already mentioned, the MRE. In some materials the giant magnetoresistance (GMR) can be observed, for instance in multilayers consisting of a stack of alternating ferromagnetic and non-magnetic layers, but also in granular systems in which ferromagnetic clusters are dissolved in a non-magnetic matrix. This phenomenon takes place in FeHfO films sputtered with large oxygen flows. Although the permeability is too low for the application in a MRE, this research might be interesting from a fundamental point of view. In particular the study of the spin dependent tunneling mechanism in these systems is extremely relevant for the recently observed tunneling magnetoresistance (TMR) in ferromagnetic layers separated by a insulating barrier, for which application in magnetic field sensors is foreseen in a near future.

Contents

Abstract 2

Technology assessment 3

1. Introduction 6
1.1 Recording principles and materials requirements 6
1.2 This report 9

2. Theory 10
2.1 Introduction 10
2.2 Magnetic anisotropy 10
2.3 Static magnetic permeability 15
2.4 Frequency dependent magnetic permeability 21
2.5 Basic principles of soft magnetic materials 31
2.6 Magnetoresistance (MR) in granular alloys 35
2.6.1 Introduction to giant magnetoresistance (GMR) 35
2.6.2 Origin GMR 35
2.6.3 Tunnelling magnetoresistance (TMR) in granular magnetic films 37
2.6.4 Temperature dependence of MR 39

3. High frequency μ measurements 41
3.1 Introduction 41
3.2 Principle of the measurement 41
3.3 Reflections on the inductance 43
3.4 Measurement procedure 45
3.5 Comparison on the HF and the LF set-up 53
3.6 Conclusions and recommendations 56

4. Other experimental techniques 57
4.1 Introduction 57
4.2 The preparation of FeHfO thin films 57
4.2.1 Reactive sputtering 57
4.2.2 Annealing 59
4.3 Magnetic characterisation 60
4.3.1 BH-loop measurements 60
4.3.2 Magnetostriction measurements 63
4.4 Electrical characterisation 65
4.4.1 Resistivity 65
4.4.2 Magnetoresistance measurements 66
4.4.3 Temperature dependent (magneto)resistance measurements 67
4.4.4 Frequency dependent resistance measurements 67

4.5 X-ray diffraction (XRD) 67

5. Results **69**
5.1 Introduction / experimental 69
5.2 Magnetic and electrical properties of FeHfO thin films 76
5.3 Sputtering parameters and annealing conditions 78
5.4 Technological optimizing 85
5.4.1 Background pressure 85
5.4.2 Rotating field annealing 87
5.4.3 Addition of Cu and Si 88
5.4.4 Application as separation oxide 93
5.5 Frequency dependent permeability measurements 94
5.6 Magnetoresistance and tunneling 100

6. Application: the thin film inductor **110**
6.1 Introduction 110
6.2 Experimental 111
6.3 Relevant properties of the used soft-magnetic layers FeHfO and MnZn-ferrite 112
6.4 Magnetic transmission line modelling 115
6.5 Results and discussion 119

Summary and conclusions **124**

References **125**

Acknowledgement **128**

Appendices **129**

1. Introduction

This report will present an investigation of several magnetic and electrical properties of soft magnetic FeHfO thin films, including the tunneling magnetoresistance and also discusses the application in a thin film inductor. Apart from the latter application this work has been motivated also, or perhaps even primarily, by the potential use of this magnetic material as flux guide or core material in magnetic heads. In order to know which of the magnetic and electrical properties are important to investigate we therefore briefly review the basic principles of this application first. Because almost all materials requirements are the same for an inductor and a magnetic head, a limitation of the discussion to the latter will indeed suffice. The theory and application of a soft magnetic film in an inductor will be discussed extensively in chapter 6.

1.1 Recording principles and materials requirements

In Fig. 1.1(a) a schematized representation of a *sandwich video head* [1] is given. Essentially it consists of three parts: the yoke (or core), the coil and the gap. The yoke is made of a soft ferromagnetic material which conducts the magnetic flux. The different processes of recording are also indicated very schematically in Fig. 1.1(b). A write head and a read head are shown together with a moving tape coated with a magnetizable material .

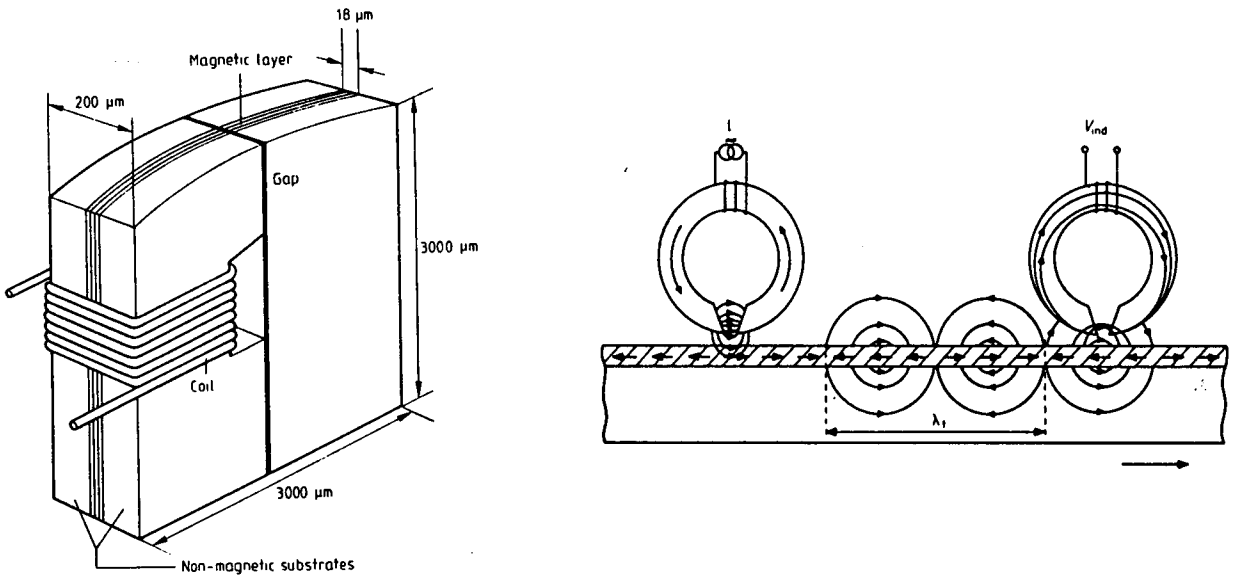

Fig. 1.1 (a) Sandwich video head. (b) Magnetic recording: writing and reading process with a tape recorder on a moving tape [1].

In case of *writing* a signal current through the coil generates a magnetic field which via a fluxguide at the gap, is permitted to fringe out and intercept the recording medium so as to produce a magnetization in the tape. Since the density of the information recorded on the tape

has been increased over the last years, this has led to severe requirements on both tape and recording head. If the storage capacity grows and consequently the size of the domains decreases, the demagnetizing field of adjacent domains magnetized in the opposite sense in the tape increases. It may be clear that, to prevent demagnetization of written domains, the demagnetizing field should be balanced by a sufficient coercive field H_c. This implies that a high information density requires a high value of the coercivity: the storage medium should be hard magnetic. This leads to specified requirements on the write head which should be able to saturate the hard magnetic storage material on the tape. Consequently, the saturation magnetization M_s and thus the saturation magnetic induction B_s of the flux guide or yoke material of the write head should have a high enough value to generate fields larger than H_c.

Mostly the same head is also used for the *reading* process in which fringing fields emanating from the domains in the moving magnetic tape will be guided via the yoke towards the coil and cause an induction voltage V_{ind}. Another requirement is that the efficiency to produce flux or to pick up magnetic flux should be as high as possible (Fig. 1.2).

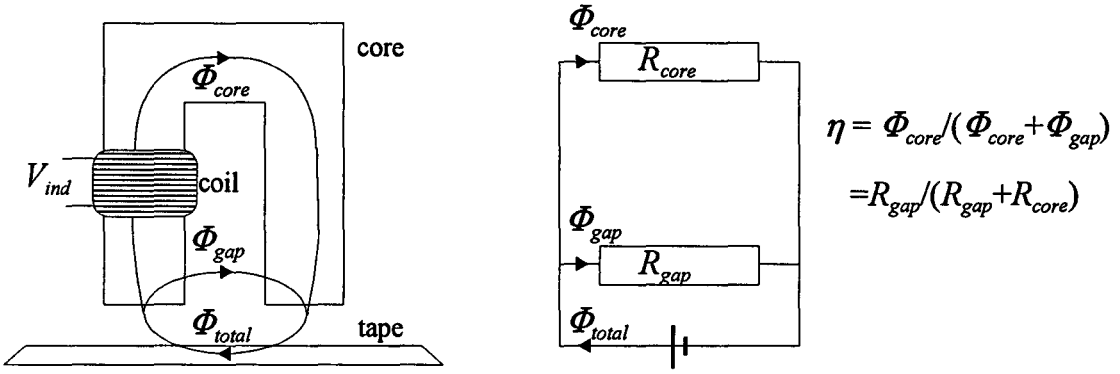

Fig. 1.2 Efficiency η of a magnetic head.

The reading efficiency η is defined as the ratio of the core flux Φ_{core} that crosses the coil and the total flux Φ_{total}. The latter consists of the flux that crosses the gap Φ_{gap} and that passing through the core Φ_{core}, see Fig. 1.2.

$$\eta=\frac{\Phi_{core}}{\Phi_{total}}=\frac{\Phi_{core}}{\Phi_{core}+\Phi_{gap}}=\frac{R_{gap}}{R_{gap}+R_{core}}. \tag{1.1}$$

Here, R_{gap} is the magnetic reluctance (resistance) of the gap and R_{core} is the magnetic reluctance of the core (flux guide). The definition of the magnetic reluctance R_m of a material having (relative) permeability μ_r is:

$$R_m=\frac{l}{\mu_0\mu_r A}. \tag{1.2}$$

Here, l is the path length which the flux has to traverse and A the cross sectional area. Eq. (1.2) can be seen as the magnetic analog of the electrical resistance of a piece of material: the permeability plays the role of the conductivity. As can be seen from Eq. (1.1) and Eq. (1.2) a high efficiency means that the magnetic resistance of the flux guide R_{core} should be small compared to the gap resistance. This implies a high permeability of the core or flux guide material.

As we will see later on, to obtain a high permeability it is necessary that some magnetic uniaxial anisotropy is present. This is because a non-zero anisotropy promotes a well defined domain structure so that use is made of the rotational permeability mechanism instead of the wall permeability mechanism. Wall permeability contributions should be avoided since they decrease much more steeply with frequency so that it is difficult to obtain a reasonable permeability at high frequencies. This is important, because high frequencies correspond to high data rates in the magnetic recording of video signals and in hard disk applications. As we will see later on this also means that in the case of rotational permeability a high electrical resistance is desirable. Furthermore, the uniaxial anisotropy should be relatively small, so that the spins are able to rotate almost freely which means that the direction of magnetization is susceptible to small tape fields, corresponding to a high permeability.

To get good soft magnetic material it is obvious that also a low remanence is required, otherwise unwanted stray fields would obstruct the reading process. Regarding a desirable high permeability, the coercivity H_c of the yoke must also be small. Otherwise it is possible that inner magnetization loops cause a smaller permeability. This aim also provides low hysteresis losses.

Furthermore, the flux guide material must have a low magnetostriction. This is necessary because unavoidable internal stresses within the magnetic head in combination with magnetostriction gives rise to magneto elastic anisotropy contributions leading to a decrease of the permeability, or to an undesired domain structure which, as we have mentioned, decreases the permeability at higher frequencies. A second reason for an as small as possible magnetostriction is that magnetostriction causes the electrical output to be coupled to vibrations set up by the tape moving across the head, which results in the so-called rubbing noise. We mention that during recording and play back the head is in direct contact with the tape.

In summary the most important requirements for fluxguide materials are in case of a *read head:*

- a high permeability μ,
- a high permeability also for high frequencies, implying a high electrical resistivity ρ,
- a not too small uniaxial magnetic anisotropy K_u,
- a low coercivity H_c,
- a low saturation magnetostriction λ_s.

For the *write head* the same requirements apply, but there is an extra requirement viz.:

- a high value of saturation magnetization M_s.

1.2 This report

Examples of well-known soft magnetic materials that are being used nowadays as flux guide or yoke materials are $Ni_{80}Fe_{20}$, $Co_{87.5}Nb_{9.5}Zr_{3.0}$ and $Fe_{80}Ta_{10}N_{10}$. Although these materials meet the requirements mentioned above to a satisfactorily degree regarding current applications, they all exhibit a relatively low resistivity varying between 24 μΩcm for NiFe to 130 μΩcm for CoZrNb. As mentioned, in future higher data rate applications a high resistivity would be desirable.

Recently, a new class of soft magnetic materials, so-called granular alloys of the type Fe-TM-O (TM=transition metal) have been discovered that are promising in this respect [2-11]. They exhibit much larger electrical resistivities, which is adjustable by varying the oxygen content. Since these are fairly unknown materials, a lot of research is still necessary. This thesis will report the investigations of one example of these granular alloys, namely FeHfO. It may be clear that emphasis is put on the study of magnetic properties relevant to application. However, magnetoresistance phenomena receive also attention since these are expected to contribute also to the understanding of the behaviour of granular alloys in general. This report reflects the work performed within a graduation research project carried out in the group Magnetism of Philips Research Laboratories Eindhoven in a collaboration with the group Cooperative Phenomena at the Eindhoven University of Technology. The structure of this report is as follows: Chapter 2 describes the necessary theoretical background about magnetic anisotropy, and in more detail about the magnetic permeability. Furthermore, because of the aim for high frequency applications, it is a necessity to measure at frequencies higher than was possible with the existing magnetic permeability set-up (10 kHz - 13 MHz). Therefore chapter 3 describes the set-up for magnetic permeability measurements up to 200 MHz. The complications accompanying the extensions of the frequency range will be discussed. In chapter 4 the preparation technique of the FeHfO thin films, and the experimental techniques which have been used to characterize the films will be discussed. The results are presented in chapter 5, including the optimizing of sputtering and annealing conditions, including the effect of additions of small amounts of other elements (Cu and Si). Furthermore, the frequency dependent magnetic permeability and resistivity receives attention. Finally, the tunnel-type GMR results will be discussed in this chapter. The temperature dependent MR ratio will be modelled with simple equivalent circuits. In chapter 6 the application of FeHfO layers in a thin film inductor will be discussed. Some impedance measurements as well as (transmission line model) calculations as a function of permeability and other (dimensional) parameters will be presented there. The final chapter will review the results, summarize the conclusions and give recommendations for future research.

2. Theory

2.1 Introduction

In this thesis primarily soft magnetic materials will receive attention for reasons mentioned in chapter 1. The present chapter will describe the most important theoretical issues that are needed to understand this report. Magnetic anisotropy is the phenomenon that the direction of the magnetization is aligned parallel to certain preferential axes (easy axes). This will be discussed in section 2.2. Both magnetic anisotropy and the domains will influence the magnetization process. The reason to discuss this is that the anisotropy and the magnetization process determine the permeability. Section 2.3 discusses the magnetization process in the case of static magnetic fields whereas in section 2.4 the case of time dependent fields is treated. The frequency dependence of the magnetic permeability, particularly the effect of eddy currents and ferromagnetic resonance will be considered. In section 2.5 the physics of the soft magnetic materials, especially the so-called *nanocrystalline* materials like FeHfO, the core of this report, will be discussed. In section 2.6 the theoretical background concerning magnetic field dependent resistance and more precisely tunneling and the giant magnetoresistance (GMR) is presented.

2.2 Magnetic anisotropy

According to the Heisenberg model, the quantum mechanical exchange interaction between two atoms i, j bearing electron spins S_i en S_j is written as

$$E_{ex} = -J\vec{S}_i \cdot \vec{S}_j = -J|\vec{S}_i||\vec{S}_j|\cos\psi, \qquad (2.1)$$

where J is the exchange integral which is related to the overlap of the charge distributions of the atoms i, j and ψ is the angle between the spin directions. The sign of the exchange integral is positive for ferromagnets, zero for paramagnets and negative for antiferromagnets. From Eq. (2.1) it is obvious that for ferromagnets in the parallel spin configuration the energy is minimal. The exchange energy is a very strong interaction, which by definition is present in ferromagnets and opposes changes in the relative directions between adjacent spins. It plays a role in domain walls, where these relative directions are non-zero ($\psi \neq 0$), and also causes averaging effects of locally varying magnetic properties. We will come back to this important point in section 2.5. Besides this pure isotropic exchange interaction there is an energy in a ferromagnetic crystal which directs the magnetization along certain preferential axes, which is called magnetic anisotropy. In general, this anisotropy energy contains four different contributions:

a) the magnetocrystalline anisotropy,
b) the shape anisotropy,
c) the magneto elastic anisotropy and
d) the field induced anisotropy.

We shall now briefly discuss the different contributions.

a) Magnetocrystalline anisotropy

In a cubic crystal like iron, for example, the cube edges [100], [010] and [001] are the directions of easy magnetization, while the body diagonals [±1±1±1] are hard axes. Its origin arises from spin-orbit coupling. Because of the Coulomb-Coulomb repulsion between orbitals of neighbouring atoms, the orientation of these orbitals is related to the crystal lattice, and thus dependent on crystallographic directions. Fig. 2.1 shows two situations illustrating the relation between magnetization or spin direction indicated by the arrows and the orientation of the orbitals.

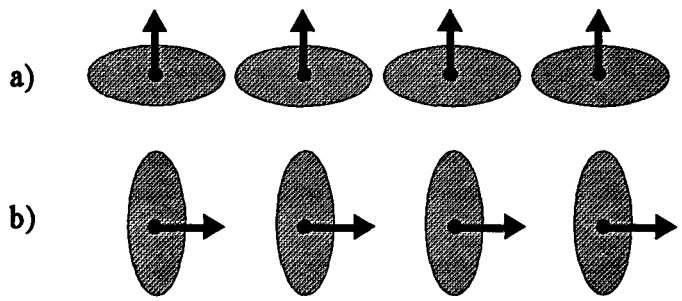

Fig. 2.1 Origin of magnetocrystalline anisotropy. The figure depicts the case of an infinitely strong spin-orbit interaction. The exchange energy and the electrostatic interaction energy of the charge distributions of neighbour atoms is different for the case that the magnetization points upwards, situation (a) compared to situation (b) in which the magnetization points to the right. Hence there exists a magnetic anisotropy energy.

From this figure it follows that the overlap of the electron clouds of neighbouring atoms is different for the case that the magnetization points upwards (Fig 2.1a) compared to the situation (Fig.2.1b) in which the magnetiztion points to the right. This leads to a different exchange energy and electrostatic energy for both situations, resulting in a magnetic anisotropy energy.

The energy of the magnetization as a function of its direction i.e. the crystalline anisotropy energy of Fe is expressed in so-called direction cosines α_1, α_2 and α_3 referred to the cube edges. A phenomenological expression can be derived making use of the cubic symmetry. Since opposite ends of a crystal axis are equivalent magnetically, the crystalline anisotropy must be an even power of each α_i. Moreover, it has to be invariant under exchanges of the α_i among themselves. Because $\alpha_1^2+\alpha_2^2+\alpha_3^2=1$, the lowest order non vanishing term is of the fourth degree. Mostly it is sufficient to express this anisotropy energy per unit of volume as

$$E_K=K_1(\alpha_1^2\alpha_2^2+\alpha_2^2\alpha_3^2+\alpha_3^2\alpha_1^2)+K_2\alpha_1^2\alpha_2^2\alpha_3^2, \qquad (2.2)$$

where K_1=42 kJ/m^3 and K_2=15 kJ/m^3 are the cubic anisotropy constants for Fe at room temperature [12].

b) Shape anisotropy

In samples with uniform magnetization, magnetic poles on the surface give rise to a demagnetizing field $\vec{H}_d$ which is proportional and opposite to the uniform magnetization $\vec{M}$:

$$\vec{H}_d = -\vec{N}\cdot\vec{M}. \tag{2.3}$$

Here $\vec{N}$ is the demagnetizing tensor which depends on the shape of the sample and, in general, on the position in the sample. The shape anisotropy energy per unit of volume can be expressed as

$$E_d = -\frac{1}{2}\mu_0\vec{M}\cdot\vec{H}_d = \frac{1}{2}\mu_0\vec{M}\cdot\vec{N}\cdot\vec{M}. \tag{2.4}$$

In this equation $\mu_0 = 4\pi\cdot 10^{-7}$ N/A^2 is the permeability of vacuum. In Eq. (2.4) we assumed no dependence of the position in $\vec{N}$. The tensor can only be calculated exactly for spheres, thin films and ellipsoids. For spheres, for instance, the tensor is diagonal with elements $N_x = N_y = N_z = 1/3$. In case of a thin film with infinite dimensions and the normal on the surface parallel to the z-axis, the tensor is diagonal with elements $N_x = N_y = 0$ and $N_z = 1$. For more realistic films (Fig. 2.2) one must take into account the finite dimensions in the x- and y-directions. However, $N_x + N_y + N_z = 1$ always holds.

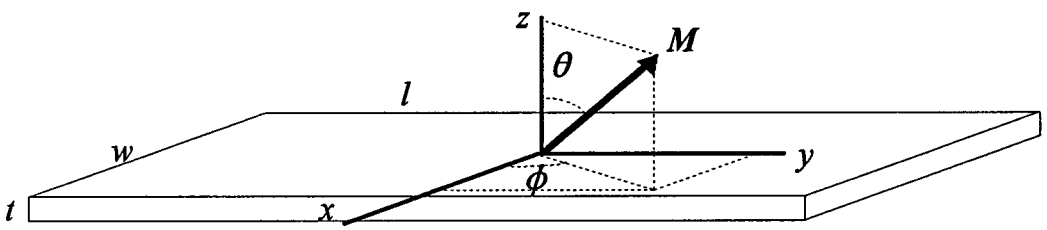

Fig. 2.2. Magnetization in a thin film with length l, width w and thickness t represented in spherical coordinates.

In this case the shape anisotropy given by Eq. (2.4) can be rewritten and becomes in spherical co-ordinates

$$E_d = -\frac{1}{2}\mu_0 M_s^2[(N_z - N_x) + (N_x - N_y)\sin^2\phi]\sin^2\theta, \tag{2.5}$$

Here, the angles ϕ and θ are defined in Fig. 2.2 and constant energy contributions are neglected, because they will not give rise to anisotropy. For a film with length l, width w and thickness t satisfying $l > w >> t$ this means that $N_y < N_x << N_z$. This is because free poles appear on the very narrow edges of the film, hence demagnetizing fields in the plane will be very

weak. Consequently, in equilibrium the magnetization will be orientated along the y-axis. For the film infinitely extended in the x- and y-directions Eq. (2.5) becomes rather simple and can be written as

$$E_d = K_d \sin^2\theta \tag{2.6}$$

with an uniaxial anisotropy constant $K_d = -1/2\mu_0 M_s^2$, which for $\mu_0 M_s = 1.0$ T is about -400 kJ/m^3. This expresses more clearly that the magnetization is preferably orientated along the film plane (θ=90°).

c) The magneto elastic anisotropy

If a magnetic material is magnetized, for example by applying a magnetic field it often has the property to change dimensions during the magnetization process. The length change caused by a magnetic field divided by its original length is characterized by the so-called magnetostriction constant λ. Because this parameter depends on the applied field, one is mostly interested in the length change at saturation λ_s. The origin again arises from spin-orbit interaction (Fig. 2.3).

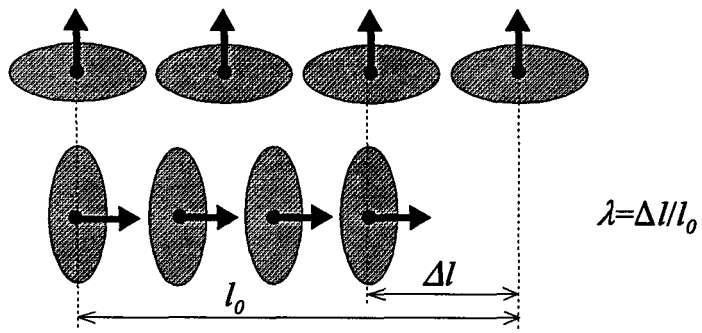

Fig. 2.3 Simplified picture of magnetostriction in a ferromagnetic material. Because of their own magnetic moments the charge distributions are ellipsoidal instead of spherical. The individual moments will be directed parallel to the applied field. Consequently, the distances between the atomic centres will change with field orientation, which results in enlarging or shrinking of the material.

When a field is aplied the individual magnetic moments will be directed parallel to the applied field. Because of the ellipsoidal charge distribution, the distances between the atomic centres will change with field orientation. This means that the material enlarges or shrinks.

The inverse effect also occurs if one applies a stress, the orbitals reorient and cause by spin-orbit coupling the magnetization e.g. to rotate to another more preferable direction. The latter is the magneto elastic anisotropy contribution: the preferential direction depends on the direction of the stress.

In general λ_s is a tensor, but in nanocrystalline materials λ_s reduces to a scalar when no texture is present. In the case that an uniaxial stress σ is applied, the magneto elastic energy can be written as [13]:

$$E_\lambda = \frac{3}{2}\lambda_s \sigma \sin^2\psi, \tag{2.7}$$

where ψ is the angle between the magnetization direction and the stress axis. It is clear that the preferential direction depends on the sign of both λ_s and σ. If the product is positive then there will be an easy axis for ψ=0° as distinct from the case when the product is negative, resulting in an energy minimum for ψ=90°. Again, this anisotropy contribution is an uniaxial energy with anisotropy constant $K_\lambda = 3/2\lambda_s\sigma$. If for instance $\lambda_s = 1\cdot10^{-6}$ and σ=100 MPa, this contribution can be as large as 150 J/m^3. If the stresses in the material are isotropic, the above considerations will not lead to any anisotropy. Only when the stresses in different directions are not the same, this will result in anisotropy. To diminish this anisotropy contribution in applications it is important to reduce the magnetostriction and the stresses in the material.

d) Field induced magnetic anisotropy

In the presence of a magnetic field during annealing it is possible to induce a preferential axis in a material, which is believed to be caused by the rearranging of atoms in pairs. The random distribution is then disturbed and the pairs will be directed with their axis parallel to the field direction (e.g. the x-direction). After the annealing treatment the pairs have been frozen in and act as easy or hard axis for the magnetization, which again results in an uniaxial energy:

$$E_{ind} = K_{ind}\sin^2\phi. \tag{2.8}$$

Here, ϕ is the angle between the pair orderening axis and the magnetization. Typical values for the field induced uniaxial anisotropy K_{ind} can be a few hundreds J/m^3.

Apart from the magnetostriction contribution, the field induced anisotropy is rather small compared to the anisotropy contributions mentioned above. This is important in connection with a high magnetic permeability. As will be discussed in section 2.5, the magnetocrystalline anisotropy will be averaged out as much as possible in nanocrystalline alloys. Moreover, if the shape anisotropy and magneto elastic anisotropy of the thin films are very small, the only remaining anisotropy is the induced anisotropy, which is more or less controllable and can be very small. As will be clear from the next section, this can result in a large magnetic permeability.

2.3 Static magnetic permeability

The relation between the magnetic induction with magnitude B and the magnetization with magnitude M defines the permeability μ by

$$B=\mu_0(H+M)=\mu_0(1+\chi)H=\mu_0\mu_r H=\mu H. \tag{2.9}$$

Here, H is the magnitude of the magnetic field, χ is the susceptibility, and μ_r is the relative permeability. For materials with $\chi\neq 0$ or $\mu_r\neq 1$, this implies that an applied field will cause a magnetization. In general the permeability is field dependent as can be seen from the hysteresis loops. In this section static fields in relation to the permeability will be considered, while in section 2.4 a review of the magnetic permeability in relation to frequency dependent fields will be given. Two major mechanisms which contribute to the magnetization process, and more in particular the permeability, will be described in this section: reversible *rotation of magnetization* and *domain wall displacements*.

a) Rotation of magnetization

In a ferromagnetic material the domain magnetization will be directed along the easy axis. When a static magnetic field is applied perpendicular to this preferential direction i.e. along the hard direction the magnetization will rotate away towards the hard direction until it is orientated parallel to it.

Let us consider a single domain with a certain easy axis in a magnetic field. The total energy E_t of this domain is the sum of the field energy E_f and the magnetic anistropy energy E_K

$$E_t=E_f+E_K=-\mu_0 M_s H\cos(\phi_H-\phi_M)+K_u\sin^2\phi_M, \tag{2.10}$$

per unit of volume, where ϕ_H is the angle between the easy axis and the direction of the magnetic field H (Fig. 2.4), K_u is the constant of uniaxial anisotropy and ϕ_M is the angle between the easy axis and the magnetization direction. The magnetization M in the field direction is now given by $M=M_s\cos(\phi_H-\phi_M)$ in the field direction.

Fig. 2.4 Rotation of magnetization in a single domain.

The stable direction of magnetization can be determined by minimizing this energy with respect to ϕ_M. In the case where the applied field is perpendicular to the easy direction (ϕ_H=90°), one can calculate that with increasing field the magnetization $M=M_s\sin\phi_M$ changes from zero to the

maximum value M_s in a linear fashion and that saturation is reached at the anisotropy field $H_K=2K_u/\mu_0 M_s$ when all magnetic moments are parallel to the hard axis. Fig. 2.5 shows the magnetization process as function of the applied field. Of course, minimizing Eq. (2.10) can also be done for angles ϕ_H different from 90°. In general this yields magnetization curves that are not straight lines.

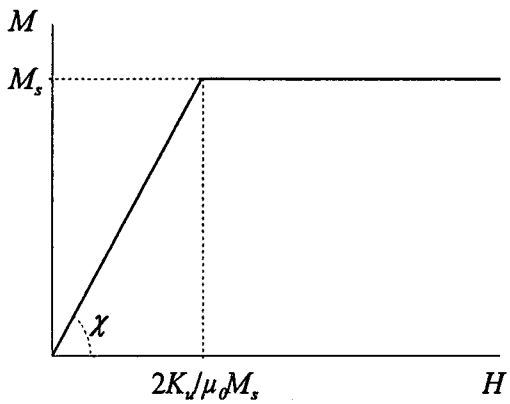

Fig.2.5 Magnetization curve with the applied field along the hard axis direction caused by rotation of magnetization from the easy axis towards the hard axis.

The slope of the *M-H* curve represents the susceptibility χ. So the (relative) rotational permeability $\mu_{r,\,rot}=1+\chi$ can be written in the case of Fig. 2.5 as

$$\mu_{r,\,rot} = 1+\chi = 1+\frac{\partial M}{\partial H} = \frac{M_s}{2K_u/\mu_0 M_s} = 1+\frac{\mu_0 M_s^2}{2K_u}. \qquad (2.11)$$

This is the contribution to the magnetic permeability in case of rotation of magnetization from an easy axis to the hard axis, when the field is applied perpendicular to the easy axis (ϕ_H=90°). A more general expression has been derived for angles ϕ_H different from 90° in appendix A, with the following result:

$$\mu_{r,\,rot}=1+\frac{\mu_0 M_s^2}{2K_u}\sin^2\phi_H. \qquad (2.12)$$

This equation is only valid for weak magnetic fields ($H << K_u/\mu_0 M_s$), due to the fact that in this case the permeability depends on the field, which is distinct from the situation that the applied field is orientated perpendicular to the easy axis. As is clear from Eq. (2.13) the permeability is largest for applying a field in the hard axis direction and becomes unity for fields along the easy axis.

In the above equations, the anisotropy K_u is in general an effective anisotropy composed of the contributions discussed in the previous section: $K_u=K_{ind}+3/2\lambda_s\sigma-1/2\mu_0 M_s^2 \cdot N$. Often μ is corrected for the shape contribution since the latter is not a material dependent property. An alternative way of correcting for the shape anisotropy than by subtracting it from K_u and calculate the intrinsic anisotropy $K_i=K_{ind}+3/2\lambda_s\sigma$ to recalculate μ is to consider the effective internal field H_i in a magnetic sample, which is given by the sum of the applied magnetic field H_a and the demagnetizing field $H_d=-NM$ caused by poles on the edges:

$$H_i=H_a-NM=H_a-N\chi_i H_i. \tag{2.13}$$

Fig. 2.6 shows the resulting magnetization curve due to this field.

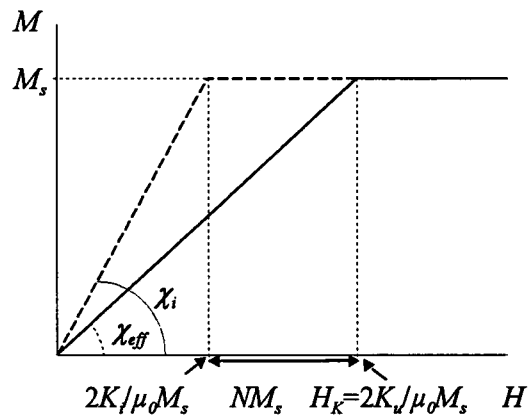

Fig. 2.6 Magnetization corrected for demagnetization.

From this figure it follows that there has to be corrected for the demagnetizing field to know the intrinsic susceptibility χ_i (or permeability).

$$\chi_i=\frac{\partial M}{\partial H}=\frac{M_s}{H_K-NM_s}=\frac{M_s}{\frac{2K_u}{\mu_0 M_s}-NM_S}=\frac{\frac{\mu_0 M_s^2}{2K_u}}{1-N\frac{\mu_0 M_s^2}{2K_u}}=\frac{\chi_{eff}}{1-N\chi_{eff}}. \tag{2.14}$$

Here χ_{eff} is the susceptibility that will be measured in an experiment. Because $\mu_r=1+\chi$ it is obvious that for ferromagnetic materials with high permeabilities it is also permissible to write for the intrinsic relative permeability $\mu_{r,i}$.

$$\mu_{r,i}=\frac{\mu_{eff}}{1-N\mu_{eff}}. \tag{2.15}$$

As can be seen from Fig. 2.6 it is clear that the factor of demagnetization can have much influence on the magnetic permeability and the magnetization curve, particularly for large μ_r. For a detailed discription of the mechanism of the magnetization process see Stoner *et al.* [14].

b) domain wall displacement

Eq. (2.13) suggest that the magnetic permeability measured in the easy-axis direction is unity. This is not true in practice: Eq. (2.13) was derived for the rotation magnetization process, whereas in a ferromagnet also another magnetization process contributes to the magnetic permeability, viz. domain wall displacement. This section focuses on this contribution and shows that this is maximal along the easy axis. If all magnetization vectors in a magnetic material would be directed parallel and along the (in-plane) y-direction (see Fig. 2.7(a)), a high magnetostatic energy $1/2\mu_0 M_s^2(N_y-N_x)$ would be build up by means of poles. To avoid this, the ferromagnetic material displays the phenomenon to subdivide its magnetization in domains with different magnetization directions (see Fig. 2.7(b)). The magnetic energy outside the sample is reduced because of the reduced spatial extension of the field outside the film. In Fig. 2.7(c) the magnetostatic energy E_d is even zero. The boundaries of the triangular domains in this case make angles of 45° with the magnetization of the domains, so that the component of the magnetization nomal to each boundary is continuous across the boundary (E_d=0). Because the flux closes inside the crystal, these triangular domains are *closure domains*.

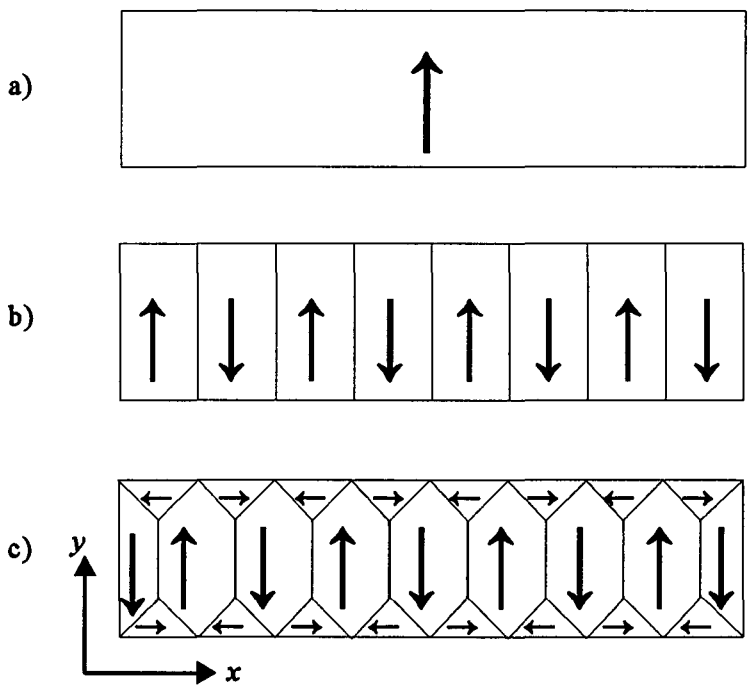

Fig. 2.7. Top view of the a magnetic film displaying three types of domain patterns..

The latter case is the most common situation encountered. Returning for a moment to the rotational permeability as measured in the x-direction, it is clear that in Eq. (2.15) and Eq. (2.16) the demagnetizing factor N equals N_x and not N_x-N_y as suggested by Eq. (2.5). This is because no poles are formed at the edges of the film in the width (y) direction if one measures the permeability (applies a field) in e.g. the x-direction.

The domains are separated by a transition area in which the direction of magnetization changes gradually. The thickness of such a domain wall is determined by the balance of the exchange energy and the anisotropy energy. In iron the thickness of a so-called 180° domain wall, where the magnetization changes from parallel to antiparallel, is 55 nm [15]. Figure 2.8 shows the domain structure with a 180° domain wall.

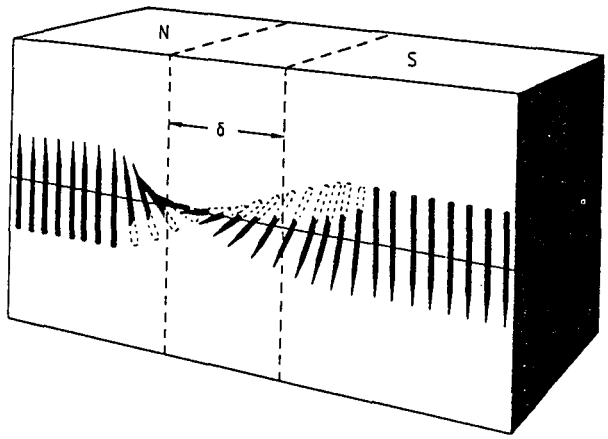

Fig. 2.8 Domain structure of a ferromagnetic material showing two domains separated by a 180° domain wall of thickness δ [12].

Let us consider the displacement of a wall in a non-uniform material. In the absence of a field, the wall will be positioned at s_0, which is a local minimum in the energy (Fig 2.9).

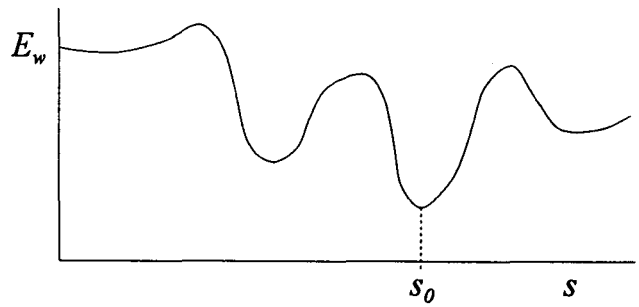

Fig. 2.9 Domain wall energy as a function of position.

In first approximation the energy of a wall with area A near this minimum displaced to s can be expressed as

$$E_w=\frac{1}{2}\alpha_w(s-s_0)^2A. \qquad (2.16)$$

If this displacement is the result of a magnetic field that is applied, with a direction making an angle ϕ_H with the magnetization in the domain, the corresponding change in field energy is given by:

$$E_H = -2\mu_0 M_s H \cos\phi_H A(s-s_0) \tag{2.17}$$

for a 180° domain wall, because by wall displacement the magnetization will change from $+M_s\cos\phi_H$ to $-M_s\cos\phi_H$, in the region $[s_0, s]$ where the wall passes, see Fig. 2.10.

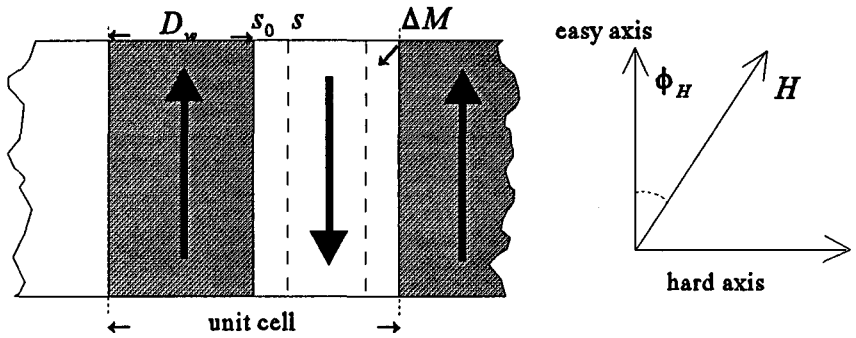

Fig. 2.10 Domain wall movements.

After minimizing the total energy E_w+E_H with respect to the the displacement $s-s_0$ of equilibrium position of the wall becomes

$$s-s_0 = \frac{2\mu_0 M_s \cos\phi_H}{\alpha_w} H. \tag{2.18}$$

As a result of this, the magnetization in a unit cell with volume $A \cdot D_w$ as indicated in Fig. 2.10 increases by $\Delta m = 2\mu_0 M_s \cos\phi_H (s-s_0) \cdot A \cdot 2D_w$ with $2D_w$ the size of a domain repetition period in the hard axis direction. This results in a (relative) wall permeability $1+\Delta m/(H \cdot A \cdot D_w)$:

$$\mu_{r,\,wall} = 1 + \frac{4\mu_0^2 M_s^2 \cos^2\phi_H}{\alpha_w D_w}. \tag{2.19}$$

From Eq. (2.19) it is clear that the wall permeability is maximal for a field applied along the easy axis and at a minimum for fields in the hard axis direction. This is exactly the opposite to the case of magnetization rotation. The general case of the permeability will be a combination of wall permeability and rotation permeability so that the angular dependence of the magnetic permeability can be described by:

$$\mu_r = 1 + \mu_{r,\,wall}\cos^2\phi_H + \mu_{r,\,rot}\sin^2\phi_H \tag{2.20}$$

with $\mu_{r,\ wall}$ and $\mu_{r,\ rot}$ the wall and rotational permeability contributions, respectively. Both processes are indicated again schematically in figure 2.11.

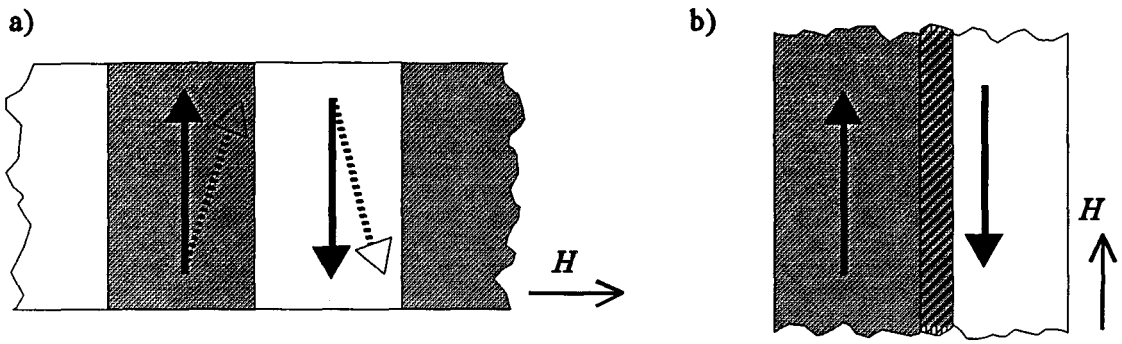

Fig. 2.11 (a) Rotation of the magnetization and (b) domain wall displacement.

2.4 Frequency dependent magnetic permeability

Until now, static magnetic fields were regarded in the magnetization process and more in particular the magnetic permeability. However, in industrial research one is often interested in high-frequency applications. The response of the magnetization of a ferromagnetic material to frequency dependent (or time dependent) magnetic fields can be completely different from the static situation discussed in section 2.3. At low frequencies the magnetization or the magnetic induction $b(t)$ is able to follow a time dependent magnetic field $h(t)=h_0\cos\omega t$, whereas for high frequencies the induction can not follow the applied field due to several loss mechanisms which will be discussed in this section. An example of what may occur is schematically depicted in Fig. 2.12.

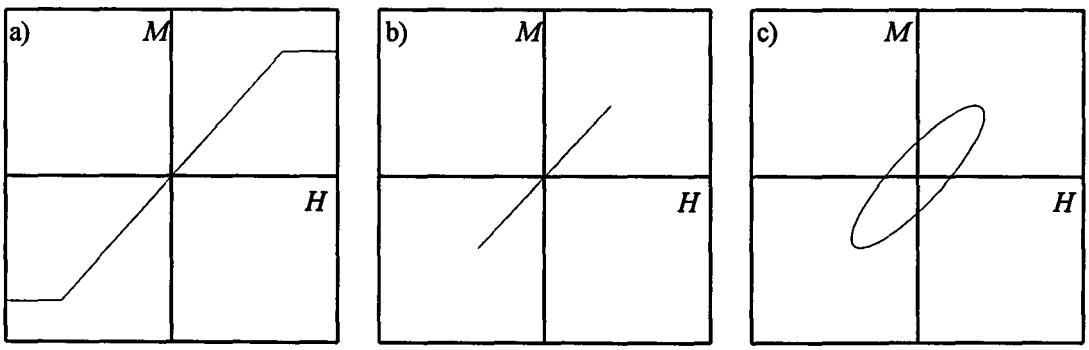

Fig. 2.12. Schematic magnetization process in case of (a) DC-field, (b) a small amplitude AC-field for low frequencies and (c) a AC-field for high frequencies.

Figure 2.12(a) depicts the magnetization process in case of a DC-field as already discussed extensively in section 2.3. Low frequency AC-fields give for both the magnetic field and the magnetic induction harmonic fields proportional with $\cos\omega t$. For large frequencies with a time dependent applied field $h(t)=h_0\cos\omega t$, the magnetic induction $b(t)$ in general displays a phase shift relative to $h(t)$ and can be written as:

$$b(t)=b_0\cos(\omega t-\varepsilon)=b_0\cos(\omega t)\cos\varepsilon+b_0\sin(\omega t)\sin\varepsilon, \tag{2.21}$$

Here ε is the magnitude of the phase delay of the magnetic induction. If we define $\mu'=b_0/\mu_0 h_0\cdot\cos\varepsilon$ and $\mu''=b_0/\mu_0 h_0\cdot\sin\varepsilon$, Eq. (2.21) becomes

$$b(t)=\mu_0\mu' h_0\cos\omega t+\mu_0\mu'' h_0\sin\omega t \tag{2.22}$$

Eliminating the time parameter t when combining $h(t)=h_0\cos\omega t$ and Eq. (2.22) yields an ellips as depicted in Fig.2.12(c). When using the convenient complex notation, Eq. (2.22) becomes:

$$\hat{b}(t)=\mu_0\hat{\mu_r}\hat{h}(t), \tag{2.23}$$

where $\hat{h}(t)=h_0\exp(j\omega t)$ and the *complex* (relative) permeability $\hat{\mu_r}$ is defined by

$$\hat{\mu_r}=\mu'-j\mu''. \tag{2.24}$$

From Eq. (2.22) or (2.23) combined with Eq. (2.24) it is clear that μ' determines the magnitude of the component of the magnetic induction in phase with the field, whereas μ'' determines the magnitude of the component which is delayed by $\pi/2$, i.e. the out of phase component of the magnetic induction. The latter part describes the magnetic energy losses (dissipation) in the material.

So far only a phenomenological relation between the energy losses in a magnetic material and its permeability was discussed. Two main loss mechanisms are important in the description of the (complex) frequency dependent permeability. An important loss mechanism in magnetic materials is related to the occurence of so-called *eddy currents*. A second possible contribution to the energy losses is *ferromagnetic resonance*, which essentially is absorption of electromagnetic radiation by the precessing magnetic moments. Both mechanisms suppress the rotational permeability as well as the wall permeability. We shall discuss both loss terms and start the discussion for the case of rotational permeability.

a) Eddy currents

At high frequencies the magnetic field $h(t)$ in a magnetic material is screened by eddy currents, which are generated, obeying Lenz's law: The currents will flow in a manner that flux changes are opposed, see Fig. 2.13. Consequently, the induced magnetization in the material will be less and thus the magnetic permeability will be smaller. It may be clear that the time derivative of the flux is larger for larger frequencies and that thus the degree of suppression of the permeability will be frequency dependent and larger for higher frequencies, which means that the magnetic permeability will decrease with frequency.

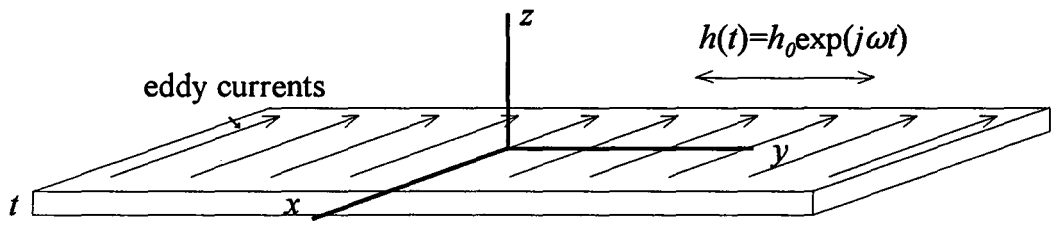

Fig. 2.13. Screening of the time dependent magnetic field h(t) by eddy currents.

For a thin film with infinite dimensions in the x- and y-directions it is possible to calculate the effect these eddy currents have on the permeability. The derivation relies on solving the Maxwell equations, a treatment which is discussed in [16]. Here we only give the result of the permeability:

$$\hat{\mu}_{r,\,eddy}=\frac{\mu_{r,\,i}}{k}\frac{(\sinh k+\sin k)-j(\sinh k-\sin k)}{\cosh k+\cos k}, \tag{2.25}$$

where $\mu_{r,\,i}$ is the intrinsic relative static rotational permeability such as discussed in section 2.3 and $k=t/\delta$ with t the thickness of the film and δ the skin depth which is given by:

$$\delta=\sqrt{\frac{2}{\omega\sigma\mu_i}}=\sqrt{\frac{2\rho}{\omega\mu_i}}. \tag{2.26}$$

Here σ is the conductivity, $\rho=1/\sigma$ the resistivity and $\mu_i=\mu_0\mu_{r,\,i}$ the intrinsic permeability. The skin depth is a measure for penetration or decay of the external applied field as a function of distance from the surface. It is now obvious that for high resistivities the skin depth can still be large at high frequencies. Therefore the field can penetrate deeper into the film, so in this manner a high permeability can still be guaranteed at high frequencies, which is important from a technological point of view. It is also clear from Eq. (2.25) and (2.26) that as a function of frequency μ' drops off more rapidly if the thickness t of the film is larger. At large t only a

relatively small part of the film proportional to δ 'sees' the field and thus can contribute to an induced magnetization or alternatively can contribute to the permeability. Figure 2.14 represents a measurement of the complex permeability as function of frequency together with a calculation based on Eq. (2.25).

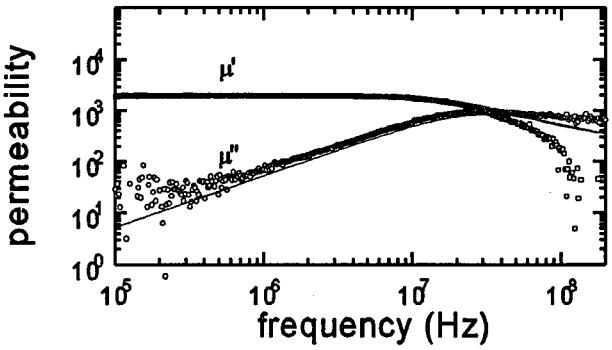

Fig. 2.14 Measurement and calculation of frequency dependent magnetic permeability frequency of a 2 μm thick $Ni_{80}Fe_{20}$ thin film (B_s=1 T, ρ=24 μΩcm).

Both at low frequencies and at high frequencies the permeability becomes a very simple formula. At low frequencies Eq. (2.25) reduces to

$$\hat{\mu}_{r,\,eddy}(\omega\to 0)=\mu_{r,\,i}\left(1-\frac{1}{6}jk^2\right), \tag{2.27}$$

by which the real and imaginary components of the complex permeability will behave as $\mu'=\mu_{r,i}$ and $\mu''\propto\omega$, i.e. as a horizontal line and an ascending line with slope 1 (see Fig. 2.12). At high frequencies

$$\hat{\mu}_{r,\,eddy}(\omega\to\infty)=\frac{\mu_{r,\,i}}{k}(1-j), \tag{2.28}$$

and both components drop of as $1/\sqrt{\omega}$, i.e. a descending line with slope -1/2 on a log-log scale, see Fig. 2.14. The cross frequency at which the real and imaginary part of the permeability are equal can be considered as a typical frequency at which the decrease of the permeability sets in. It can be shown easily using Eq. (2.25) that this frequency is given by

$$f_{cross}=\frac{\pi\rho}{\mu_0\mu_r t^2} \tag{2.29}$$

b) Ferromagnetic resonance

Apart from eddy currents, there is another loss mechanism possible in ferromagnetic materials, which is related to the dynamic response of the spin system itself. Spins always carry out a precessional motion with a certain frequency around their equilibruim position. When the frequency of an applied field approaches this frequency, resonance occurs. This is the so-called ferromagnetic resonance (FMR). Actually it is a quantum mechanical phenomenon, but it is possible to describe it classical if many spins are coupled to a macroscopic magnetization M. The Landau-Lifshitz equation gives a phenomenological description of this phenomenon. The equation is an equation of motion for the magnetization and describes the response of the time dependent magnetization on static and time dependent fields. Consequently, the discription includes the effects of resonances on the magnetic permeability. The equation is given by:

$$\frac{1}{\gamma}\frac{d\vec{M}}{dt}=\mu_0\vec{M}\times\vec{H}_i-\frac{\alpha}{\gamma M_s}\vec{M}\times\frac{d\vec{M}}{dt}, \tag{2.30}$$

Here $\gamma=ge/2m_e$=185 GHz/T is the gyromagnetic ratio for Fe with e the electrical charge, m_e the mass of a free electron, and g the Landé-factor which is 2 for spin motion. H_i is the internal (effective) field, which is the sum of the applied magnetic field and the effective anisotropy field. The first term on the right of the Landau-Lifshitz equation describes the normal precessional motion of a magnetic moment in the internal magnetic field. The second term describes the damping force acting on the precessional motion, α is the damping constant. This force gives rise to a motion perpendicular to the magnetization, moving it towards the equilibrium direction. Consequently, the magnetization will spiral towards its equilibrium direction along $\vec{H}_i$.

Strictly speaking, the Maxwell equations should be solved coupled with the Landau-Lifshitz equation to obtain the magnetic permeability or susceptibility i.e. the proportionality between the dynamic magnetization and the field. To make this easier, the following assumptions are made:

- the time dependent field is uniform across the thickness of the film, i.e. eddy currents are not considered. This assumption decouples the Landau-Lifshitz equation from the Maxwell equations and it is sufficient to solve Eq. (2.30) seperately.
- uniform precession of magnetization, i.e. no spinwave-like modes occur.
- the magnetization M_s is large in comparison with the anisotropy field H_K.
- higher order terms ($\geq$2) in the dynamic components of M and H are neglected.

Using these assumptions, it is possible to obtain an analytic expression for the complex magnetic permeability including ferromagnetic resonance effects. In this report we will distinguish two cases in geometry, which are interesting to examine more in detail.

First, in connection with frequency dependent *permeability measurements*, a small time dependent magnetic field $h(t)=h_0\exp(j\omega t)$ is applied in the y-direction of a thin film (N_z =1), having uniaxial anisotropy K_u with an easy axis in the x-direction.

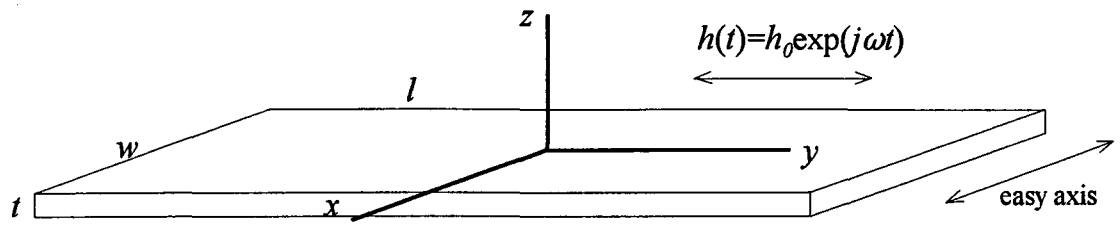

Fig. 2.15 Geometry of time dependent magnetic fields in case of permeabilty measurements. The easy axis is along the x-direction whereas the applied field is along the y-direction..

Solving the complex frequency dependent permeability out of the Landau-Lifshitz equation, yields [16]:

$$\hat{\mu}_{fmr}=1+\frac{\mu_0^2 M_s^2 + \frac{j\omega}{\gamma}\alpha\mu_0 M_s}{[(\frac{\omega_{res}}{\gamma})^2-(\frac{\omega}{\gamma})^2][1+\alpha^2] + \frac{j\omega}{\gamma}\alpha\mu_0 M_s} \tag{2.31}$$

In this equation the resonance frequency ω_{res} is given by:

$$(\frac{\omega_{res}}{\gamma})^2=\frac{2\mu_0 K_u}{1+\alpha^2}, \tag{2.32}$$

with K_u the effective uniaxial anisotropy, represented by the sum of the (field induced) uniaxial anisotropy K_{ind} and the shape anisotropy (and in general also other possible contributions such as magneto-striction):

$$K_u=K_{ind}-\frac{1}{2}\mu_0 M_s^2 N_y. \tag{2.33}$$

At the resonance frequency $\omega=\omega_{res}$ the dedominator in Eq. (2.31) becomes minimal meaning that at this point μ' becomes maximal while μ" becomes 1. Note that taking the limit $\omega\to 0$ gives Eq. (2.11) which describes the static situation.

Another geometry which is of interest to us is related to *electron spin resonance* experiments (ESR). Here, a constant main field is applied in the *y*-direction. In contrast with the permeability measurements, the small time dependent component of the magnetic field is of fixed frequency in the GHz range and is applied in the direction parallel to the *x*-axis (see Fig. 2.16).

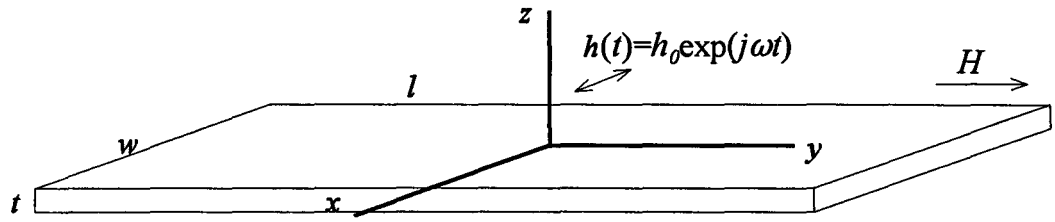

Fig. 2.16 Geometry of time dependent magnetic fields in case of ESR experiments.

Again, solving the Landau- Lifshitz equation, yields for the permeability:

$$\hat{\mu}_{fmr}=1+\frac{\mu_0 M_s(\mu_0 M_S+\mu_0 H) + \frac{j\omega}{\gamma}\alpha\mu_0 M_s}{[(\frac{\omega_{res}}{\gamma})^2-(\frac{\omega}{\gamma})^2][1+\alpha^2] + \frac{j\omega}{\gamma}\alpha(\mu_0 M_s+2\mu_0 H)} \tag{2.34}$$

In this equation the resonance frequency ω_{res} is given by:

$$(\frac{\omega_{res}}{\gamma})^2=\frac{\mu_0 H(\mu_0 M_s+\mu_0 H)}{1+\alpha^2}. \tag{2.35}$$

The reason that the uniaxial anisotropy K_{ind} does not appear in Eq.(2.34) and (2.35) is because of the assumption $H_K=2K_{ind}/\mu_0 M_s<<H$.

Another difference between the permeability measurements and the ESR experiments is that in the first case the frequency is a variable parameter, while in the latter case the frequency is a constant determined by the klystron and the magnetic field H is the scanning parameter. Resonance occurs at a certain field H obeying Eq.(2.35).

By substituting the permeability due to ferromagnetic resonance (Eq. (2.31)) for the intrinsic permeability μ_i in the eddy current formula (Eq. (2.25)) one obtains a permeability accounting for both mechanisms. Strictly speaking this is not the correct way, because the Maxwell equations and the Landau-Lifshitz equation are not uncoupled, as mentioned before. In Figure 2.17 a summary of three situations is given for a FeHfO film with the roll-off of the permeability caused by: (a) only eddy currents, (b) only FMR, (c) both FMR and eddy currents. The parameters used for the calculations are indicated in this figure. Figure 2.18 represents the same calculated curves but now plotted on a logaritmic scale.

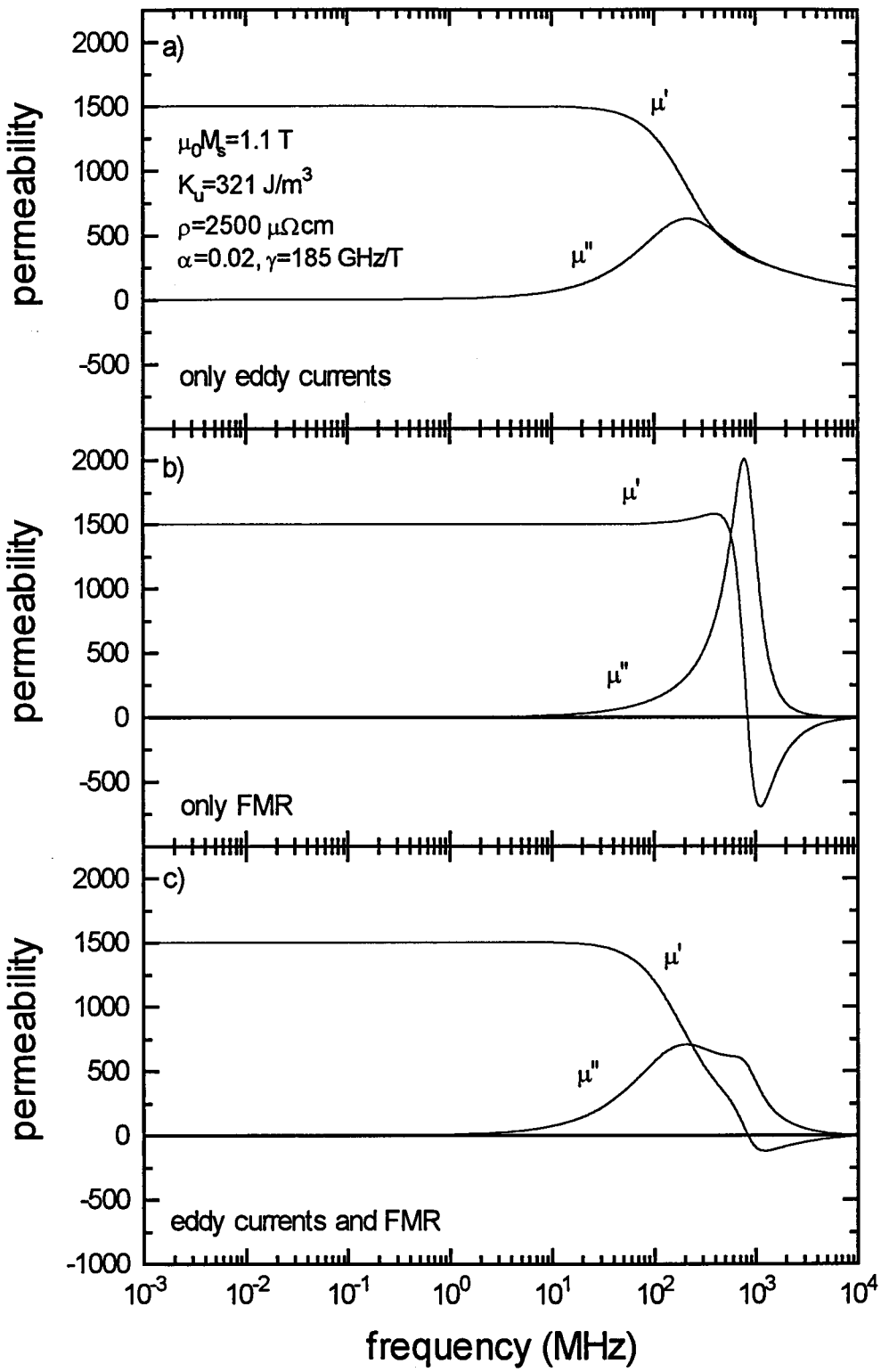

Fig. 2.17 Permeability of a FeHfO thin film caused by (a) only eddy currents, (b) only FMR, (c) both FMR and eddy currents. The parameters used for the calculations are indicated.

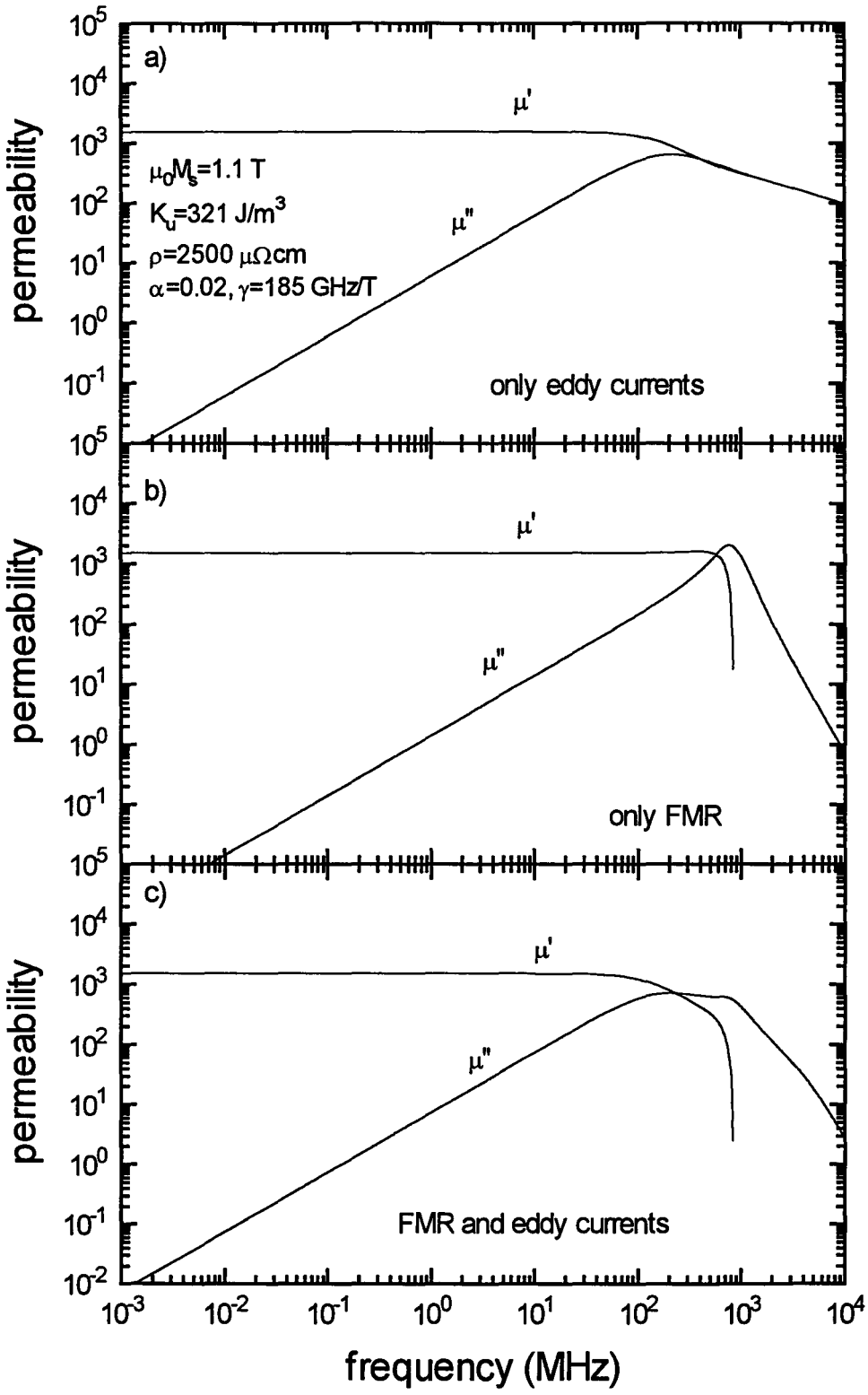

Fig. 2.18 Permeability of a FeHfO thin film caused by (a) only eddy currents, (b) only FMR, (c) both FMR and eddy currents. The parameters used for the calculations are indicated. This figure is the same as Fig. 2.18, but the permeability is plotted on a logarithmic scale.

c) Frequency dependent wall permeability

The two preceding sections are related to the loss mechanisms in case of rotational magnetization. This section describes the frequency dependence of the wall movements: the domain wall is not able to follow a time dependent magnetic field $h(t)$ at high frequencies. Again eddy current losses and FMR losses occur.

At the position where the wall moves as a function of time, the magnetization changes. Consequently, the magnetic induction changes with time, which again leads to local eddy currents which oppose the magnetic field and thus suppress the wall movements. The same damping mechanism that opposes the precession of magnetization (FMR) also suppresses the rotation of the spins in a moving domain wall. In the same geometry as depicted in Fig. 2.10, except for the choice that the field is now parallel to the easy axis (ϕ_H=0), the equation of motion for a 180° domain wall is [15]

$$m_w \frac{d^2 s(t)}{dt^2} + \beta_w \frac{ds(t)}{dt} + \alpha_w s(t) = 2\mu_0 M_s h(t), \tag{2.36}$$

where m_w is a measure for inertia of the wall per unit area, β_w the damping coefficient, α_w the restoring coefficient which is the same as in Eq. (2.16). The position of the wall is $s(t)$, while the term on the right hand side represents the driving force being related to the gain in field energy in the time dependent field. Additionally, we have chosen s_0=0 for convenience. After solving this differential equation assuming harmonic time dependencies we obtain the frequency dependent permeability

$$\hat{\mu}_{r,\,wall}(\omega) = 1 + \frac{4\mu_0 M_s^2}{D_w} \frac{(\alpha_w - m_w\omega^2) - j\omega\beta_w}{(\alpha_w - m_w\omega^2)^2 + (\omega\beta_w)^2}. \tag{2.37}$$

Here D_w is again the width of a domain in the hard axis direction (see again Fig. 2.10). In the limit for low frequencies $\omega \to 0$ we again obtain Eq. (2.21) with ϕ_H=0°. The behaviour of the permeability as function of the frequency depends on the damping β_w. For small damping ($\beta_w \to 0$) the function shows resonance at a frequency $\omega_{res}=\sqrt{(\alpha_w/m_w)}$, while for large β_w the permeability represents a relaxation behaviour. In the latter case where the permeability is decreased by a factor 2 at the frequency $\omega=\alpha_w/\beta_w$. Fig. 2.19 shows this situation.

We note that the loss mechanisms (eddy currents and FMR) are hidden in the parameters m_w and and β_w. Expressions for these parameters have been derived in literature [17].

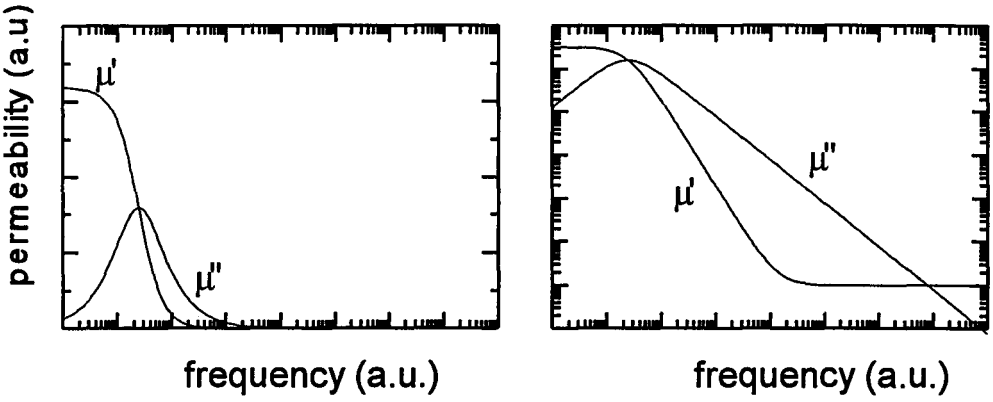

Fig. 2.19 Frequency dependent permeability due to domain wall movements in case of large damping.

2.5 Basic principles of soft magnetic materials

This section discusses the principle that underlies the soft-magnetic behaviour of nano-crystalline materials. Because this principle exclusively applies to nano-crystalline materials we start this section by putting things into perspective and briefly mention other classes of materials where the soft-magnetic properties are based on a different principle. As may be clear from the previous sections, particularly Eq. (2.11), soft magnetism i.e. a high magnetic permeability is obtained only in case of a low magnetic anisotropy. Now, soft magnetic materials can be divided into three main groups:

1. *Crystalline materials*. Few crystalline materials happen to combine a low magneto-crystalline anisotropy with a low magnetostriction, in order to obtain a high permeability. The most well known examples of these materials that are used nowadays are Mn-Zn ferrite and $Ni_{80}Fe_{20}$ (permalloy).

2. *Amorphous materials*, which also combine a low anisotropy with a low magnetostriction. Here, magneto-crystalline anisotropy is absent because of the absence of crystal symmetry. Examples of these materials are CoFeSiB and CoNbZr. By adjusting the [Co]/[Fe] ratios and the [Nb]/[Zr] ratios, respectively, the magnetic properties can be varied. For example, the magnetostriction constant can be manipulated and tuned to zero.

3. *Nanocrystalline materials*, which are inhomogeneous materials consisting mostly of two phases: a ferromagnetic and a non-magnetic phase. Although the magneto-crystalline anisotropy of the ferromagnetic nano-crystals themselves is large, the *effective* averaged anisotropy can be rather small as will be discussed below. FeHfO, subject of the present report, but also FeTaN, form examples of these materials.

The remainder of this section is to discuss the physical mechanism underlying the above mentioned averaging of the magnetic anisotropy in nano-crystalline materials. The basic ingredient of the mechanism that determines the soft-magnetic properties appears the interplay between the local magnetic anosotropy and the ferromagnetic exchange energy. The important length scale that determines how and to what degree the interplay determines the magnetic properties is set by the ferromagnetic exchange length L_{ex} given by:

$$L_{ex}=\sqrt{\frac{A}{K}}, \tag{2.38}$$

where A denotes the exchange stiffness which is proportional to J in Eq. (2.1) and K the constant of anisotropy. The typical domain wall width δ, for instance, satisfies $\delta=\pi L_{ex}$. For nano-crystalline materials the average size of the grains D compared to L_{ex} turns out to be the critical parameter that determines the magnetic properties.

In case of *large grains* satisfying $D > L_{ex}$, the magnetization will be determined by the crystalline anisotropy K_1. To clarify this, a schematic representation of the microstructure of nano-crystalline materials like FeTaN is shown in Fig. 2.20

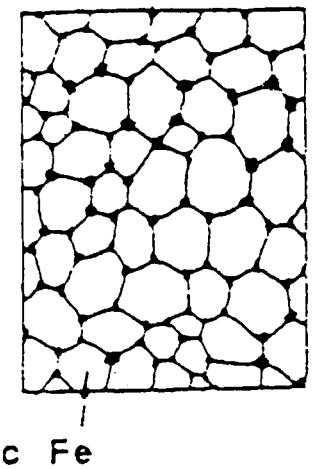

Fig.2.20 Microstructure of FeTaN.

These nano-crystalline material consist of nanometer-sized polycrystallites with at the triple points a non-magnetic phase, TaN in the case of FeTaN. The orientations of the easy axes are random. In order to minimize the magnetic anisotropy energy the magnetization direction would like to follow these random directions. The exchange interactions between the spins oppose these changes in direction. However, for large crystallites the change in direction can take place gradually causing the exchange energy in the thus formed domain walls to be limited i.e. the wall contribution is smaller than the gain in magnetocrystalline anisotropy energy that is obtained by letting the magnetizations follow the preferential directions. Since the anisotropy of each crystallite is large it is clear that in such a situation this means that in the magnetization process this large anisotropy must be overcome, leading to a low permeability (Eq. (2.12)) in the case of large grains.

For very small grains satisfying $D << L_{ex}$ the magnetization will not follow the local preferential directions. This is because in that case the magnetization should change direction within short distances which is energetically unfavourable: it costs too much exchange energy, see Eq. (2.1), where ψ is now the angle between the preferential directions of two crystallites. Thus the magnetization direction will be uniform across a number of random orientated preferential directions and consequently the crystalline anisotropy will be averaged out to some degree leading to a high permeability in the case of small grains.

In the general cas, the magnitude of the averaged anisotropy $<K>$ is determined by statistics and is shown [18] to be given by

$$<K> \approx \frac{K_1}{\sqrt{N}} = K_1 \left(\frac{D}{L_{ex}}\right)^{3/2}, \tag{2.39}$$

where $N=(L_{ex}/D)^3$ is the number of grains across which the magnetization has a uniform direction. The exchange length now becomes $L_{ex}=\sqrt{(A/<K>)}$. Substituting this into Eq. (2.39) yields that the effective anisotropy is given by

$$<K> \approx \frac{K_1^4}{A^3} D^6. \tag{2.40}$$

From this equation it is clear that the effective anisotropy is strongly dependent on the grain size: low anisotropies and hence high permeabilities are obtained for very small crystallites. This is the reason why these materials are called nano-crystalline materials.

What is also clear from Eq. (2.40) is that preferably as a base a ferromagnetic material wih an as low as possible magnetocrystalline anisotropy is used. This is the reason that one prefers Fe based nano-crystalline materials above Co-based nano-crystalline materials. Ni-based nano-crystalline materials can be made also soft. However, here the disadvantage from technological point of view is that the saturation magnetization would be rather low. In fact the advantage of the nano-Fe materials over that of the materials in group 1 and 2 is the considerably higher saturation induction. The combined soft-magnetic properties and high saturation magnetisation is the main reason for the fact that these materials attract the attention to application engineers. FeTaN and FeNbSiN and more in general Fe-TM-N are examples, with TM a transition metal. The present report focusses on FeHfO. Here, the advantage is not the high saturation magnetization but the very high resistivity. The somewhat lower saturation magnetization is a result of the higher (summed) hafnium and oxygen content. The higher resistivity is also related to the latter. However, if one would replace oxygen by nitrogen and thus compares FeHfO and FeHfN materials with the same amount of non-magnetic elements it appears that the resisitivity of the oxide based material is considerably higher [19]. As mentioned earlier the high resistivities are desirable: they extend the frequency range in which the soft-magnetic material has a high magnetic permeability. It appears that FeHfO like materials have a different microstructure compared to the earlier mentioned FeTaN like materials: it is composed of bcc-Fe nanograins in an amorphous phase, see Fig. 2.21.

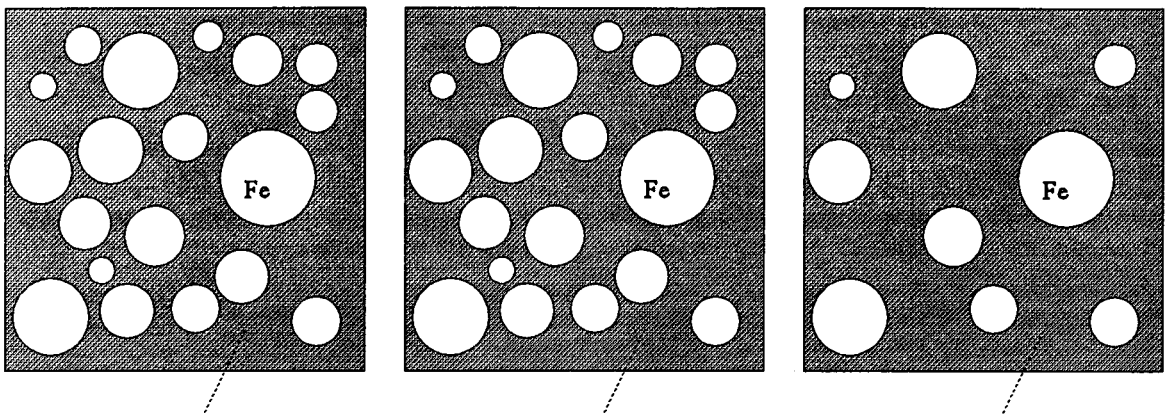

Fig. 2.21 Schematic representation of the microstructure of nanocrystalline FeHfO (a) in case of large μ behaviour and (b) in case of GMR behaviour.

From the discussion earlier it is clear that to yield a high permeability or equivalently an anisotropy that is averaged out, the crystallites should be small and that the amorphous phase should be ferromagnetic (Fig. 2.21(a)) with a sufficiently large exchange constant A to couple the crystallites. This is to prevent that domain walls are formed within. Furthermore, the distance between the crystallites must be comparable to the sizes of the crystallites. Obviously, such microstructural details are expected to depend on the preperation conditions. In chapter 4 the relation between the soft-magnetic properties and the preperation conditions is investigated.

It will become clear from the next section, that in order to exhibit a significant magnetoresistance effect the material has to fulfill a principle requirement viz. the angles between the magnetization directions in the neighbouring Fe-crystallites should be changeable by applying a magnetic field. This automatically implies that the crystallites are weakly coupled or not coupled at all. In turn this has the consequence that a large magnetoresistance effect and a high magnetic permeability in these materials mutually exclude each other: for a large permeability a large exchange constant is required (see Eq. (2.40)) whereas for a high magnetoresistance a preferably zero exchange constant is requird (A=0). Clearly, films with high permeability will differ from films with a high magnetoresistance as regards their microstructure. This difference is schematised for clarity in Fig. 2.21(b). For a large magnetoresistance FeHfO, i.e. a so-called GMR FeHfO, the effective decoupling of the Fe-crystallites can be caused by either the fact that the amorphous FeHfO phase seperating the crystallites is non-magnetic (A=0, see Fig. 2.21 (c)) or alternatively in the case that it is ferromagnetic the distance between the Fe-crystallites should be considerably larger than the exchange length. In the latter case domain walls form between the several crystallites.

2.6 Magnetoresistance (MR) in granular alloys

2.6.1 Introduction

The resistance changes when a magnetic field is applied. Mostly the so-called anisotropic magnetoresistance (AMR) occurs. This is the dependence of the resistance on the direction of the magnetization (or applied magnetic field) with respect to the direction of the current. Like magnetic anisotropy the phenomenon originates originates from spin-orbit coupling by application of a magnetic field, the magnetization rotates towrds athe magnetic field and because of the spin-orbit coupling the atomic electron orbits will also rotate to some degree. It might be clear that due to the latter, the orientation of the orbit with respect to the current also changes and that hence the cross section or scattering probability of the conduction electrons with atomic orbitals changes. The result is the above mentioned angular dependent resistance. This magnetoresistance effect is typically 2% and occurs in homogeneously as well as in inhomogeneously magnetized ferromagnetic magnets. This is not true for the so-called GMR effect. For few effects to occur it is necessary that the magnetization direction within the material changes. Magnetic multilayers consisting of a stack of alternating ferromagnetic and non-magnetic layers such as Co/Cu/Co/... form an example. Here, the magnetization direction may change from layer to layer. For these systems the GMR effect was first observed. Another example is formed by granular materials where the magnetization may also be non-uniform, i.e. it may vary from crystallite to crystallite. Clearly, the latter case is of interest for the present report, i.e. for the FeHfO films that have not been studied. We define the MR-ratio as follows:

$$MR = 100\% \cdot \frac{R(0) - R(H_{sat})}{R(H_{sat})}. \tag{2.41}$$

Here, $R(H)$ is the resistance in the presence of an external field H and H_{sat} is the field at which the system magnetically saturates. The MR-ratio is therefore the relative difference in resistivity between the situation that all magnetic moments are alligned parallel to the field (see Fig. 2.22(b)) and the situation at zero field where the magnetization in the crystallites make certain non-zero angles with each other (see Fig. 2.22(a)). The reason that these situations have different resistivity will become clear from the next section.

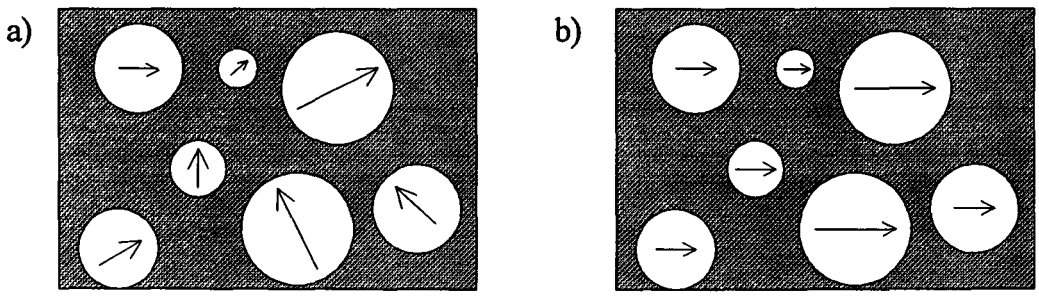

Fig. 2.22. Magnetizations of ferromagnetic clusters in a non-magnetic matrix in (a) zero-field and (b) in case of saturation.

2.6.2 Origin of GMR

Nowadays, it is accepted that the GMR arises from a different scattering probability for different spin directions of the conduction electrons with respect to the direction of the local magnetization resulting in two different resistivities for spin-up (s_z=1/2) and spin-down (s_z=-1/2) electrons, viz. $\rho\uparrow$ and $\rho\downarrow$ repectively. If we accept for a magnetic moment that $\rho\uparrow$ is indeed not equal to $\rho\downarrow$, we will come back later to this point, then it is relatively straightforward to reason that this will be a difference in resistivity between the satuarated sistuation and a saturated situation.

For the situation that the magnetization in the ferromagnetic crystallites are aligned parallel, the current can be subdivided in two independent currents according to the two current model [20]: a spin-up and a spin-down current of electrons, see Fig. 2.23 (a). The resistance will be

$$R_P=\frac{\rho\uparrow\rho\downarrow}{\rho\uparrow+\rho\downarrow}. \tag{2.42}$$

In case of antiparallel magnetizations, every electron spin will have its spin direction alternatively parallel and antiparallel to the magnetization when it traverses the several crystallites, which may occur in a multilayer system but will in general not occur in a granular system. In the case that the number of crystallited that heve their magnetization pointing upwards is equal to the number of crystallites with the magnetization pointing downwards, the situation is described by Fig. 2.23(b) and the resistivity is consequently given by:

$$R_{AP}=\frac{1}{4}(\rho\uparrow+\rho\downarrow). \tag{2.43}$$

Comparing R_P and R_{AP} it is clear that the resistivity in the antiparallel (AP) situationis different and larger than the resistance in the parallel situation (P). An alternative way of presenting the ferromagnetic and antiferromagnetic state is presented in Fig. 2.23(c) and (d). The reason why this has been done becomes clear in section 2.6.4 where we will discuss the spin-flip scattering.

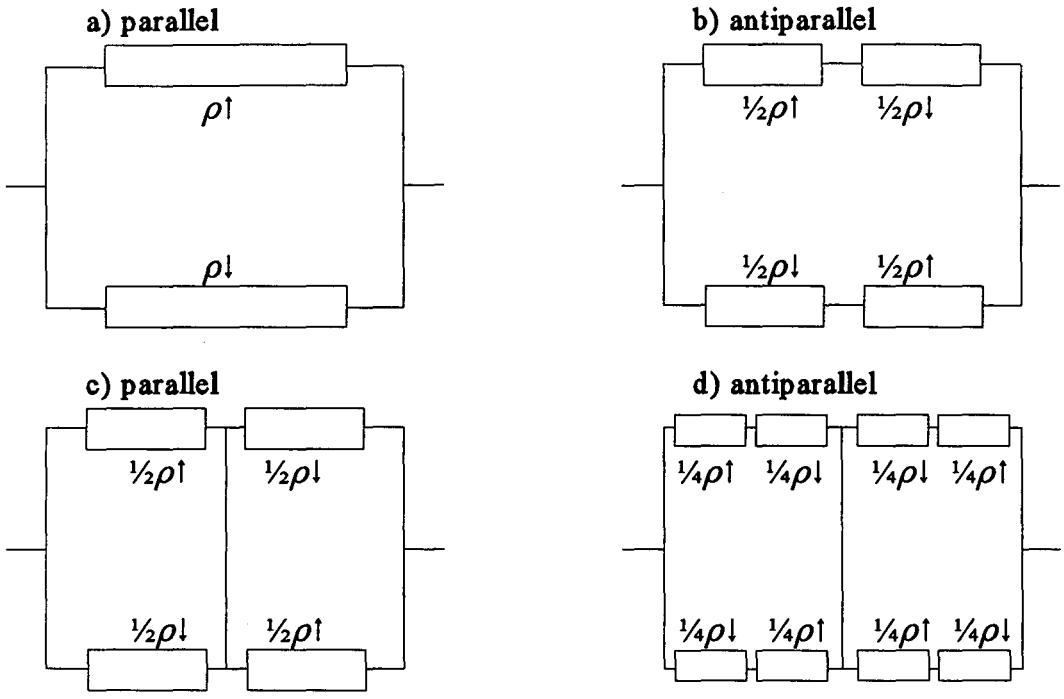

Fig. 2.23 Resistance in case of (a) parallel magnetization and (b) antiparallel magnetization. In (c) and (d) the parallel and antiparallel state are presented in an alternative way. In the latter case the spin-up and spin-down electrons switch channel.

To conclude this section we briefly discuss why $\rho\uparrow \neq \rho\downarrow$, i.e. the origin of spin dependent scattering becomes clear when we consider the density of states of the 3*d* bands of the ferromagnets Fe, Co and Ni. For these, the *d*-band is splitted for spin-up and spin-down electrons and are shifted relative to each other, resulting in a different density of states D at the Fermi energy E_F, viz. $D\uparrow$ and $D\downarrow$ respectively. Clearly, this shift is the origin of ferromagnetism of Fe, Co and Ni. Now the transport occurs by conduction electrons: the *s*- and *p*-electrons. The corresponding energy bands have no assymetry with respect to the spin direction. However, the reason for $\rho\uparrow$ being not equal to $\rho\downarrow$, is due to the fact that the scattering probabilities of the *d*-scattering processes is proportional to the final density of states.

2.6.3 Tunnelling magnetoresistance (TMR) in granular magnetic films

In granular alloys where ferromagnetic metalic clusters are dissolved in a insulating matrix, it is possible that electrons can tunnel through the insulating barrier. The magnetoresistance in this case is often called tunneling magnetoresistance (TMR). It has been recently observed in highly resistive CoAlO granular magnetic films The resistivity shows a non-Ohmic character and a non-metalic temperature dependence. This has been explained by Sheng *et al.* [21] in terms of electron tunneling between the grains and shows an exponential behaviour with temperature, viz.

$$\rho=\rho_0\exp(C/\sqrt{T}). \tag{2.44}$$

This is the resistivity in zero field in the case of non-magnetic clusters. Inoue *et al.* [22] showed that the conductance $\sigma=1/\rho$ for ferromagnetic metalic clusters is dependent on the relative magnetization m, by

$$\sigma=\sigma_0(1+P^2m^2)\exp(-C/\sqrt{T}), \tag{2.45}$$

where m is the magnetization normalised to the saturation magnetisation: m=0 corresponds to a random distribution of the magnetization directions and m=1 corresponds to the saturated situation. P is the polarization which represents the asymmetry in the density of states for different spin directions and is defined as

$$P=\frac{D\uparrow-D\downarrow}{D\uparrow+D\downarrow}. \tag{2.46}$$

Here, $D\uparrow$ is the density of states at the Fermi level for spin-up electrons whereas $D\downarrow$ is the density of states at the Femi-level for spin-down electrons. MR(m), which is the magneto-resistance as a function of the relative magnetization m is defined as (compare Eq. (2.41)):

$$MR(m)=100\%\cdot\frac{\rho(m)-\rho(m=1)}{\rho(m=1)}. \tag{2.47}$$

MR(m) behaves as $P^2(1-m^2)/(1+P^2m^2) \approx P^2(1-m^2)$ for small values of P. The maximal MR ratio is now P^2. This means that in case of Fe the maximum MR ratio is achieved at 16%, because P=40% for Fe (table I). From this model it also follows that if no other mechanisms take place than tunneling, the MR ratio should be temperature independent.

Table I Polarization and maximum (theoretical) MR ratio of three magnetic d-metals [22].

metal	*polarization P (%)*	*maximum MR ratio (%)*
iron (Fe)	40	16
Cobalt (Co)	34	12
Nickel (Ni)	23	5.3

2.6.4 Temperature dependence of MR

As mentioned just before the MR ratio will not be temperature dependent when the resistivity and thus the conductance is just determined fully by the tunnel resistance. However, in practice spin-flip scattering processes are expected to occur. Since these processes depend on temperature and have the tendency to mix the currents of the two spin directions, the MR ratio may decrease with the temperature. Fert *et al.* [20] proposed this mechanism for temperature dependent resistance in ferromagnetic materials diluted with transition metal ions and applied the resistor scheme illustrated in Fig. 2.24 to describe this.

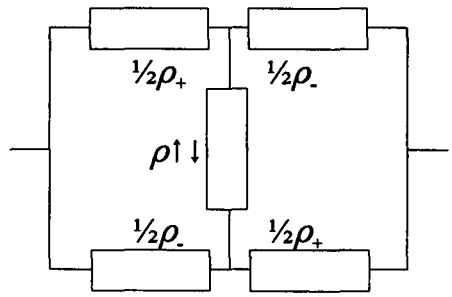

Fig. 2.24 Equivalence circuit of granular alloy including spin-mixing (ρ↑↓).

The resistance of such a circuit is given by (see also Fert [20]):

$$\rho=\frac{\rho_+\rho_-+\rho\uparrow\downarrow(\rho_++\rho_-)}{\rho_++\rho_-+4\rho\uparrow\downarrow}, \tag{2.48}$$

where ρ_+ and ρ_- denote the resistivities of the majority and minority electrons respectively, andwhere $\rho\uparrow\downarrow$ is the spin-mix resistivity, describing spin-flip scattering processes which tend to equalize the to spin currents. This means that for $\rho\uparrow\downarrow \to \infty$ the spin-up and spin-down channel is entirely equalised, yielding MR=0, whereas for $\rho\uparrow\downarrow \to 0$ the situation without spin flips is again obtained. The resistivities ρ_+ and ρ_- consist of the sum of the part of the grains with magnetizations 'up' and the part with magnetizations 'down':

$$\begin{aligned}\rho_+&=\frac{1}{2}\frac{N}{M}\rho\uparrow+\frac{1}{2}(1-\frac{N}{M})\rho\downarrow,\\ \rho_-&=\frac{1}{2}\frac{N}{M}\rho\downarrow+\frac{1}{2}(1-\frac{N}{M})\rho\uparrow.\end{aligned} \tag{2.49}$$

Here, M is the total number of grains and N is the number of grains with magnetization 'up', leading to a resistivity $\rho\uparrow$ and M-N the number of grains with magnetization down, leading to a resistivity $\rho\downarrow$. By applying a field the granular alloy is saturated if N=M and if no field is applied N=M/2.

From this circuit model the resistivity ρ can be calculated as a function of the relative magnetization m. This is done by substituting Eq. (2.49) into Eq. (2.48) and using $m=(2N-M)/M$.

$$\rho=\frac{1}{4}(\rho\uparrow+\rho\downarrow)-\frac{1}{4}m^2\frac{(\rho\uparrow-\rho\downarrow)^2}{\rho\uparrow+\rho\downarrow+4\rho\uparrow\downarrow}. \tag{2.50}$$

This can be regarded as the general formula for the resistivity in a field. If no spin-mixing ($\rho\uparrow\downarrow=0$) is present Eq. (2.50) returns to the usual two current model: for $m=1$ the parallel situation of Eq. (2.42) is described For $m=0$ the antiparallel (or random) situation, see Eq. (2.43). The temperature dependence can now be obtained by comparison of Eq. (2.50) and Eq. (2.45). This enables one to express $\rho\uparrow+\rho\downarrow$ and $\rho\uparrow-\rho\downarrow$ in terms of ρ_0, $\exp(C/\sqrt{T})$ and P. The result is:

$$\rho=\rho_0\exp(\frac{C}{\sqrt{T}})-m^2P^2\frac{\rho_0^2\exp(2\frac{C}{\sqrt{T}})}{\rho_0\exp(\frac{C}{\sqrt{T}})+\rho\uparrow\downarrow} \tag{2.51}$$

Clearly, $\rho\uparrow\downarrow$ becomes sufficiently large (at high temperatures) and total mixing of spins takes place and the resistivity is no longer dependent on m. The spin-mixing rate at finite temperature has been modeled by Fert *et al.* [20] showing that, without going into details, $\rho\uparrow\downarrow$ must be proportional with T^2. Because the spin-flip resistivity can be described with a T^2-law and not with an exponentional law as in Eq. (2.45), it follows that the GMR ratio becomes temperature dependent.

This model description will be used in the interpretation of the magnetoresistance data in chapter 5. We would like to emphasize the simplicity of this model, since some rather crude assumptions have been made, such as the averaging over the crystallites in series with just 'up' and 'down' magnetizations. However, the effect of spin-mixing in the tunneling magneto-resistance effect have not been treated in literature so far. Our model can be regarded as a first attempt.

3 High frequency μ measurements

3.1 Introduction

Up till now, frequency dependent magnetic permeability measurements were performed with a set-up operating in the low frequency range: from 10 kHz up to 13 MHz. In future applications high permeabilities also for high frequencies are required. Moreover, to study loss mechanisms in the dynamic behaviour of magnetic films, it is desirable to investigate the behaviour in an as wide as possible frequency range. Therefore efforts have been made to extend the frequency range up to 200 MHz. This chapter describes how this is done and discusses the complications connected with the extension of the frequency range. The build up of this chapter is as follows: Section 3.2 addresses the principle of the frequency dependent permeability measurements. From this it becomes clear that the measurement of the inductance of a coil plays a central role. Therefore some attention to this is given in section 3.3. Section 3.4 describes the measurement procedure: in high frequency permeability measurements, the measuring coil will resonate at a certain frequency, related to the stray capacity of the coil and the sample inside. How to correct for this complication will be discussed also. Section 3.5 gives a summary of the advantages and disadvantages of the high frequency set-up above the low frequency set-up. Finally, section 3.6 will draw conclusions and give recommendations.

3.2 Principle of the measurement

To measure the magnetic permeability μ as function of the frequency, use is made of a coil, in which a sample is placed (Fig 3.1).

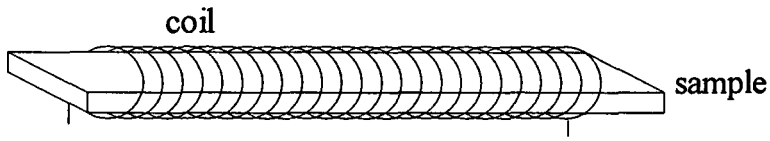

Fig. 3.1 Principle of a frequency dependent magnetic permeability measurement.

The determination of μ involves measurement of the electrical impedance Z of a coil. This impedance is determined by the resistance R and inductance L of the coil $Z=R+j\omega L$. In turn the inductance depends on the magnetic permeability of the magnetic sample. If the sample fills the coil completely, the (complex) self inductance L, which is defined as the flux through the coil divided by the current, is given by:

$$L=\mu_0\hat{\mu}_r \frac{N^2A}{l_c}. \qquad (3.1)$$

Here, N is the number of windings and l_c is the length of the coil, while A is the cross sectional area and $\hat{\mu}_r=\mu'-j\mu''$ is the *complex* relative magnetic permeability of the sample. So, in principle a (frequency dependent) measurement of the impedance and thus the inductance L enables one to determine the magnetic permeability.

In practice, the sample (a thin film) will not fill the coil completely, but the total magnetic flux in the coil will be generated partly by the sample and partly by the surrounding air in the coil. So if one is interested in the permeability of the sample, one should correct for the flux through the air. This is done by subtracting the inductance L_0 of an empty coil from the inductance L of a coil with a sample inside. Experimentally, this means that two measurements should be performed: a so-called *sample* measurement and a so-called *empty* measurement. It is a straightforward matter to derive an expression for the difference between those two inductances. The difference is given by:

$$L-L_0=\mu_0\frac{(N\frac{l}{l_c})^2}{l}A(\hat{\mu}_r-1). \tag{3.2}$$

Here, A is the cross sectional area of the sample width times thickness. When considering this expression one notes that $L-L_0$ can be considered as the inductance of a fully filled coil with the coil length equal to the sample of length l, thus with an *effective* number of windings equal to Nl/l_c, see Fig. 3.1. If the coil and sample dimensions are known and the inductances have been obtained from measurements, the magnetic permeability can be calculated.

It should be noticed that the magnetic permeability extracted from the above considerations, must be corrected. There are a two sources of error which can influence the permeability, besides the demagnetizing field already discussed in chapter 2:

1. The applied field is overestimated, the field is not homogeneous: at the end of the coil, the field becomes weaker.
2. The magnetic flux is only detected partly, because some flux lines close inside the coil.

Both errors have an effect on the inductance because they alter the amount of flux enclosed by the coil. Both errors are estimated and discussed extensively in [23]. For now, its sufficient to mention that the first error can be corrected with a factor C_H which corrects for the overestimating of the applied field at the ends of the coil, and the second error with a factor C_f which corrects for the missing flux. Both factors are smaller or equal to 1 and the magnetic permeability μ_{eff} of the sample will be

$$\mu_{eff}=\frac{\mu_{meas}}{C_H C_f}. \tag{3.3}$$

As mentioned μ_{eff} may subsequently be corrected for the demagnetizing field as mentioned in chapter 2 to obtain the intrinsic (material determined) magnetic permeability $\mu_{r,i}$ by applying Eq. (2.14).

3.3 Reflections on the inductance

From the foregoing it is clear that determination of μ completely depends on a reliable measurement of the inductance L and on the validity of Eq. (3.1). This section focusses on this matter. The electrical circuit of the measuring coil is presented in Fig. 3.2.

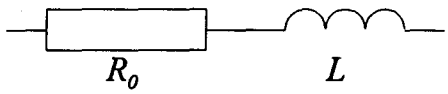

Fig. 3.2 Equivalence circuit of the measuring coil.

The frequency dependent impedance $Z(\omega)$ of this equivalence circuit is given by the expression:

$$Z(\omega)=R_0+j\omega L(\omega), \tag{3.4}$$

where R_0 is the DC resistance of the coil. We designed a coil holder usable for measurements of permeabilities at strips of 34 × 5 mm^2. This holder is shown schematically in Fig 3.3.

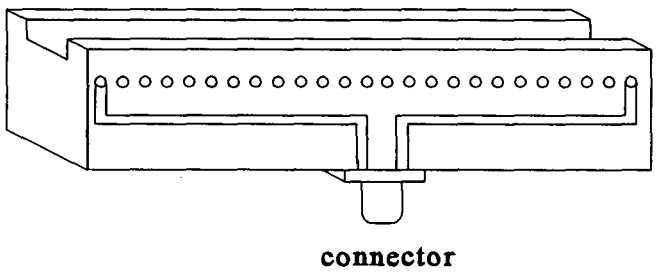

Fig. 3.3 Coil holder for permeability measurements at magnetic strips of 34 × 5 mm^2.

The coil holders contain 25 small holes and is able to carry 24 or 12 windings. Five coils were prepared to investigate. By means of a HP-4195A spectrum analyser which is connected to a HP-41951-60001 impedance test adaptor, the frequency dependent impedance was measured. In Fig 3.4 the imaginary parts of the impedances of the empty coils are given. The frequency range is 10-1000 kHz, where the effect of the stray capacity (see section 3.4) is insignificant.

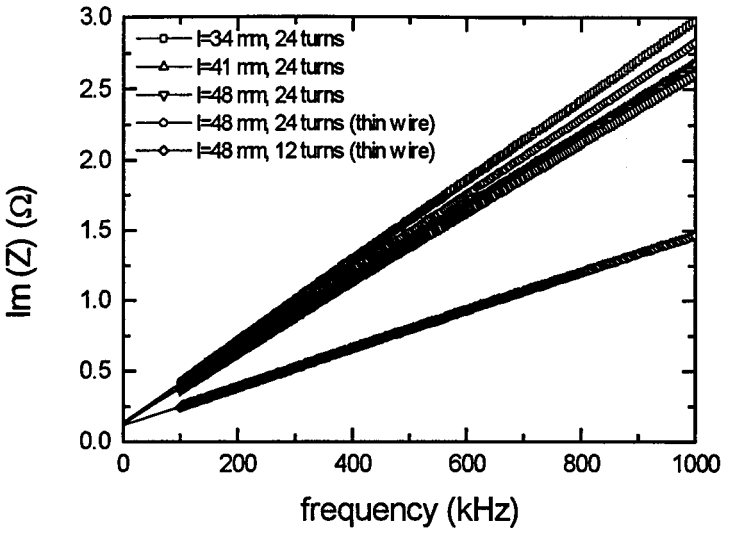

Fig. 3.4 The imaginary part of the impedance is shown together with a fit: linear regression which is based on the equivalence circuit description of the coil, $Z(\omega)=R_0+j\omega L_0$.

It appears that the measured impedance can be described very well by $Z(\omega)=R_0+j\omega L_0$. From the slope of the figure, the inductance L_0 (of the coil without sample) can be obtained. The results of these inductances are summarized in table II. In this table also the calculated values based on Eq. (3.1) are given.

Table II: The dimensions of several coils and the measured and calculated inductances for the case that no sample is inside. The last column represents the magnetic permeability of a FeHfO layer as determined from experiments employing the several coils.

Coil nr.	*Coil length (mm)*	*number of turns*	*wire diameter (mm)*	*experimental inductance L (nH)*	*calculated inductance L (nH)*	*μ' (100 kHz)*
1	34	24	0.5	454	373 ± 53	1250
2	41	24	0.5	408	309 ± 44	1230
3	48	24	0.5	396	264 ± 38	1210
4	48	24	0.3	432	264 ± 38	1250
5	48	12	0.3	216	66 ± 11	1250

The first three coils are all the same with exception of their coil lengths. The cross sectional area is 17.5±2.5 mm^2 and they all contain 24 windings, only the spacing between the turns is varied. Considering these coils, it is noted that the inductance of the coils is larger than expected from the simple formula of Eq. (3.1). They seem to detect more magnetic flux than is calculated ($L=\Phi/I$). The reason why the measured inductances differ so much from the calculated ones, is not very clear. One could suggest that the turns of the coil are not sufficiently close to each other, so that not all magnetic flux is detected by the coil. However, this would lead to a experimental inductance that is *lower* than the calculated values which is not in agreement with the observation.

The last two coils in the table possess a thinner wire (0.3 mm) than the first three coils (0.5 mm). Coil 4 has the same dimensions as coil 3 with exception of the wire diameter. It is again remarkable that the measured inductance is even larger than derived from calculations. Finally, coil 5 is comparable with coil 4 except for the number of turns, which is halved. From Eq. (3.1) it follows that the inductance should diminish with a factor 4. However, the measured inductance only decreases by 45%. The discrepancy between the calculated and the measured inductance L_0 of the latter coil is very large. These results may be explained by assuming that some supply wires also contain an inductance L which adds to the self-inductance of the coil and so enlarges the total inductance as measured with the HP-4195A spectrum analyser.

If we use the coils to determine the magnetic permeabiltity of a typical FeHfO film by employing Eq. (3.2) the data in the last column of the table are obtained. It follows that no significant differences in the permeability occur. This strongly suggests that the discrepancy between experiment and calculation in the inductances for different coils must be a certain constant (sample independent) offset, which is eliminated by subtraction, see Eq. (3.2). In further chapters of these reports where use is made of the HF set-up that this is indeed the case. The there presented permeability results are all obtained with coil 2 with a coil length of 41 mm, unless stated otherwise.

3.4 Measurement procedure

To obtain the permeability in the high frequency (HF) range from the inductance, a HP-4195A spectrum analyser, which can be used to measure impedances up to 500 MHz, is connected to an HP-41951-60001 impedance test adaptor. The spectrum analyser is connected to a PC and can be controlled via a LABVIEW program. The corresponding LABVIEW program will not be presented in this report. After initialisation and calibration, the coil is connected to the test adaptor.

In general the inductance is a complex quantity. It is obvious from Eq. (3.4) combined with Eq. (3.2) that the losses in the permeability, μ" will appear as a frequency dependent electrical resistance. The real part of the permeability μ' finds its expression in the imaginary part of the impedance. The spectrum analyser measures the frequency dependent impedance $Z(\omega)$ of a coil with a sample inside and the impedance $Z_0(\omega)$ of an empty coil. From Eq. (3.4) it follows that the DC resistance of the coil is eliminated if one calculates the quantity of interest $L\text{-}L_0=(Z\text{-}Z_0)/j\omega$. As mentioned, by applying Eq. (3.2), the permeability can be derived.

In Fig. 3.5 an impedance measurement of coil nr. 3 (48 mm) with and one without a (typical) sample is presented.

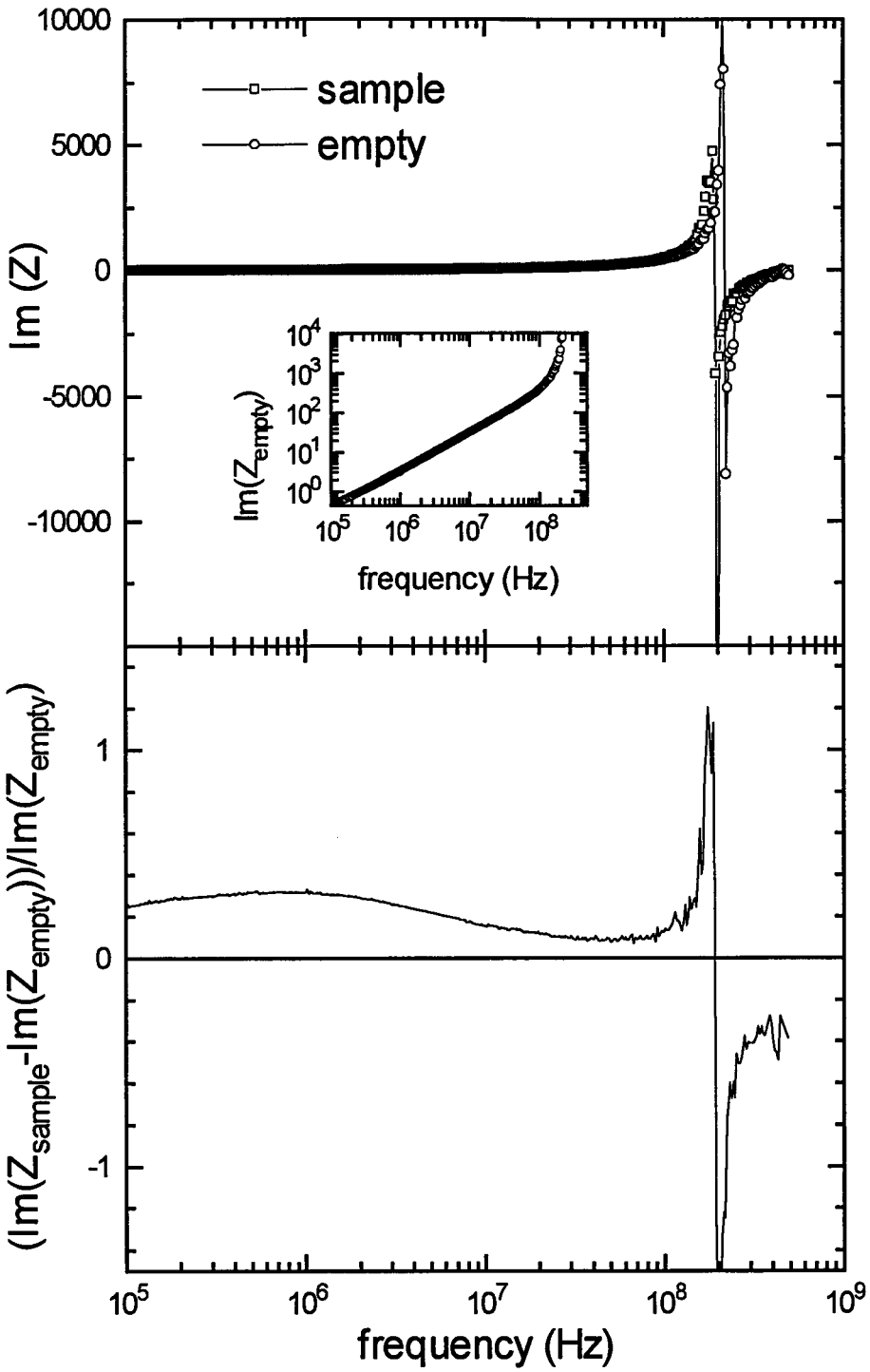

Fig. 3.5. Imaginary part of the impedance measured with the HF-set-up for a sample measurement and an empty measurement. Also the relative difference of the two impedances is shown.

From this figure it is obvious that the difference in the imaginary part of these impedances (which is directly related to μ') is very small. It may be clear that this is because we are dealing with thin films: only a minor part of the coil is filled with magnetic material. Moreover, one can see that at a certain frequency the impedance explodes and is not a straight line anymore which is to be expected keeping Eq. (3.4) in mind. What happens is that due to an electronic resonance, the impedance steeply increases. The most simple equivalence circuit to describe this frequency behaviour of the impedance is given in Fig 3.6.

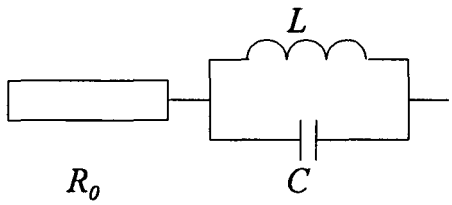

Fig 3.6 Equivalence circuit with stray capacity.

The resonance frequency of this circuit equals

$$\omega_{res}=\frac{1}{\sqrt{LC}}, \tag{3.5}$$

where C is the stray capacity of the coil or the coil with sample. Because the resonance frequency for both measurements (the one with and the one without sample) are not the same, an accurate determination of the permeability is not possible near this frequency. Only sufficiently below the resonance it is possible to determine μ. However, in order to do this one still has to eliminate the effect of the capacity from the measured impedance Z_{expt}: the impedance Z in which one is interested is related to the measured impedance by:

$$\frac{1}{Z}=\frac{1}{R+j\omega L}=\frac{1}{Z_{expt}}-j\omega C. \tag{3.6}$$

Which capacity must be taken into account and how this is measured will be discussed below.

A problem that arises is the fact that the capacity of an empty coil may not be equal to the capacity of a coil with a sample inside. In case of an empty coil, the capacitance appears between the turns of the coil. In case of a sample measurement, an additional contribution to the capacity appears, viz. between the wires of the coil and the surface of the conducting sample. Based on this, the capacity of coil with sample will be higher than the capacity of a coil without sample. This is, besides the larger inductance, because of the higher permeability, also a reason why the resonance frequency in Eq. (3.5) shifts to lower frequencies, see Fig 3.5. It is possible to take into account two different capacities in order to obtain the inductances from

the impedances. Another way is, to perform an empty measurement with a non-magnetic sample of the same dimension as the magnetic sample, as was done by v.d Riet [24].

We prefer a different method, which becomes clear after considering Fig. 3.7 in which the theoretical magnetization curve of a magnetic sample with uniaxial anisotropy is presented, when measured in the hard axis direction.

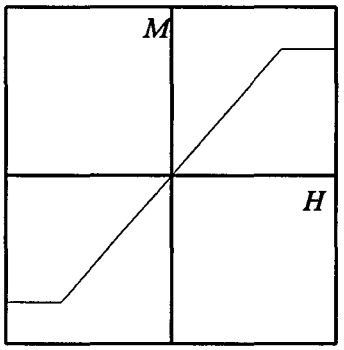

Fig. 3.7 Magnetization curve of a magnetic sample with uniaxial anisotropy measured in the hard axis direction.

At a certain magnetic field, the sample gets saturated. The magnetic susceptibility χ, which is the slope of this figure, is zero from this point on up to larger field and therefore the relative permeability μ_r equals one. This is the same value as for air or in other words, the empty measurements can be replaced by a measurement with a saturated sample. In practice this means that instead of an empty coil, a coil with the sample positioned in a magnetic field is used in the empty measurement option. After the empty measurement, the magnets which are used to saturate the sample, are taken away to perform the sample measurement. An advantage of this method is that the capacity, in both the empty measurement situation as well as the sample measurement situation, is the same. Additionally, there is the advantage of the avoidance of slight changes in the contact resistance between coil and test fixture when the sample is positioned inside the coil, which can influence the accuracy measurement. Namely, the coil will not be touched between the two measurements. In Fig 3.8 the holder of the magnets is shown schematically together with a coil with a sample within.

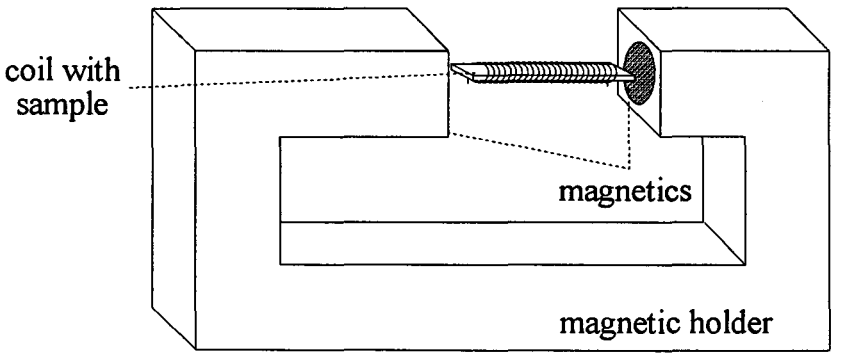

Fig. 3.8 Magnetic holder with a (saturated) magnetic sample positioned inside the coil.

Because the magnets are rather close to the coil, it is possible that some extra capacity is introduced, which would eliminate the advantages of this procedure. So, this method is only allowed if no significant extra capacity plays a role. Whether this is the case or not, can be examined with some frequency dependent impedance measurements. We performed two measurements. First an empty measurement (without magnets placed near the coil) and a second new empty measurement with the magnets placed around the coil. The difference in the imaginary part of the impedances of these two measurements is shown in the graph of Fig 3.9.

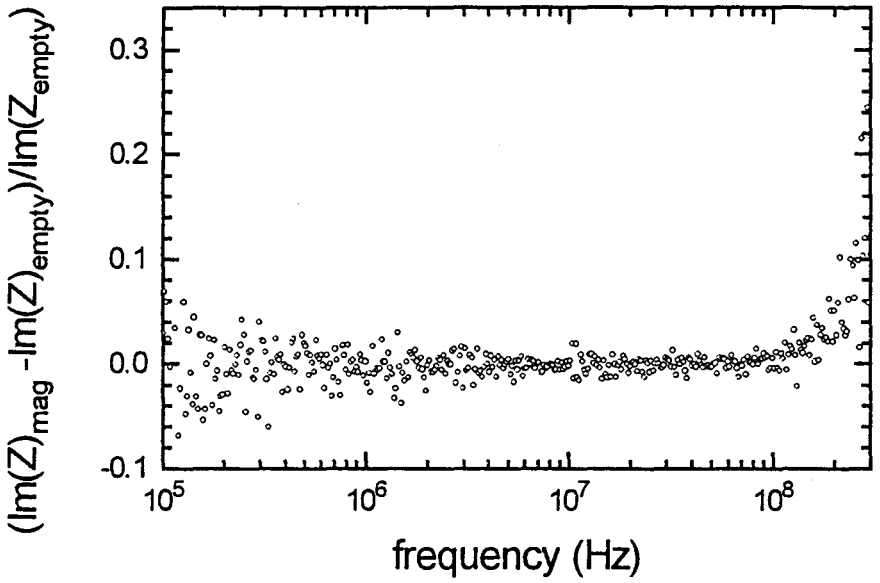

Fig. 3.9. Difference in the imaginary part of the impedance obtained from an empty measurement with an empty coil and a measurement performed with magnets placed around the empty coil.

We indeed conclude that for frequencies up to 200 MHz, the (relative) difference in the imaginary part of the impedance between the two measurements are rather small. So the effect of the extra capacitance related to the magnets can be neglected. It is obvious that the method with the saturated sample will lead to a different stray capacity than the method with the empty coil. This appears also from Fig 3.10 in which the imaginary parts of the two measurements are plotted. In the same figure, a fit based on Eq. (3.6) is given for the imaginary parts.

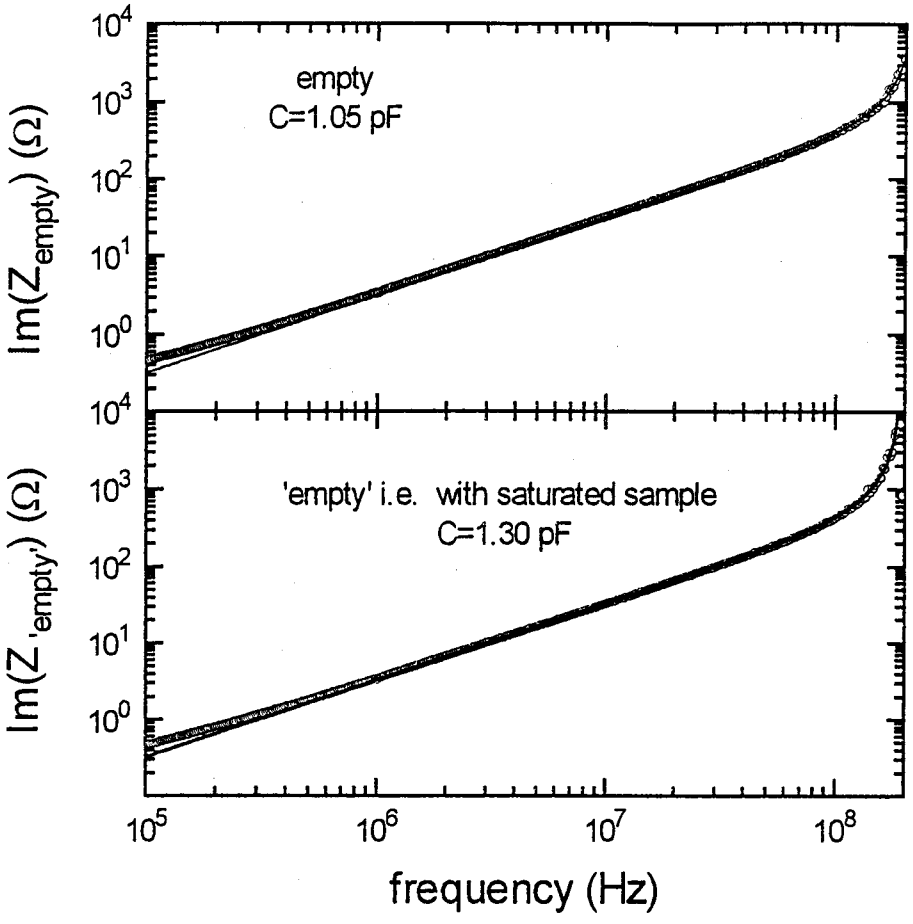

Fig. 3.10 Imaginary parts of the impedances for an empty coil (a) and for a coil with a saturated sample (b). The data points extracted from measurements are plotted together with a function that describes an inductance and a resistance in series, both parallel to a capacity.

From the true empty measurement, it follows that a stray capacity of 1.05 pF describes the impedance the best as distinct from the 'empty' measurement situation with the saturated sample which yields a capacity of 1.30 pF. The difference in both capacities finds its expression at frequencies above 10 MHz and becomes significant motivating again the necessity of the above correction scheme.

The stray capacity only plays role at high frequencies. This is the reason that there merely must be corrected in the HF set-up for this effect and that for the LF-permeability set-up used at Philips these corrections are not neccesary: the frequency range is between 10 kHz and 13 MHz. That the *C*-correction is important follows again from the next figure.

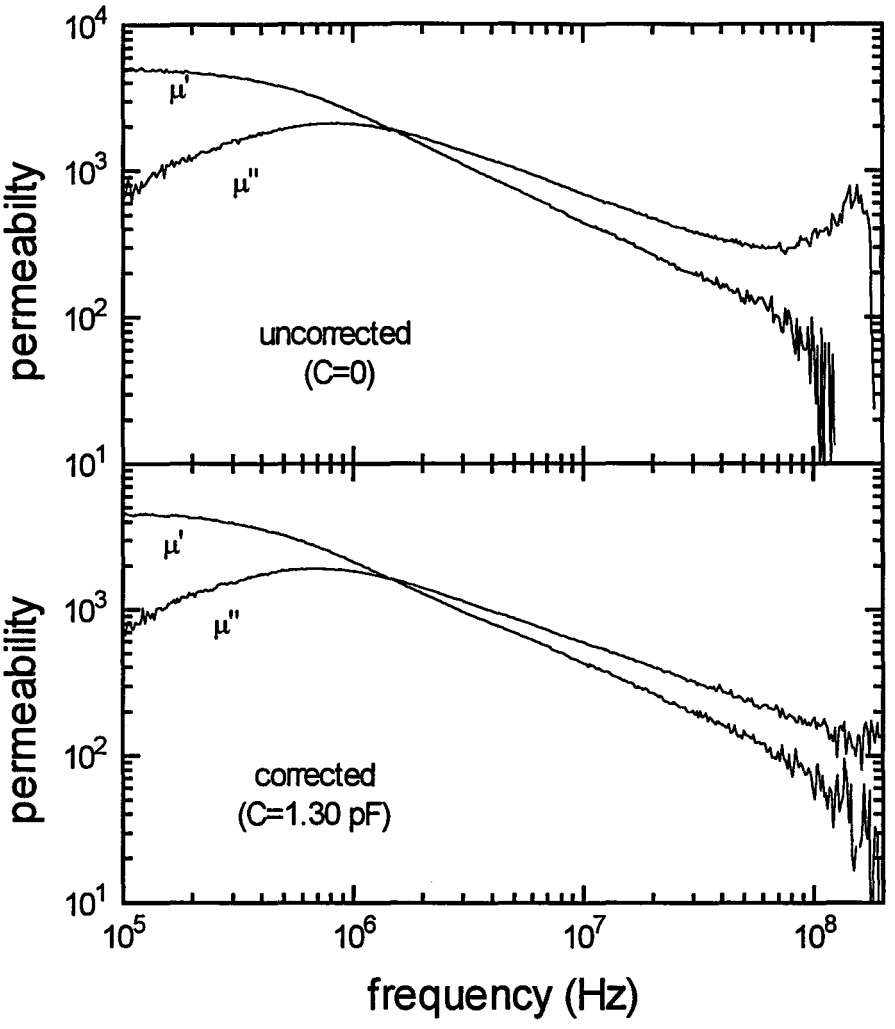

Fig. 3.11 Correction for stray capacities. Figure (a) is showing the complex permeability as follows from the impedance measurements using the simple equivalence circuit of Fig. 3.2, while Fig (b) represents the permeability as calculated with the equivalence circuit of Fig. 3.6.

In this figure the magnetic permeability as a function of frequency is shown for the case that one neglects the correction and for the case that it is taken into account. Because the total stray capacity is build up as the sum of the capacity between the turns of the coil, and the capacity between the wire of the coil and the film, it is self-evident that the capacity depends on the sample dimensions. For example, the capacity is expected to increase with increasing length of the sample.

Up till now only the low frequency behaviour of the coils is discussed to determine the validity of Eq. (3.1). To conclude this section we have to be able to perform permeability measurements up to 200 MHz, so a (better) fit of L and C is neccesary. Also the final parameters of the coil which we have used in the HF permeabilty measurements will be presented.

At the same manner as described above, the frequency dependent impedance of coil nr. 2 (41 mm) in table II is measured, again with a saturated magnetic sample with length 34 mm and width 5 mm. The imaginary part is plotted in Fig 3.12. Again a fit function is plotted that describes a resistance R_0 and an inductance L_0 in series, parallel to a stray capacity C. The two main fit parameters are L_0 and C because the resistance is very small (~0.5 Ω) and does not play a considerable role in the fit. On purpose, the inductance is left as a free parameter to create an extra degree of freedom in the high-frequency range. Fig 3.12(a) depicts the imaginary part of the experimental and the calculated impedance, while Fig. 3.12(b) shows the relative difference between the experiment and the fit.

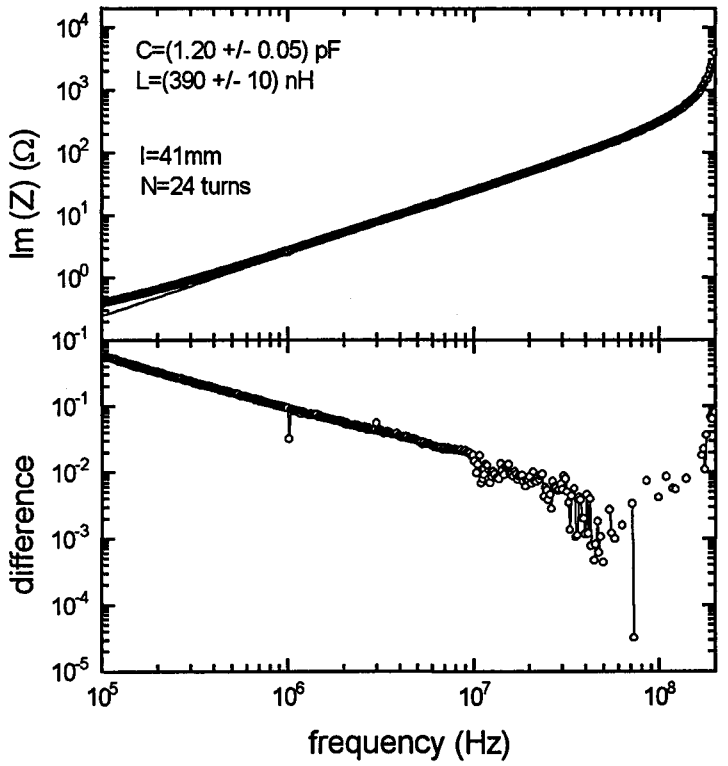

Fig. 3.12 Imaginary part of the impedance of a coil with length 41 mm and 24 turns, as follows from measurements by the HP-4195A spectrum analyser together with the best fit function (a). The relative difference between the measurement and the best fit function is depicted in (b).

The difference between the experiment and the fit, shows that at frequencies above 10 MHz the fit is good within 2%, while for low frequencies the discrepancy is somewhat larger. The best fit gives a capacity of 1.20±5 pF and an inductance L=390±10 nH. The inductance as derived from these experiments is slightly smaller than the previous result (table II), but it is within experimental accuracy.

The final coil parameters are shown in table III. It should be noted that the capacity is only reliable for a sample with dimensions 34 mm × 5 mm. The capacity is expected to increase with increasing sample area.

Table III Coil parameters of the coil used for permeability measurements at strips of 34 × 5 mm².

coil parameter	*value*
length	41.0±0.5 mm
cross sectional area	17.5±2.5 mm²
number of windings	24
inductance	390±10 nH
stray capacity	1.20±0.05 pF
resistance	0.5±0.1 Ω

All HF μ measurements presented in this report were obtained using these parameters.

3.5 Comparison of the HF and the LF set-up

At Philips research also use is made of a LF-set up, to perform impedance measurements to obtain the permeability. The frequency range is 10 kHz - 13 MHz. As mentioned in the previous section, correction for the stray capacity of the coil with the sample inside is not necessary for this frequency range. Because there is some overlap between the frequency ranges of both set-ups, it is possible to compare the permeability obtained with both equipments, see Fig 3.13.

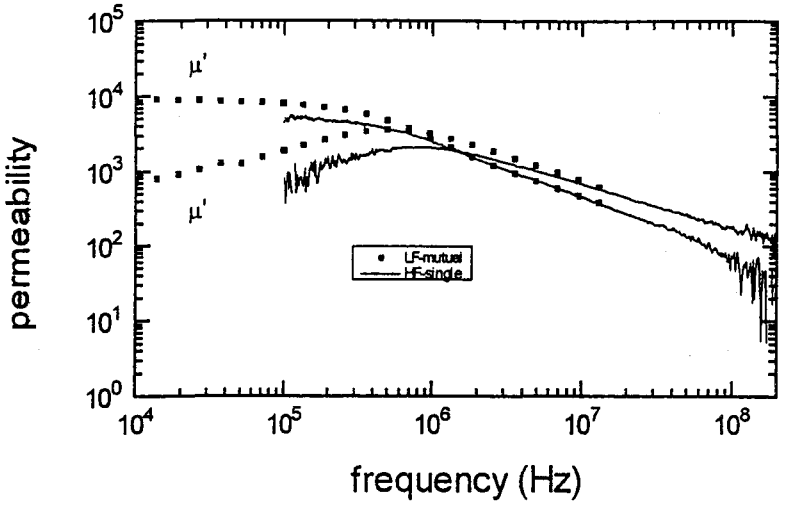

Fig. 3.13 Comparison of μ measurements performed with the HF- and the LF-permeability set-up.

There seems to exist some discrepancy between the permeabilities measured with the different equipments. This is not very strange when the different methods are regarded more precisely. The HF permeability set-up only uses a single coil. This coil serves to generate the current and the flux in the coil and is also used as a pick-up coil i.e. to detect the flux changes in the coil. The LF set-up on the contrary, commonly contains *two* coils, a long one to generate the field (the field coil) and a small one to pick-up the flux (the measuring coil). This forms an advantage of the LF equipment, because two opposite requirements can be formulated, which should be balanced. The first requirement is to aim at a homogeneous magnetic field in the coil and therefore also in the sample. Near the ends of the coil, the field is smaller, see Bernards *at al.* [24]. This implies that the average field applied to the sample is lower than expected. As discussed in section 3.2, there is an estimated correction for this effect. But if the length of the coil is small in comparison with the sample length, this correction becomes dominant which is not desirable. Based on this one would prefer as as long as possible coil. On the other hand, it can be argued that to length of the coil should be small compared to the sample length. This is connected with the fact that some flux lines originating from the sample close inside the measuring coil without being detected. As discussed in [24] one can correct for this effect already mentioned in section 3.2. This missing flux correction is smallest for long samples with a small demagnetizing field. Thus, the coil length has to be small compared with the length of the sample. These conflicting requirements are not easy to fulfil with one coil in the so-called 'single coil' mode such as used currently in the HF set-up. However, in the 'mutual coil' mode (used in the LF set-up) these aims can easily be pursued. A long coil is used to generate the magnetic field, while a second short coil is used to detect the magnetic flux. The latter coil is positioned inside the first one.

The aim for field homogeneity is easily fulfilled also in the HF set-up. The differences which appear from measurements originate from the missing flux correction C_f. Because of this correction factor which is sample dependent by the demagnetizing factor, there will always be a systematic difference in the permeability measured with the HF single coil set-up and the LF mutual coil set-up.

Commonly, the LF set-up is used in the mutual coil geometry. However, to compare the equipment of the LF and HF set-up more accurately, we have used the LF set-up with the single coil method (Up till now it is not possible to use the HF set-up in the 'mutual coil' mode). From permeability measurements it appears that the permeability is in agreement to a satisfactorily degree for both methods. Fig 3.14 compares the measurements performed on the two set-ups.

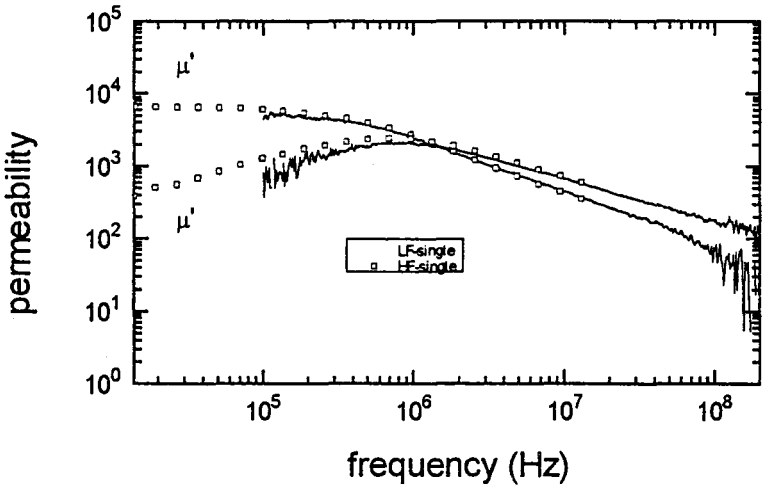

Fig. 3.14 Comparison of the permeability measured with the LF set-up and the HF set-up, both in the 'single coil' mode.

Finally, we present in table IV some experimental μ-data performed with three different procedures, viz. 1) the LF mutual coil set-up, 2) the LF single coil set-up 3) the HF single coil set-up. It seems that no significant differences between the LF-single mode and the HF-single mode appear

Table IV Comparison of permeability measured with different set-ups.

LF-mutual: μ'(100kHz)	*LF-single: μ'(100kHz)*	*HF-single: μ'(100kHz)*
778	791	1007
2603	2247	2410
3619	3174	3336
6242	5012	5222
12794	10694	9717

3.6 Conclusions and recommendations

Because of the correction of the stray capacity, the HF permeability set-up is able to measure frequency dependent magnetic permeabilities up to 200 MHz. This allows one to investigate e.g. eddy currents and ferromagnetic resonance, which play a role at high frequencies. This has been the main motivation to extend the frequency range which used to be up to 13 MHz for the LF set-up. Additionally it can also be utilized for frequency dependent resistances up to 500 MHz, which is the limit of the HP-4195A. The HF permeability set-up and the LF permeability set-up give almost identical permeability results, when both are used in the 'single coil' mode. As distinct from the LF permeability set-up, the LF permeability set-up is able to use the more accurate 'mutual coil' method, in which one coil is used to generate a magnetic field, while the other coil is used to detect the flux changes in the coil. They give comparable results. The relatively small systematic differences are due to an error made in estimating the missing flux correction factor C_f in the case of a single coil. Currently the frequency range in which reliable μ measurements can be performed is limited by the electronic resonance of the used coil. One way to eliminate the resonace by shifting it to higher frequencies is to diminish the stray capacity. One possible way to achieve this is to use a sort of waveguide instead of a simple coil.

4 Other experimental techniques

4.1 Introduction

In this chapter the experimental techniques, which were not reviewed in the previous chapter, are briefly discussed. Section 4.2 gives a review of the preparation of thin films, including the reactive sputtering and the annealing treatment. Although the description is given in the special case of FeHfO thin films, it is a general description which also suffices for other similar materials. Section 4.3 describes the magnetic characterisation (BH-loop and magnetostriction measurements) and section 4.4 the electrical characterisation techniques. Finally, in section 4.5 a structure analysis technique, X-ray diffraction, is briefly discussed.

4.2 The preparation of FeHfO thin films

4.2.1 Reactive sputtering

One of the deposition methods that is quite often used in research and production is reactive sputtering. By means of this technique it is possible to deposit thin films of metals, metal-oxides, -nitrides and -carbides on a substrate. The principle of the technique is as follows: By applying a large constant negative voltage at the target (cathode) and by grounding the substrate (anode), electrons will be accelerated to the substrate, on their way colliding with Ar atoms to form Ar^+ ions and other (secondary) electrons. Consequently, an Ar plasma will be formed, with a degree of ionisation of about 10^{-4} [25]. The positive ions will be accelerated to the target where various processes can occur. Apart from reflections of the ions, emission of radiation and structural rearrangements at the target surface, bombarding ions may be implanted in the target which can result in the ejection of deposition material or the release of secondary electrons. The secondary electrons will make the glow discharge self-sustaining. The released material condenses on a substrate to form a thin film. The bombarding particles must be inert to avoid chemical reactions on both target and substrate, which is the reason why argon (Ar) is often used. Additionally, it is possible to insert some reactive gasses such as oxygen (O_2) to promote *reactive sputtering*.

When the sputtered atoms reach the substrate, they are absorbed and diffuse across the surface until evaporation or junction with other atoms takes place. The growth of the film occurs by nucleation of a few atoms which start to form clusters, which can grow to a sort of metastable islands. At last they shall coalesce and form a continuous thin film. The process of sputtering can be influenced by varying the total pressure, the partial pressure of the reactive gasses and the applied power.

The simplest way to sputter is by applying constant negative voltage difference. This is so-called *DC diode sputtering* which will not be discussed here, because it is hardly used nowadays. A more common and more efficient method to deposit thin films is *RF diode sputtering*. By superimposing a high frequency AC voltage (MHz region) on the DC voltage, it

is possible to obtain a higher ionisation efficiency. This is because it takes a longer way for the electrons to travel to the substrate, so they can collide with more Ar atoms to form ions. Therefore lower pressures are sufficient to get a self-sustaining plasma. Additionally, with DC sputtering it is not possible to produce insulators. For more thorough discussions of the technique of sputtering we refer to [26].

The deposition of all the FeHfO thin films in this report is done in a Perkin-Elmer 2400 RF diode sputtering system, which is shown schematically in Fig. 4.1.

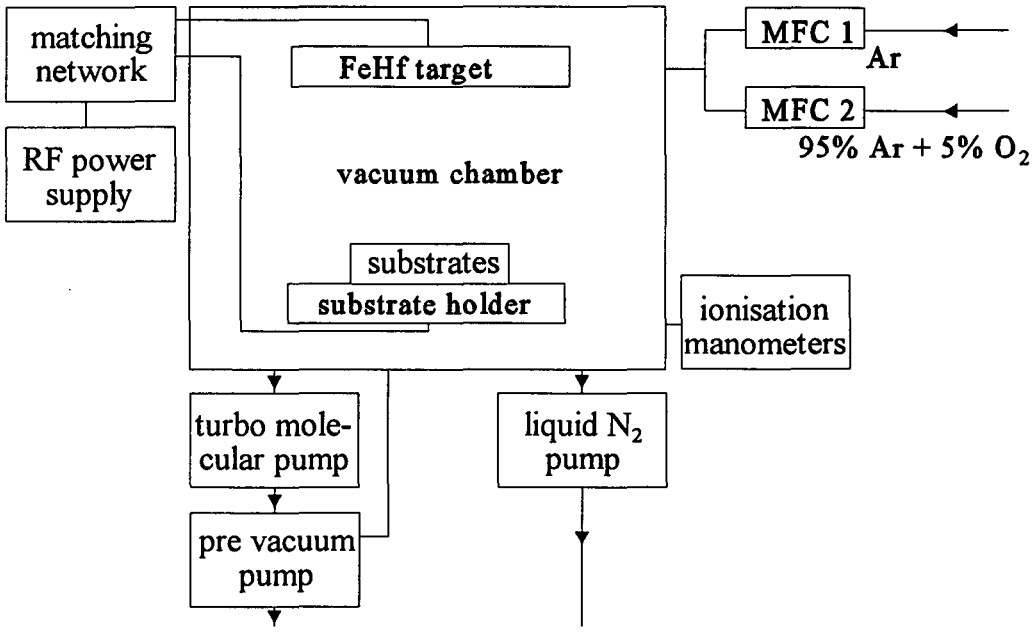

Fig. 4.1 The Perkin Elmer sputtering model 2400 utilized for RF reactive sputtering.

The vacuum chamber is evacuated by means of a roughing pump, a turbo molecular pump and a liquid nitrogen trap/pump to a base pressure below $5 \cdot 10^{-7}$ mbar. The pump speed can be controlled by a throttle valve between the turbo pump and the chamber, because a too high pressure can cause turbulence. A 13.56 MHz RF generator supplies the power for the glow discharge of the plasma, controlled by a Randex matching network and a power stabiliser. This matching network contains variable resistances, inductors and capacities. The power supply is variable which is necessary to control the deposition rate of the films. A circular 15 cm diameter water cooled FeHf alloy target with 83.3% Fe and 16.7% Hf is used to sputter. The distance between the target and the substrate is about 5 cm. Oxygen and argon flow rate ratios are adjusted for each deposition to vary the incorporation of oxygen in the films. Two gas inlets are utilized for this goal: one inlet for Ar with a maximum flow of 100 sccm[1] and one with a mixture of 95% Ar and 5% O_2 with a maximum flow of 20 sccm. The gas flows are

[1] sccm: standard (273 K, 1 atm) cubic centimetre per minute.

mixed before entering the chamber and adjusted by the two mass flow controllers. Pressures above 10^{-3} mbar are measured with an MKS controller and lower pressures are measured with a Balzers IMG 060B ion gauge controller. The total pressure of the system is for the depositions in this report typically 4 to 5 mbar, dependent on the gas flow rates.

The thin FeHfO films were deposited on D263 glass or on silicon (Si) substrates with a thermal SiO_2 layer of 0.3 μm thick. The glass substrates are cleaned in a sequence of six different baths containing 1) an alkaline soap, 2) running water, 3) an acid soap, 4)+5) (demi) water and 6) again in running demi water. Here, both soap baths were at a temperature of about 70 °C. Both the glass and silicon substrates have dimensions 5 × 34 mm^2 to facilitate accurate and easy magnetic measurements. The thickness of the glass is about 0.33 mm and the thickness of the silicon is about 0.54 mm. Too thick substrates may hinder accurate magnetostriction measurements.

Before the sputtering can start, the target is commonly *presputtered* to remove absorbed gasses. We used typically 30 minutes because the system had no load-lock and prior to each deposition the system needed to be exposed to air to load the substrates. After the pre-sputtering of the target, the substrates are sputter *etched* in argon (without reactive gasses such as oxygen) for 2 minutes again with the purpose of removing absorbed gasses. During the latter process, the substrate serves as a matter of speaking as a target. The substrate bias voltage is now -30 V and the power supply is now chosen to give 300 W. During *sputtering* the target voltage is -200 V and with the power supply at 500 W films are produced with growth rates of 0.7 to 0.8 μm per hour.

4.2.2 Annealing

After the deposition the as-deposited samples receive an annealing treatment in a magnetic field to induce uniaxial anisotropy, see the requirements discussed in chapter 1. During annealing in a magnetic field actually several processes involving rearrangements of atoms may occur: By heating, crystallisation of Fe is promoted. Also precipitation of Hf atoms from Fe crystallites is expected to take place since Hf only has a very limited solubility in Fe. Furthermore, Fe, Hf and O atoms may form HfO_2 and Fe_2O_3. Apart from this, rearrangement of atoms in pairs due to the magnetic field is expected to take place. This latter mechanism provides uniaxial anisotropy. By rotating the sample in the field, after it has been given an anneal treatment in a static field, the net anisotropy can be reduced. Annealing in zero field will stabilize a random domain structure by inducing uniaxial anisotropy locally parallel to the magnetization within the domains.

Besides the conventional classical thermal processing (CTP) based on resistive heating which has not been used here, there is another method of annealing: rapid thermal processing (RTP). It is this method that has been used to anneal our samples. In contrast with CTP, RTP is based on heating by radiation. The advantage is that the efficiency of the power supply is higher: all the energy will be supplied to the sample, instead of the surrounding walls. At Philips Research in Eindhoven, an AST Elektronik SHS 1000 MA prototype RTP reactor is used for the annealing treatments [27]. The applied magnetic field provided by an electromagnet is approximately 48 kA/m. In a few seconds the sample can be heated up to the desired temperature, because annealing based on radiation is a very effective method. Heating rates are typically 10 °C/s. By means of a rotor, it is possible to do annealing treatments with a

rotating sample in a constant magnetic field. In the present work we used a static rotor unless stated otherwise. The annealing treatment in the case of rotating field annealing is shown schematically in Fig. 4.2.

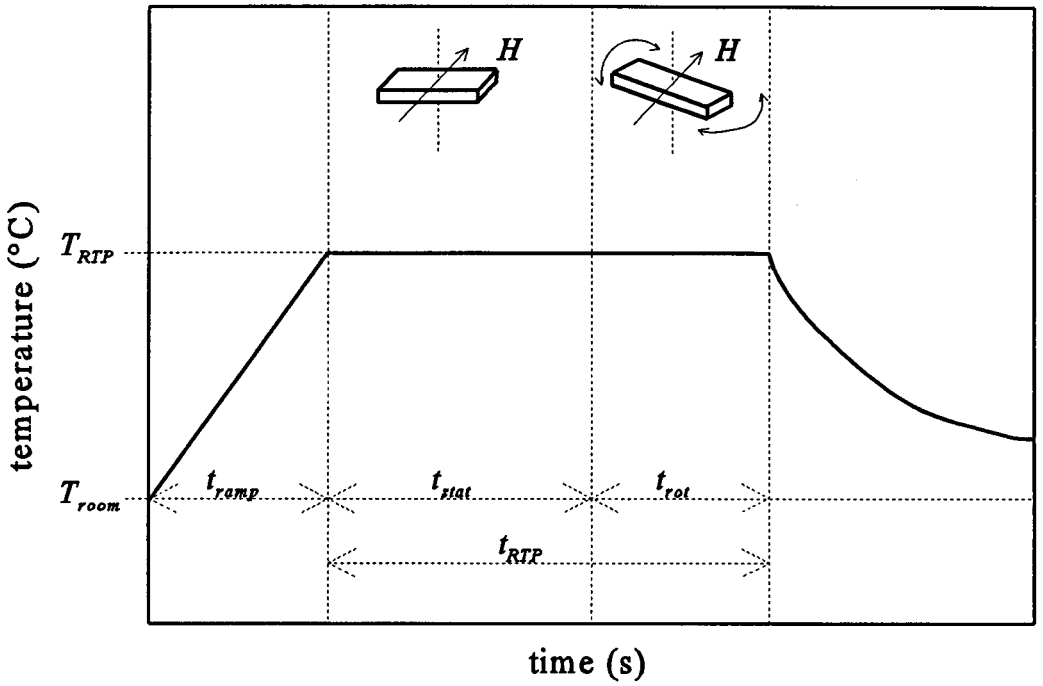

Fig. 4.2 Schematic representation of the annealing treatment in a rotating magnetic field.

This figure depicts the temperature as a function of time. During the first stage, the ramping stage t_{ramp}, the temperature will raise from room temperature up to the desired annealing temperature. The next stage is divided in two sections: during a certain amount of time t_{stat} the sample will be positioned in a static field and during the remainder of the annealing time t_{rot}, the sample will be rotated in the magnetic field. Both sections take place at a certain constant temperature T_{RTP}. During the final stage, the heating power supply is shut down causing the sample to cool down to room temperature T_{room}.

4.3 Magnetic characterisation

4.3.1 BH-loop measurements

A simple method to measure the hysteresis loops (the magnetic induction B as function of the applied magnetic field H) of soft magnetic material will be discussed here. In principle, this technique is not much different from the set-up of the magnetic permeability (see chapter 3) in the mutual set-up. Two coils are used for this aim: a primary coil generates a magnetic field and a secondary coil will pick up the response of the magnetic sample (Fig. 4.3).

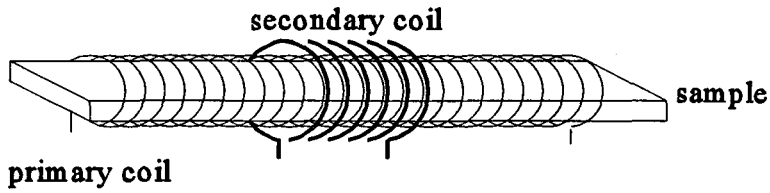

Fig. 4.3 Measurement circuit of the BH loop measurements.

A low frequent AC current produces a time dependent magnetic field in the primary coil. The secondary coil (n_2 turns) will pick up an induction voltage

$$V_{ind,\,2}(t) = -n_2 \frac{d\Phi}{dt}, \tag{4.1}$$

with Φ the time dependent magnetic flux in the secondary coil caused by both the field of the primary coil *and* the sample contribution. In the set-up used at Philips Nat. Lab. the primary coil is positioned inside the secondary coil. Another possibility is to connect both coils by a magnetic core as was done by Schmidt *et. al.* [28]. The magnetic flux depends on whether there is magnetic material in this secondary coil or not. Two measurements have to be done: firstly, a sample is put inside the secondary coil. Then the measured induction is equal to

$$V_{ind}^{sample} = -n_2 \frac{d}{dt}[BA + B_{air}(A_{coil} - A)]. \tag{4.2}$$

Here, B is the magnetic induction in the film, B_{air} is the magnetic induction in the air, A the cross sectional area of the film, and A_{coil} is the cross sectional area of the secondary coil. Afterwards an empty measurement is done, leading to an induction voltage given by:

$$V_{ind}^{empty} = -n_2 \frac{d}{dt}[B_{air} A_{coil}]. \tag{4.3}$$

Eliminating the magnetic induction in the air B_{air} by combining the above equations, leads to an expression for the time derivative of the magnetic induction in the sample, equal to

$$\frac{d}{dt}B(t) = \frac{1}{n_2 A}\left[V_{ind}^{empty}\frac{(A_{coil} - A)}{A_{coil}} - V_{ind}^{sample}\right] \tag{4.4}$$

V_{ind}^{sample} and V_{ind}^{empty} are measured to determine $B(t)$. On the other hand, $H(t)$ is known from $H(t) = n_1 i(t)/l_1$ in which $i(t)$ represents the current through the primary coil which in turn is

obtained by measuring the voltage $V_1(t)$ across a known resistance (R=1 Ω), which is in series with the primary coil: $i_1(t)=V_1(t)/R$. By integrating Eq. (4.4) and combining with the magnetic field $H(t)$ the hysteresis loop $B(H)$ can be determined. The equipment for the BH loop measurements is shown schematically in Fig. 4.4.

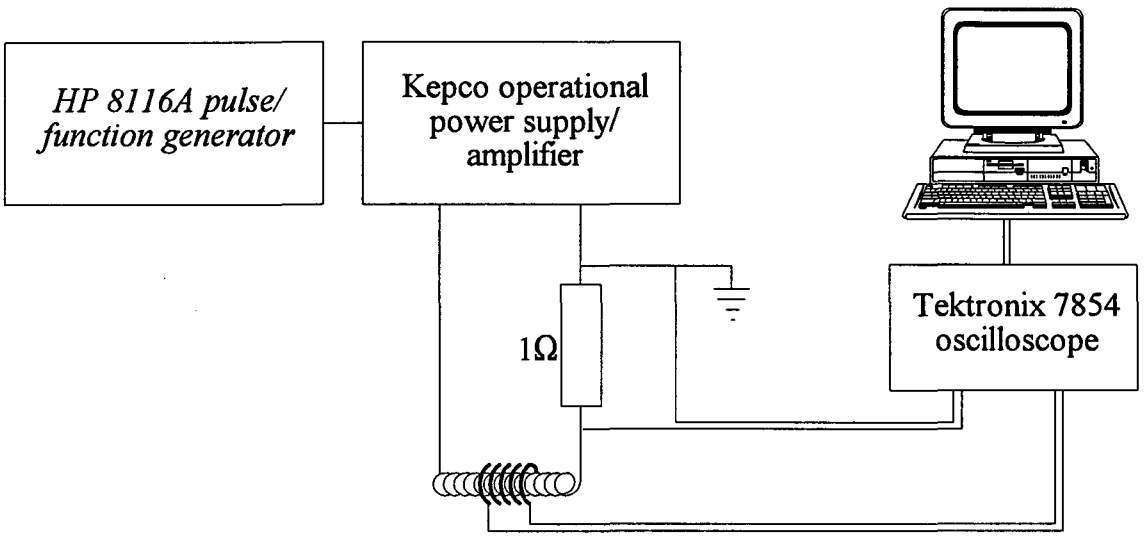

Fig. 4.4 Equipment for BH loop measurements.

A HP 8116A pulse/function generator produces an alternating voltage with a frequency of 160 Hz, which is applied by means of a Kepco operational power supply/amplifier. This voltage is applied to the primary coil and the 1 Ω resistance. The Tektronix 7854 oscilloscope is used to measure and store the data of $V_1(t)$ and the induction voltages. The integration of the induction voltages and the calculations are also done by the storage oscilloscope, including the determination of the saturation magnetic induction, the remanence, the coercivity and the uniaxial anisotropy constant. After these operations, the data are transferred to the HP computer. A typical magnetization loop for a 2.1 μm thick FeHfO film with dimensions 34 mm × 5 mm is given in Fig. 4.5.

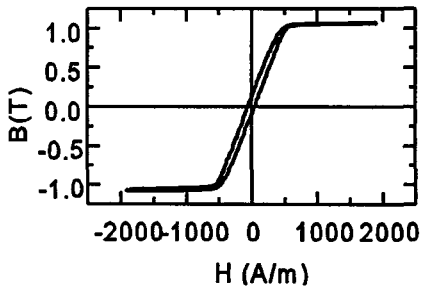

Fig. 4.5 Typical magnetization loop of a FeHfO thin film with dimension 34 mm × 5 mm × 2.1 μm annealed at 400°C.

4.3.2 Magnetostriction measurements

Magnetostrictive stresses are frequently determined by measuring the deflection of a film deposited on a substrate. When a magnetic film is saturated (magnetized) in a certain direction it will undergo a length change because of magnetostriction. This length change in turn will cause the film to bend. It is possible to derive a relation between the saturation magnetostriction constant λ_s and the deflection D of the film [28]:

$$\lambda_s = D\frac{E_s t_s^2}{E_f t_f}\frac{2}{9l^2}\frac{1+\nu_f}{1+\nu_s}, \tag{4.5}$$

where E_f and E_s are the Young's moduli, t_f and t_s are the thicknesses and ν_f and ν_s are the Poisson ratios of the film and the substrate, respectively. The Poisson ratios are often assumed to be equal. Further, l is the distance from a fixed end to the point at which the deflection is measured. Some relevant Young's moduli are represented in table V.

Table V. Some relevant Young's moduli.

Material	*Young's modulus E (GPa)*
glass D263	72.9
Si	208
GGG	225
nano-Fe	≈100

The experimental set-up to measure the saturation magnetostriction is illustrated in Fig. 4.6.

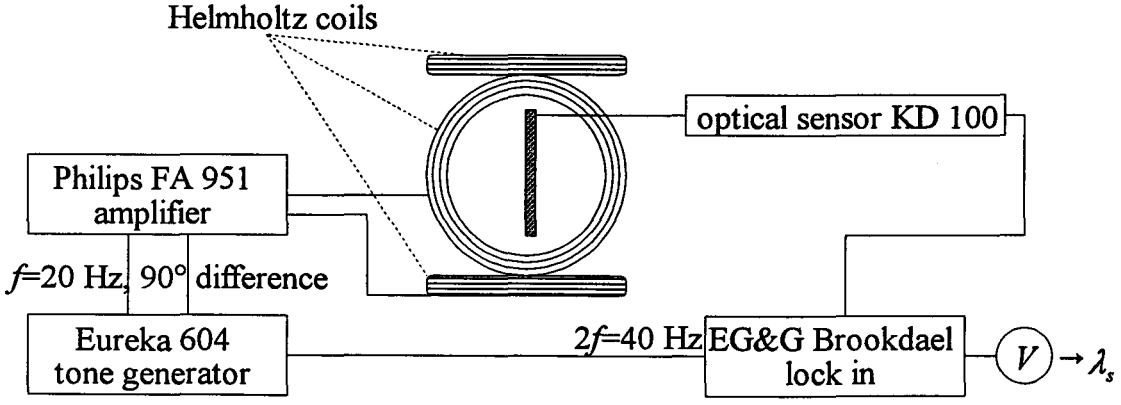

Fig. 4.6 Schematic representation of the equipment to measure the saturation magnetostriction.

A strip of magnetic material on a substrate is fixed at one end. In the present set-up l=28 mm. The Eureko 604 tone generator produces two sinusoidal currents with a phase difference of 90° and a frequency f=20 Hz, which are amplified by a Philips FA 951 amplifier and directed towards two sets of Helmholtz coil pairs which have their axes mutually perpendicular to each other. These produce a rotating magnetic field in the plane of the film. The field must be large enough to saturate the sample since we want to measure the *saturation* magnetostriction constant. The field strength is typically 2 kA/m. Due to the rotating field, the length of the sample will periodically change because of the magnetostriction (section 2.2). Because of the uniaxial symmetry of the magnetostrictive length change, a positive and a negative field in a certain direction give the same deflection, i.e. the deflection of the sample changes with the double frequency: $2f$ (see Fig. 4.7).

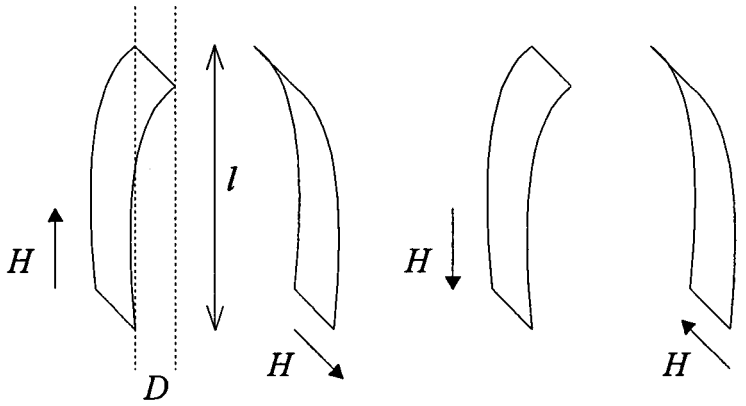

Fig. 4.7 Magnetostriction measurements: deflection D of a strip fixed at one end, due to a rotating magnetic field.

A very sensitive optical sensor KD 100 transfers this small deflection into a voltage. The output voltage is proportional with the deflection, the proportionality constant being 3.9 nm/mV. This rms[2] voltage is measured with a two phase EG&G Brookdael lock in analyser at a frequency $2f$ and should be multiplied with a factor $2\sqrt{2}$ to obtain the peak-peak[3] voltage. The sign of the output voltage is the same as the sign of the saturation magnetostriction.

[2] rms = root mean square.

[3] difference between maximum and minimum.

4.4 Electrical characterisation

4.4.1 Resistivity

The specific resistivity ρ of a material is related to the macroscopic resistance R by

$$R=\rho\frac{l}{A}=\rho\frac{l}{wt}, \tag{4.6}$$

where l is the length of the film in the direction parallel to the current, and $A=wt$ is the cross sectional area of the film. The sheet resistance R_s is defined as the resistance of a square film ($w=l$) with thickness t. By applying a certain voltage and measuring the current, it is possible to obtain a resistance. However, a better way to find an accurate value of the resistivity is to use the so-called *four-point method*: four probes are placed on the film in a line at an equal distance (Fig. 4.8).

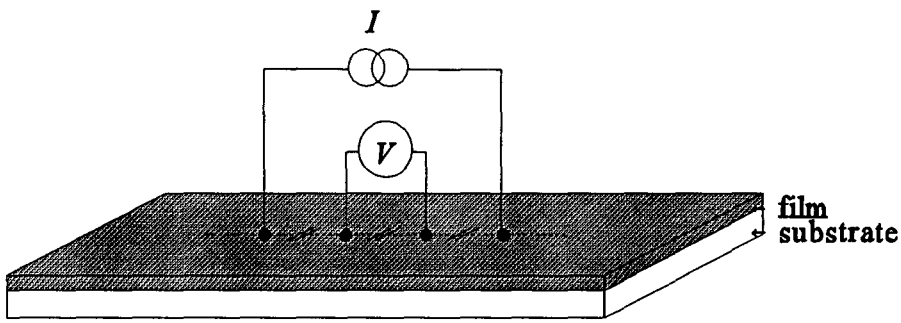

Fig. 4.8 Four-point method

The advantage of this method compared to the two-point method is that the voltage contacts are not the same as the current contacts so that the non-controllable contact resistance caused by the contact itself or the supply wires are not measured. A certain current source causes a current I to flow through the sample and the voltage V is measured between the two inner probes. The relation between the resistivity and the sheet resistance of the film will be [29]:

$$R_s=\frac{\rho}{t}=C\frac{V}{I}. \tag{4.7}$$

Here C is a dimensionless geometric factor which corrects for the non-uniformities in the current density. It depends on the sample dimensions as well as the distance between the contact probes. Moreover the probes must be regarded as point contacts which means that their diameter is much smaller than the distance between the contacts. For the data presented in

this report a VEECO Instruments Inc. EPP 5000 four-point probe meter was used to measure the sheet resistance. In this case the correction factor C equals 0.616 for films with dimensions 34 mm × 5 mm. From Eq. (4.7) it is possible to derive the resistivity.

4.4.2 Magnetoresistance measurements

The four-point method discussed above is also the basic starting-point of the equipment used to perform magnetoresistance measurements. In this case the distance between the outer contact probes is 7.5 mm. Fig. 4.9 shows a schematic representation of the set-up of the magnetoresistance measurements.

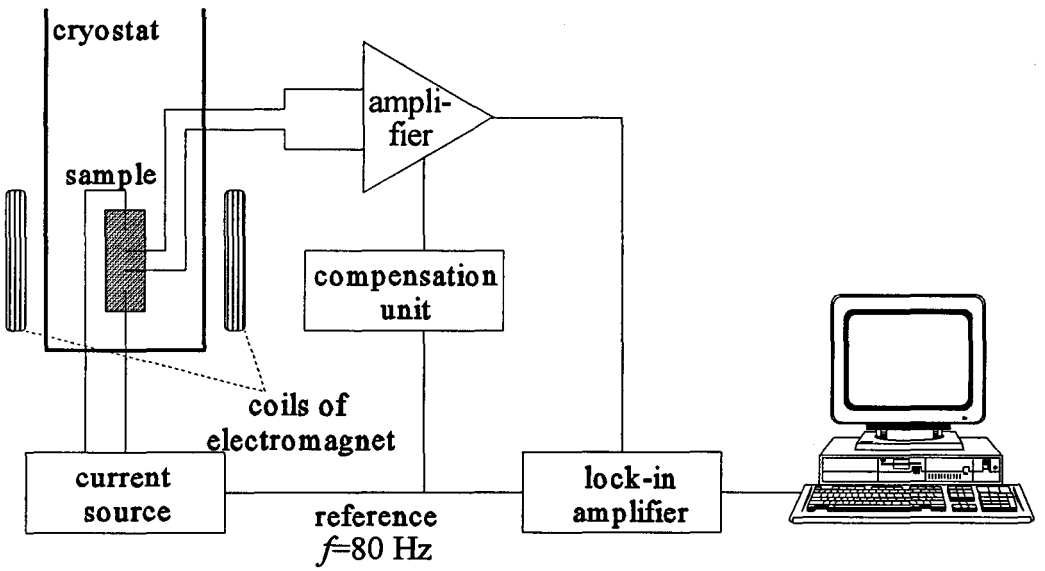

Fig. 4.9 Schematic representation of the set-up of the magnetoresistance measurements.

A current source is connected to the outer pressure contacts on the sample while the output voltage is measured via the two inner probes. The sample is positioned between two coils of an electromagnet. A sweep generator can vary the magnetic induction between 0 T and ±1.35 T. The direction of the magnetic field can be aligned parallel or perpendicular to the applied current, but it is always in the plane of the film. To obtain a high signal-to-noise ratio, the lock-in technique is used. Firstly, the output voltage in zero field is measured. Then a compensation unit is compensating for this voltage. The voltage variation around zero in field can now be measured more accurately and is amplified by a factor 100 or 1000. The reference frequency used is 80 Hz. Finally, the data are transferred to a PC, linked to a Phydas system.

4.4.3 Temperature dependent (magneto)resistance measurements

The equipment described in the previous section can also be used to measure temperature dependent resistances. The sample is placed into a cryostat (Fig. 4.9) that can be filled with helium. By means of a heater which is positioned near the sample, the temperature can be varied between 10K and 350K. Now it is not only possible to measure temperature dependent resistivities, but also temperature dependent magnetoresistance measurements can be done.

4.4.4 Frequency dependent resistance measurements

In principle, the set-up used to measure magnetic permeabilities (chapter 3) also enables one to measure the frequency dependence of the electrical impedance or resistance of a thin film. The HP 4195A is able to measure at frequencies up to 500 MHz. The LABVIEW program used for the high frequency permeability measurements is suitable for this aim. The main difference is that the HP 41951-60001 impedance test adaptor is now connected to two probes which can be placed on a sample, rather than connected to a coil in case of a permeability measurement.

4.5 X-ray diffraction (XRD)

To determine the structure and texture of a film, a very useful and powerful method is X-ray diffraction (XRD). When a film is exposed to X-rays, constructive interference will occur when the difference in path length between two scattered rays is an integer number of wavelengths. When applied to a crystal lattice, this gives the so-called Bragg's law.

$$2d\sin\theta = n\lambda. \tag{4.8}$$

Here d is the interplanar spacing, θ is the diffraction angle and n is the order of interference which is a positive integer, and λ the wavelength of the used radiation (Fig. 4.10).

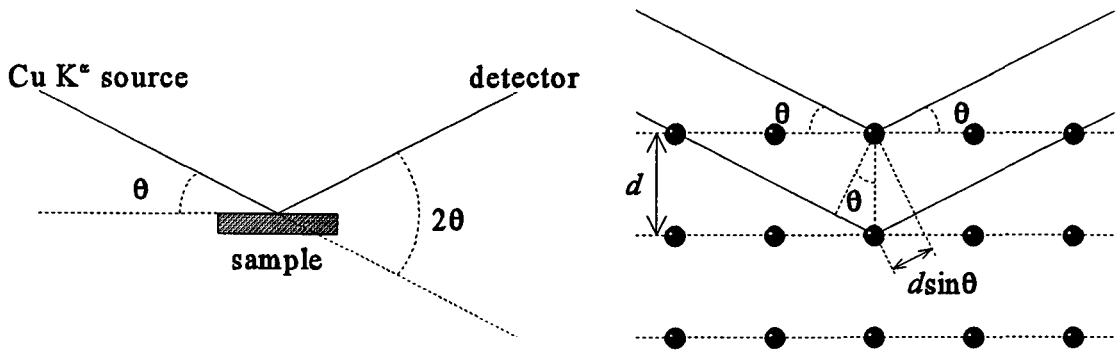

Fig. 4.10 Geometry of X-ray diffraction experiments.

The law describes at which angles peaks occur. The peak position in turn gives information about the spacing between the planes, in other words about the lattice constant *d* and about the texture. Unavoidably, in experiments the diffraction peaks are broadened by the apparatus and moreover by the material itself. For instance nanocrystalline materials contain small grains with average size $\langle D \rangle$. The Scherrer equation describes the dependence of the peak width, in the ideal case of no apparatus broadening, on the average grain size [30]:

$$\langle D \rangle = \frac{0.9\lambda}{\Delta\theta_{FWHM}\cos\theta_B} \tag{4.9}$$

Here θ_B is the Bragg-angle and $\Delta\theta_{FWHM}$ is the peak broadening, or more precisely the full width at half maximum of the diffraction peak. The broadening caused by the apparatus can be neglected for the experiments presented in this report, because here the peak broadening is dominated by the small crystallites. In our case, the XRD experiments were performed on a Philips PW 1800 diffractometer and the X-rays are emitted by a copper target that is bombarded with high energy (40 keV) electrons. The X-rays are Cu K^{α} with a wavelength λ=1.5418 Å, and come from the deep level electrons of the Cu atom. By fitting the X-ray peaks with a Gaussian profile after subtracting the background radiation, its possible to obtain the distance *d* of the planes parallel to the surface and the grain size in the direction normal to the surface.

5 Results

5.1 Introduction / experimental

In this chapter the results of the investigation of the FeHfO thin films will be presented. The present section will give a brief review of the sputtering characteristics such as pressure, gas flows and used target. Furthermore, the XRD results of some films are presented yielding information on the texture, lattice parameters and the size of the crystallites. A summary of the composition of some investigated samples, which will be discussed in this chapter, are also presented. Section 5.2. will give some magnetic properties of a typical FeHfO thin film, such as the BH loops and the magnetic permeability. To obtain good soft magnetic behaviour of FeHfO, some additional experiments were performed. Firstly, the influence of the throttle valve in the sputtering machine (see section 4.2) on the magnetic properties was investigated. Secondly, the effect of the addition of the elements Cu and Si to the FeHf target was examined. Both influences come up for discussion in section 5.4. Section 5.5 describes an important part of this work, namely the frequency dependent magnetic permeability. Finally section 5.6 presents some electrical transport studies on the FeHfO films, including the giant magnetoresistance (GMR) and temperature dependent resistance.

The sputter conditions during the three stages (presputtering, etching and sputtering) are summarized in table VI. Additionally, the composition of the target, the base pressure and the used substrates are given. Further details on the sputtering process can be found in section 4.2.1.

Table VI. Sputter characteristics

target composition		$Fe_{83.3}Hf_{16.7}$	
base pressure (mbar)		$\leq 5 \cdot 10^{-7}$	
substrates		glass, Si/SiO_2	
conditions	*presputtering*	*sputter etching*	*sputtering*
RF power (W)	500	300	500
target bias (V)	200	0	200
substrate bias (V)	0	-30	0
gas flow #1: Ar (sccm)	10-60	10-60	10-60
gas flow #2: 95%Ar/5%O_2 (sccm)	40-75	0	40-75
process presure (mbar)	3-4	2-3	3-4
process time (min)	30	2	60-900

After sputtering the so-called *as deposited* samples were annealed in a constant magnetic field of 48 kA/m along its short axis at 400 °C during 5 seconds. This rapid thermal processing (RTP) has been briefly described in section 4.2.2. Table VII gives a summary of the prepared samples which are investigated and discussed in this report. In this table also the type of experiments performed on the respective films are indicated, including the section(s) in which they are discussed. The composition of some samples resulting from Rutherford backscattering measurements (RBS) or surface electron microscopy (SEM at the Eindhoven University of Technology) are also given in this table.

Table VII. Summary of the samples discussed in this report. The films of group 3 to 6 are sputtered with the throttle valve completely open to diminish the background pressure during sputtering in contrast to the films of group 1 and 2.

group nr.	*typical* chemical composition*	*analyses*	*Ar flow (sccm)*	*Ar/O_2 (sccm)*	*experiments (section)*
1	FeHfO		10-45	9	electric./magn. properties(5.3), $\mu_r(f)$ (5.5)
2	$Fe_{51}Hf_{10}O_{39}$	RBS	30	8-13	electric./magn. properties (5.3)
3	$Fe_{48}Hf_{10}O_{42}$ $Fe_{52.5}Hf_{11.7}O_{35.8}$	RBS SEM	42.8	11-13	electric./magn. properties (5.4)
	$Fe_{46.6}Hf_{10.0}O_{43.4}$	SEM	42.8	12-13.4	GMR (5.6)
	FeHfO		42.8	12	RTP temperature (5.3), $\mu_r(f)$ (5.5)
	FeHfO		42.8	11, 12	rotating sample during RTP (5.4)
4	FeHfCuO		42.8	9-14	electric./magn. properties (5.4)
5	FeHfSiO		42.8	8-15	electric./magn. properties (5.4)
6	FeHfSiO		27.5-67.5	10	electric./magn. properties (5.4)

* *'Typical' means a sample with good soft magnetic behaviour or large GMR effect. The differences between RBS and SEM can be explained by the fact that the error in the O concentration can be as large as 10% absolute, in case of RBS.*

The XRD patterns representing the intensity as function of the double angle 2θ together with the lattice parameters and grain sizes are shown in Fig. 5.1 to 5.5. Fig. 5.1(a) shows the XRD results of some FeHfO films of group 2 in table VII, prepared with different Ar/O_2 flows. The (110), (200) and (211) peaks of α-Fe are visible; in polycrystalline materials there is a random texture. The broad peak near 33° is attributed to an amorphous FeHfO phase. Further, no peaks of HfO_2 or Fe-O phases can be identified. By applying the Bragg law (Eq. (4.8)) to the position of the Fe(110) peak in the several measurements one obtains the (110) interplanar distances. These are collected in Fig. 5.1(b). By using the Scherrer equation (Eq. (4.9)) it is possible to derive the grain size of the Fe crystallites from the peak broadening. These results are shown in Fig. 5.1(c).

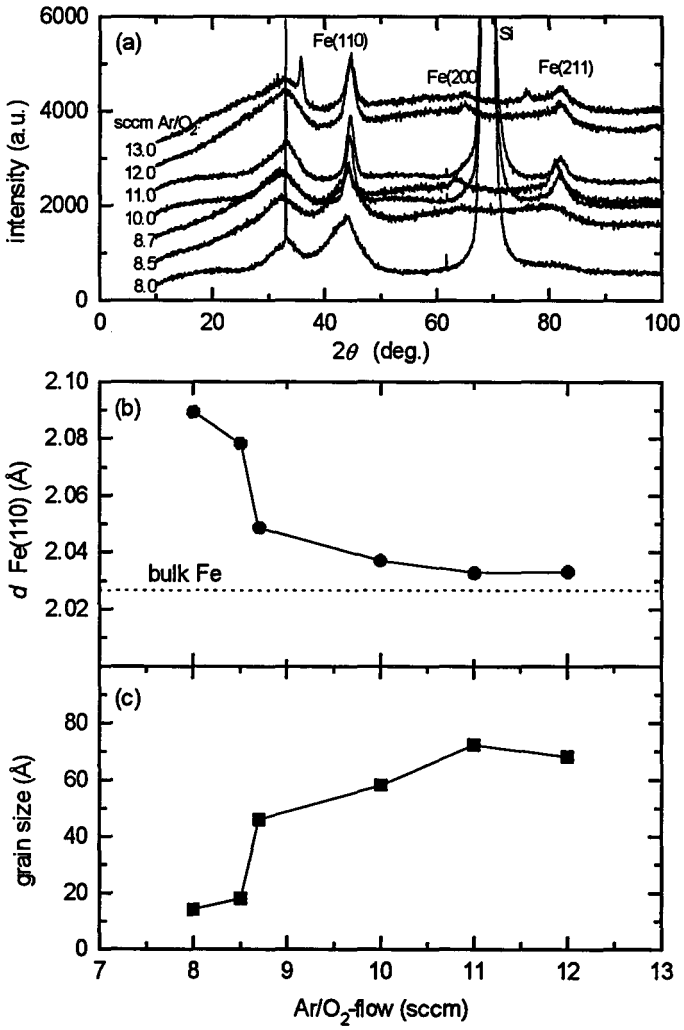

Fig. 5.1 (a). Typical XRD patterns (Cu K^{α} radiation) of FeHfO thin films for different argon/oxygen flows. The large peak at near 68° is a Si peak from the substrate. It only appears for samples grown on the Si/SiO_2 substrates. The Fe (110) peak becomes more narrow for higher Ar/O_2 flows. (b) represents the (110) interplanar spacing of the α-Fe and (c) the grain size of the Fe crystallites as a function of the argon/oxygen flow.

Figure 5.1(b) shows that the interplanar spacing between the Fe(110) planes decreases with the flow indicating a decrease in the Fe lattice parameter. The gradual decrease above 8.5 sccm Ar/O_2 might be due to the dissapearance of Hf out of the Fe crystallites into the amorphous phase to form HfO_2. We note again that the samples are annealed. However, the steep decrease at about 8.5 sccm Ar/O_2 probably has a different origin. A possible explanation is that the samples become ferromagnetic at room temperature, for flows larger than 8.5 sccm, which leads to a non-zero magnetization M. Consequently, the lattice parameter changes via the magnetostriction. It is surprising that the grain size (Fig.5.1(c)) increases with the Ar/O_2 flow and thus with the concentration of O in the FeHfO film: it was expected that O promotes the amorphous phase, which might be at the expense of the size of the Fe crystallites.

We have also prepared FeHfO films at various Ar flows. The results are shown in Fig. 5.2.

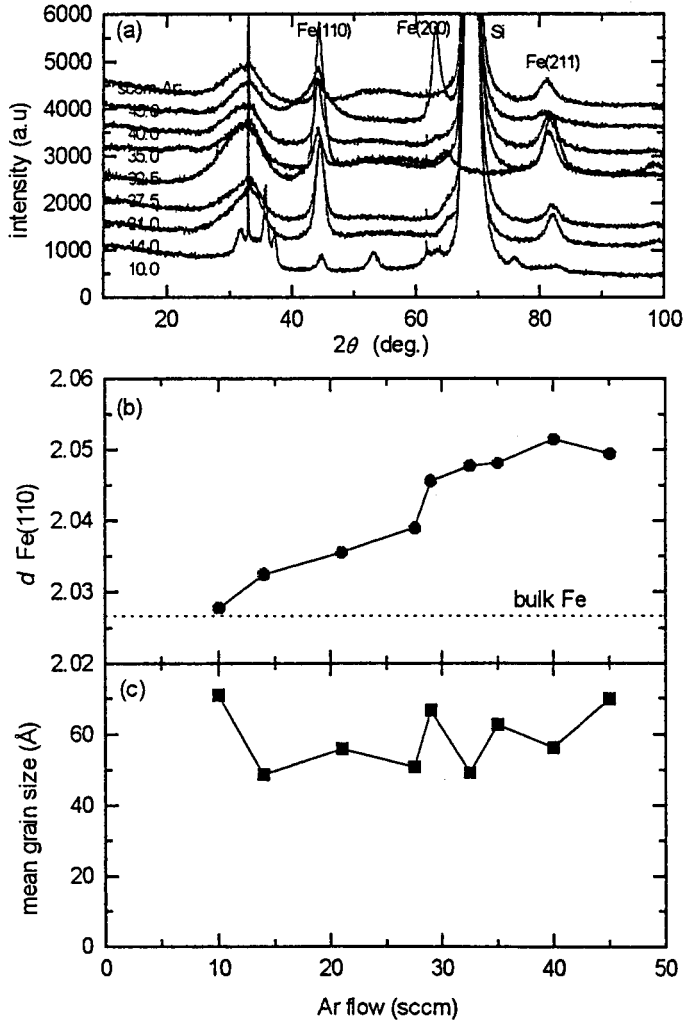

Fig. 5.2 (a). Typical XRD patterns (Cu K^{α} radiation) of FeHfO thin films for different argon flows. The large peak at near 68° is a Si peak from the substrate. It only appears for samples grown on the Si/SiO_2 substrates. The Fe (110) peak becomes more narrow for higher Ar/O_2 flows. (b) represents the (110) interplanar spacing of the α-Fe and (c) the grain size of the Fe crystallites as a function of the argon flow.

From this figure the lattice parameter increases with the Ar flow with a steep increase at about 30 sccm Ar, which is in agreement with the foregoing. It might be possible that more Hf atoms are build in at higher pressures (i.e. Ar flows), which enhances the lattice parameter. The mean grain size shows no obvious dependence on the Ar flow: it remains small i.e. between 5 and 7 nm.

As will be discussed in section 5.3, by annealing the samples, the magnetic properties change. This may be related to structural changes in the FeHfO films. Therefore, Fig. 5.3 collects the XRD patterns of samples (group 3 in table VII) annealed at various temperatures. The lattice parameter and grain size are included also; Fig 5.3 (b) and (c), respectively.

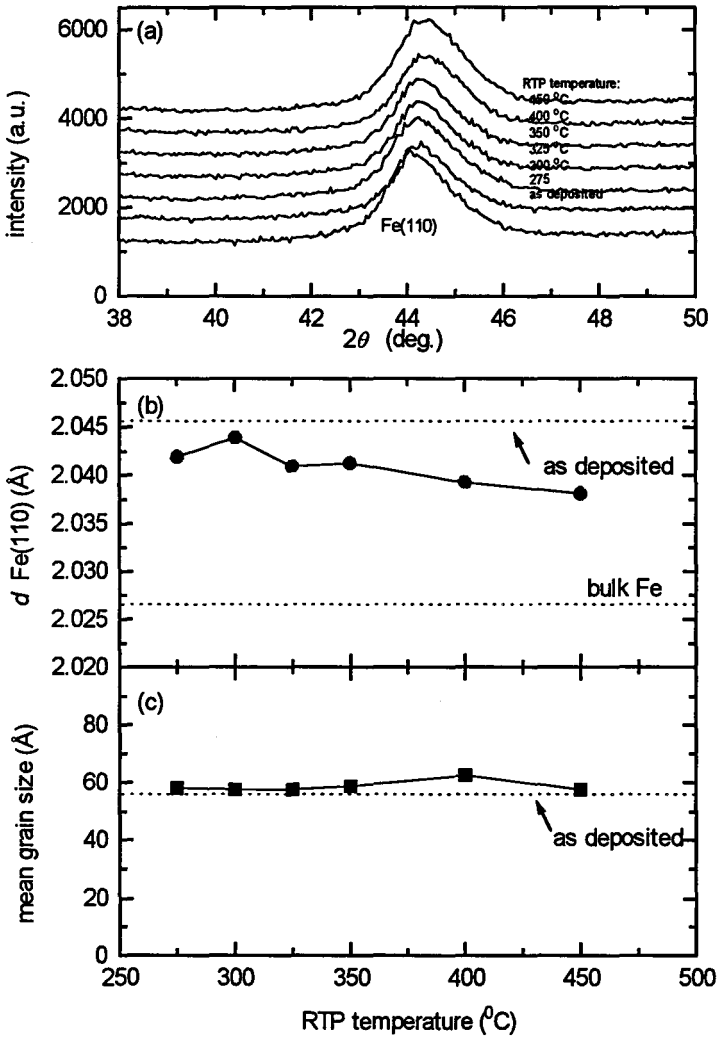

Fig. 5.3 XRD intensity pattern of the Fe (110) peak in FeHfO thin films annealed at different temperatures shown together with an as deposited sample (a). In this case the throttle valve is completely opened. In (b) the Fe(110) interplanar spacing and (c) the grain size of the Fe crystallites are shown as a function of the annealing temperature.

The lattice parameter is larger than expected from the lattice constant of α-Fe for all annealing temperatures including the as deposited state. As mentioned, this is probably caused by Hf atoms dissolved in the bcc Fe crystallites. By annealing, dissolved atoms leave the Fe nanocrystals accounting for the observed decrease in lattice parameter. It was expected that the grain size would increase with the RTP temperature, because annealing tends to promote crystallisation. However, this does not appear from the XRD patterns. The crystallite size does not change. Apparently, the amorphous FeHfO phase has a high thermal stability and inhibits the growth of the Fe-crystallites.

For reasons to be discussed in section 5.4, we also investigated films prepared from a target with additions of copper (Cu) or silicon (Si). The XRD pattern of an FeHfSiO thin films are not shown in figure 5.4: we mention that no notable differences are observed for the XRD patterns when compared to the just discussed features. The films are polycrystalline with random texture. Therefore, only the lattice parameter and the grain size are shown for different argon/oxygen flows.

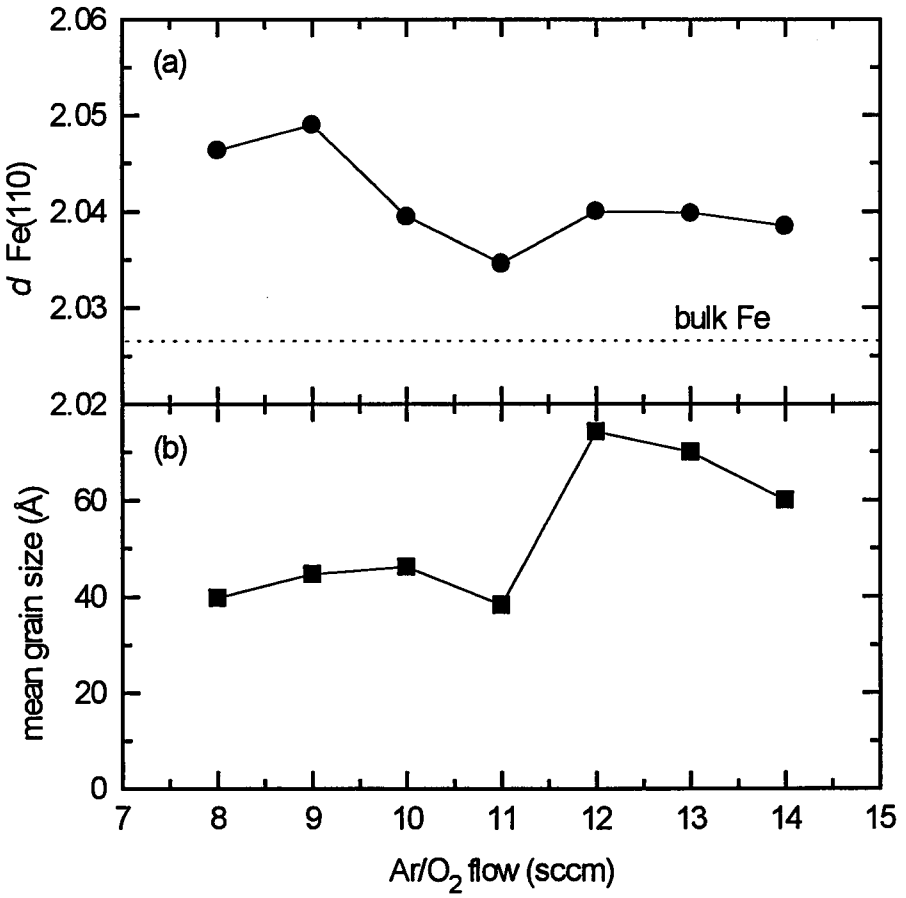

Fig. 5.4 (a) represents the (110) interplanar spacing of the α-Fe and (b) the grain size of the Fe crystallites as a function of the argon/oxygen flow as observed for FeHfSiO thin films.

The behaviour of crystallites sizes displaying the remarkable rapid change at low Ar/O_2 flows is again observed. The behaviour of the lattice parameter, on the contrary does not resemble the behaviour as observed for pure FeHfO films. Figure 5.5 represents the same crystal properties as a function of the Ar flow.

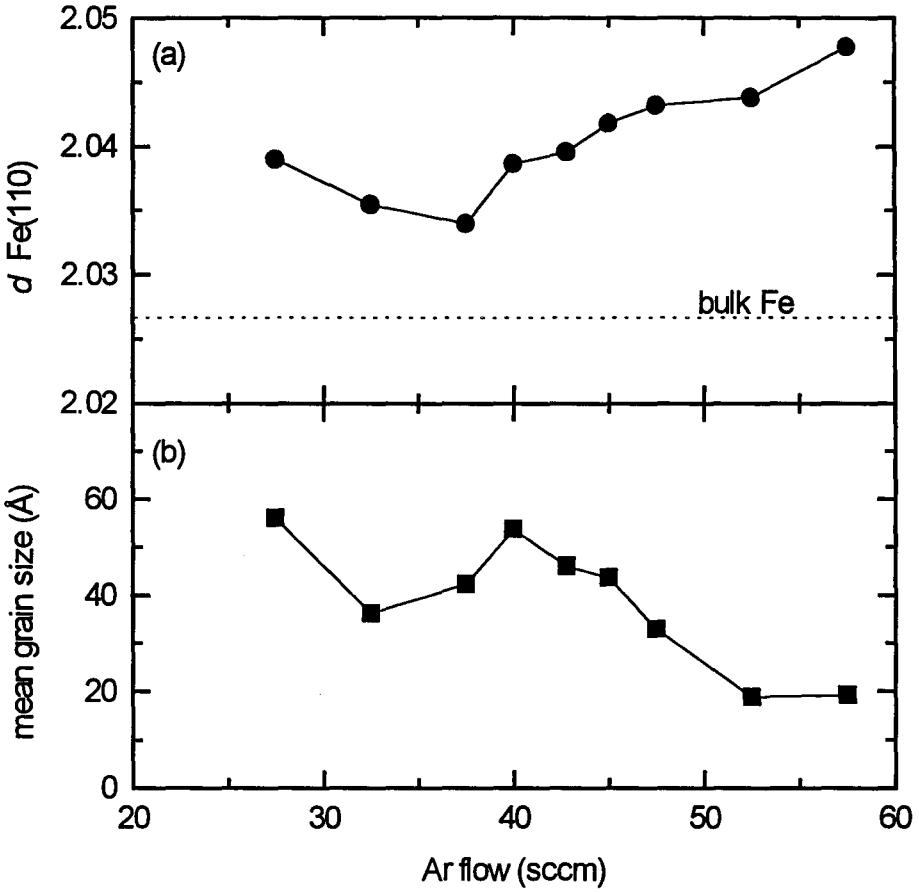

Fig. 5.5 (a) represents the (110) interplanar spacing of the α-Fe and (b) the grain size of the Fe crystallites as a function of the argon flow as observed for FeHfSiO thin films.

The lattice parameter again shows a certain steep increase (at 37.5 sccm Ar), although less pronounced as in case of FeHfO films. At flows higher than 37.5 sccm, the lattice parameter increases, while at flows beneath 37.5 sccm the lattice parameter decreases as a function of Ar flow. The grain size seems to have a local maximum as function of the Ar flow.

Roughly, we can summarize the results as follows:

- the films are poly crystalline,
- the crystallite size is typically 2-7 nm,
- a small Ar/O_2 flow or a large Ar flow seems to correspond to smaller crystallites,

- the Fe lattice parameter is larger than of bulk Fe probably due to Hf in the Fe,
- the grain size does not depend on the annealing temperature up to 450 °C,
- with annealing the lattice parameter decreases.

5.2 Magnetic and electrical properties of FeHfO thin films

To see the difference between an as deposited FeHfO thin film and a film annealed in the presence of a magnetic field, several magnetization loops are given for a typical soft-magnetic 0.7 μm thick FeHfO film in figure 5.6. In all cases, the applied field is directed along the long axis of the sample. Also the relative magnetic permeability μ' at a frequency of 100 kHz is given in this picture. This permeability is measured in all cases with the rf field parallel to the long axis of the sample.

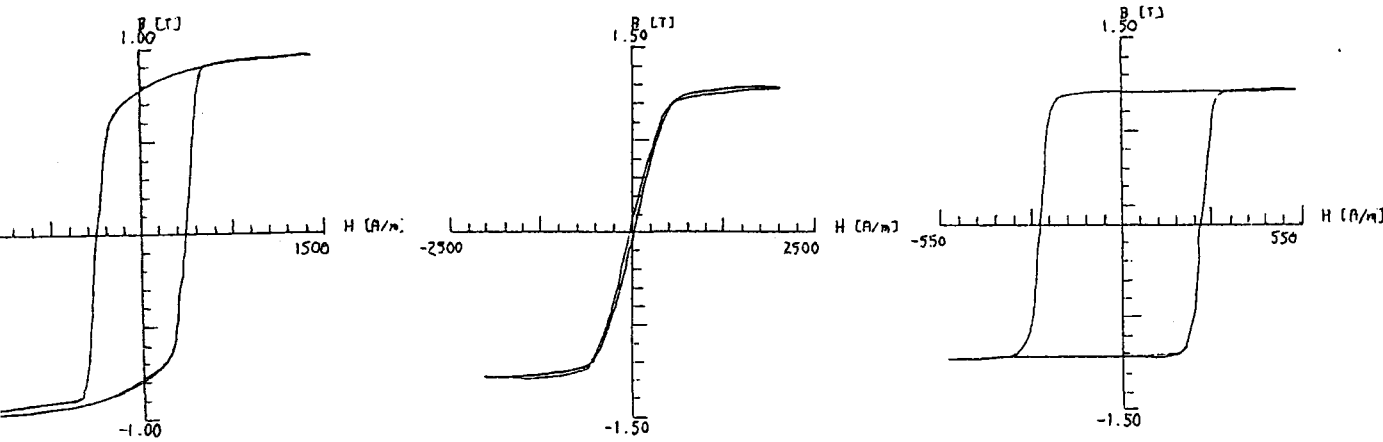

Fig. 5.6 BH loops for a 0.7 μm thick FeHfO thin film measured with the field applied along the long axis of the sample. The magnetization is depicted for an as deposited film (a), for a film annealed in a magnetic field of 48 kA/m along the short axis of the film, representing the hard axis magnetization curve (b) and for a film annealed in a magnetic field along the long axis of the film, representing the easy axis magnetization curve (c).

From this figure it is obvious that annealing in a magnetic field changes the situation dramatically. An as deposited FeHfO shows a low permeability μ'(100 kHz)=283 with a relatively large coercive field H_c of 370 A/m (Fig. 5.6(a)) and a large remanence. The domains for this film are expected to be orientated randomly, and no over all preferential direction is present. But there are domains which are orientated with their local *easy* axis parallel to the measurement direction, some with their local *hard* axis parallel to the measurement direction and some others have components parallel and perpendicular to the measurement direction. This implies that the BH loop is an averaged magnetization curve.

After annealing at 400 °C in a magnetic field along the short axis of the strip, a field induced uniaxial anisotropy is expected to be introduced. As Fig. 5.6(b) shows this indeed occurs and results in a linear B(H) curve typical for a hard axis loop. This situation corresponds to a high relative permeability of 1555 when measuring along the hard axis direction. When annealing along the long axis, the magnetization loop is square and the remanence induction B_r is 100%. This situation corresponds to a relatively low magnetic permeability of 52. In this case the rf field is along the easy axis and the magnetization process finds its origin in domain wall movements which as discussed in section 2.4 have a strongly reduced and thus small contribution to the permeability at higher frequencies (100 kHz). However, we note that in the present case of square loop with a remanence of 100% and with a coercivity considerably larger than the small rf field (2.5 A/m) in the permeability measurement, it is rather surprising that the permeability is still 52. It is expected to be 1, because the film is saturated at zero field, which means that there are no domain walls.

The saturation induction B_s=1.1 T is rather high. Compared to B_s=2.2 T in the case of iron this means that approximately 50% of the volume of the film contains Fe having its full magnetic moment. From RBS measurements (section 5.1, table VII) it follows that indeed circa 50% of the FeHfO thin film consists of Fe. It is rather surprising that the Fe atoms apparently exhibit their full moment. It would be expected that Fe atoms with O or Hf neighbours (e.g. in the amorphous phase) have reduced magnetic moments because of the transfer of electrons between the atoms.

Also the resistance of the FeHfO changes during annealing. The resistivity of an annealed film is lower than the resistivity of an as deposited sample. Typical values are 2000 μΩcm for the as deposited film and 1000 μΩcm for the annealed film. This may indicate some ordening process of the atoms. Considering Fig. 5.2 where the XRD patterns are shown for several temperatures, no significant change in the Fe(110) reflection peak can be observed. Therefore, the changes probably occur in the amorphous FeHfO phase rather than in the Fe crystallites. This is in agreement with the fact that the resisitivity is expected to be dominated by the high resistivity amorphous phase and not by the low resisitivity of the Fe crystallites (bulk Fe ρ=10.5 μΩcm).

Table VIII gives a summary of the most important electrical and magnetic properties of the above discussed cases.

Table VIII. Electrical properties of a typical FeHfO thin film in the as deposited state as well in the annealed state (RTP 400 °C, 5", 48kA/m). The latter situation is subdivided in the case when the magnetization is measured in the easy axis direction and the case when the magnetization is measured in the hard axis direction.

property	*as deposited*	*annealed (easy axis)*	*annealed (hard axis)*
resistivity ρ (μΩcm)	1950	1020	1034
saturation magnetization B_s (T)	1.0	1.1	1.2
coercive field H_c (A/m)	370	250	29
magnetostriction coefficient λ_s	$5 \cdot 10^{-6}$	$5 \cdot 10^{-6}$	$5 \cdot 10^{-6}$
uniaxial anisotropy K_u (J/m^3)	-	-	310
permeability μ'(100 kHz)	283	52	1555
magnetization process occurs by:	domain wall movements + rotation of magnetization	domain wall movements	rotation of magnetization

5.3 Sputtering parameters and annealing conditions

To investigate the electrical and magnetic properties of the FeHfO thin films as function of several sputtering and annealing conditions, a number of experiments were performed. Three main parameters which are varied, are the argon flow, the oxygen flow and the annealing temperature.

Firstly, the results of the variable argon flow on the electrical and magnetic properties of the films measured with the techniques described in chapters 2 and 3, are presented in figure 5.7.

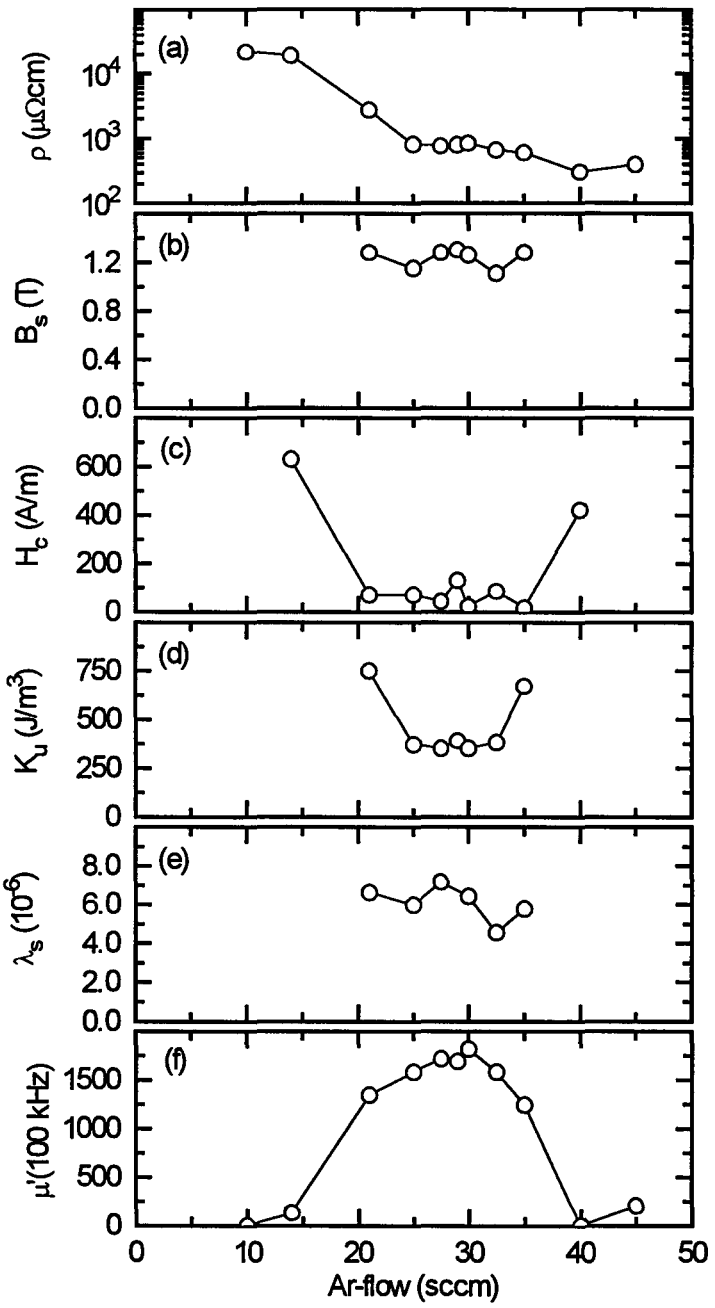

Fig 5.7 Electrical and magnetic properties of 0.7μm FeHfO thin films RF-sputtered on SiO_2 substrates in an Ar/O_2 plasma at various argon flows. The resistivity ρ (a), the saturation induction B_s (b), the coercive field H_c (c), uniaxial anisotropy constant K (d), magnetostriction λ_s (e) and permeability μ at 100 kHz (f) were measured at room temperature after rapid thermal annealing treatment at 400 °C for 5 seconds in a static field of 48 kA/m.

From this figure it becomes clear that in the interval between 20 sccm and 35 sccm argon, reasonable soft magnetic behaviour of the film is observed: The relative permeability μ' at 100 kHz (Fig. 5.7(f)) is always above 1200 with an optimum of 1800 at 30 sccm argon. Beneath 20 sccm argon and above 35 sccm argon the permeability decreases rapidly as function of the Ar flow. The uniaxial anisotropy (Fig. 5.7(d)) decreases when the permeability increases, in agreement with Eq. (2.10) which states that the permeability is inversely proportional to the uniaxial anisotropy. If one applies Eq. (2.10) on the K_u data to calculate μ in fact a quantitatively satisfactorily agreement is obtained with the data in Fig 5.7(f). Considering the coercive field (Fig. 5.7(c)) we conclude that the coercive field is lower than 150 A/m with a minimum of 23 A/m at 30 sccm. For very low or very high argon flows the coercivity increases enormously. This suggests that a large permeability is connected with a low coercivity and vice versa, which is in agreement with the fact that the coercivity is proportionally related to the uniaxial anisotropy, while the permeability is inversely proportional to the uniaxial anisotropy (Fig. (5.7(d)). The resistivity (Fig 5.7(a)) of these films seem to remain constant, except for very low argon flows where the resistivity is much larger and for very high argon flows where it is lower (note the logaritmic scale for ρ). More Ar implies relatively less O_2 in the plasma. We measured the magnetization loop showin paramagnetic behaviour, implying a decrease of the permeability. This has also been observed in Fe-rich FeZr [31], where the amorphous phase would exist of two magnetic states: one state is strongly ferromagnetic similar to α-Fe, while the other phase is antiferromagnetic. This can be seen as the limit of our FeHfO system for very low oxygen contents. In case of relative much oxygen the amorphous intergranular phase becomes non-magnetic, which means that the exchange interaction cannot do its averaging work: the Fe-crystallites are decoupled, see section 2.5. This is also in agreement with the large resistivity at low Ar flows: more oxygen implicates a larger resistivity.

Because of a low coercivity, a high permeability and a reasonable saturation induction of 1.1 T (Fig. 5.7(b)) are achieved, the investigated FeHfO thin films can be regarded as good soft magnetic. Apart from this, a high electrical resistivity of 850 μΩcm (Fig 5.7(a)) seems to make this material interesting for applications. One difficulty that makes these films not suitable for magnetic heads is the high saturation magnetostriction λ_s of $5 \cdot 10^{-6}$ (Fig 5.7(e)) which is too large for this application: one needs typically values below $5 \cdot 10^{-7}$.

A second parameter that might influence the structure and the electrical or magnetic properties of the FeHfO thin films is the amount of oxygen in the film. This effect has been studied by changing the Ar/O_2 flow leaving the Ar flow constant at a rate of 30 sccm. Sputtering with different Ar/O_2 flows, again yields an optimum in the soft-magnetic properties, see Fig. 5.8.

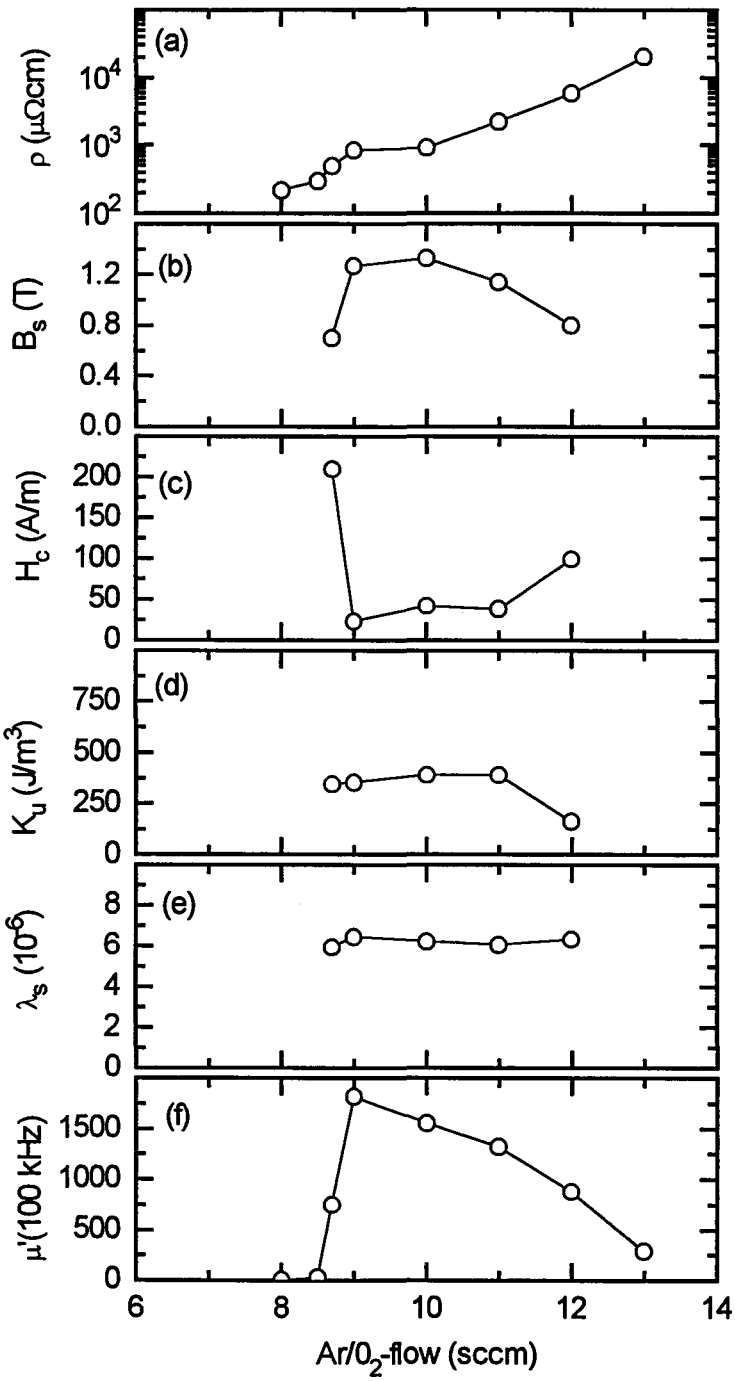

Fig. 5.8 Electrical and magnetic properties of 0.7μm FeHfO thin films RF-sputtered on SiO_2 substrates in an Ar/O_2 plasma at various argon/oxygen flows. The resistivity ρ (a), the saturation induction B_s (b), the coercive field H_c (c), uniaxial anisotropy constant K_u (d), magnetostriction λ_s (e) and permeability μ at 100 kHz (f) were measured at room temperature after rapid thermal annealing treatment at 400 °C for 5 seconds in a static field of 48 kA/m.

A possible explanation for the behaviour as a function of the amount of oxygen, has been discussed basically already in the foregoing. If the amorphous phase contains a lot of oxygen, it will not be magnetic. This implies that no coupling between the crystallites can take place. This is the reason why the permeabiltiy is reduced enormously for large Ar/O_2 flows. For very low oxygen concentrations in the plasma the permeability decreases rapidly. This steep decrease can also be discerned in the XRD data from Fig 5.1. Also a possible explanation is given there for this behaviour. Also the behaviour of the resisitivity is clear: the more oxygen is used in the sputter deposition, the more oxygen is build in the amorphous phase. This implies a higher resistivity.

The third and last parameter to be discussed here is the annealing temperature. Again, the influence on the electrical and magnetic properties has been investigated. Some FeHfO samples were sputtered with a 42.8 sccm Ar flow and a 12 sccm Ar/O_2 flow[1]. Afterwards, they were RTP annealed at various temperatures during 5 seconds in a field of 48 kA/m. Figure 5.9 gives some properties of the films as a function of annealing temperature for FeHfO thin films deposited on glass and Si/SiO_2 substrates.

It is striking that some magnetic properties such as permeability and coercivity are not very sensitive to different annealing temperatures. Good soft magnetic properties can be achieved in a wide temperature range (300°C-500°C). The resistivity, on the other hand, decreases considerably with the temperature. As discussed in section 5.2 this is probably related to changes in the amorphous phase and not due to the crystallization of Fe, see also the XRD data in figure 5.3(c), which show that the crystallite size is rather independent with the annealing temperature. The fact that no further crystallization occurs with temperature is in agreement with the behaviour of the magnetostriction:

$$\lambda_s = v_{cr}\lambda_s^{\alpha\text{-}Fe} + (1 - v_{cr})\lambda_s^{amorphous}. \qquad (5.1)$$

Here, v_{cr} is the volume fraction of the crystallites and $\lambda_s^{\alpha\text{-}Fe} = -4 \cdot 10^{-6}$ and $\lambda_s^{amorphous} \approx 10^{-4}$ a 10^{-5} are the magnetostrictions of the crystalline and the amorphous phase respectively. The experiments showed that λ_s is positive for FeHfO. This implies that the total magnetostriction is dominated by the positive magnetostriction of the amorphous phase. The total magnetostriction λ_s is rather independent of anneal temperature suggesting that indeed v_{cr} does not change as supported by the XRD data. It is remarkable that there are also some differences for glass and Si/SiO_2 substrates. The BH loops of the samples which are submitted to the annealing experiments are shown in figure 5.10.

[1]These Ar and Ar/O_2 flows cannot be compared to those in Fig. 5.7 and 5.8. This is because for the annealing experiments, the films were prepared with a different setting of the throttle valve. This will be discussed in the next section.

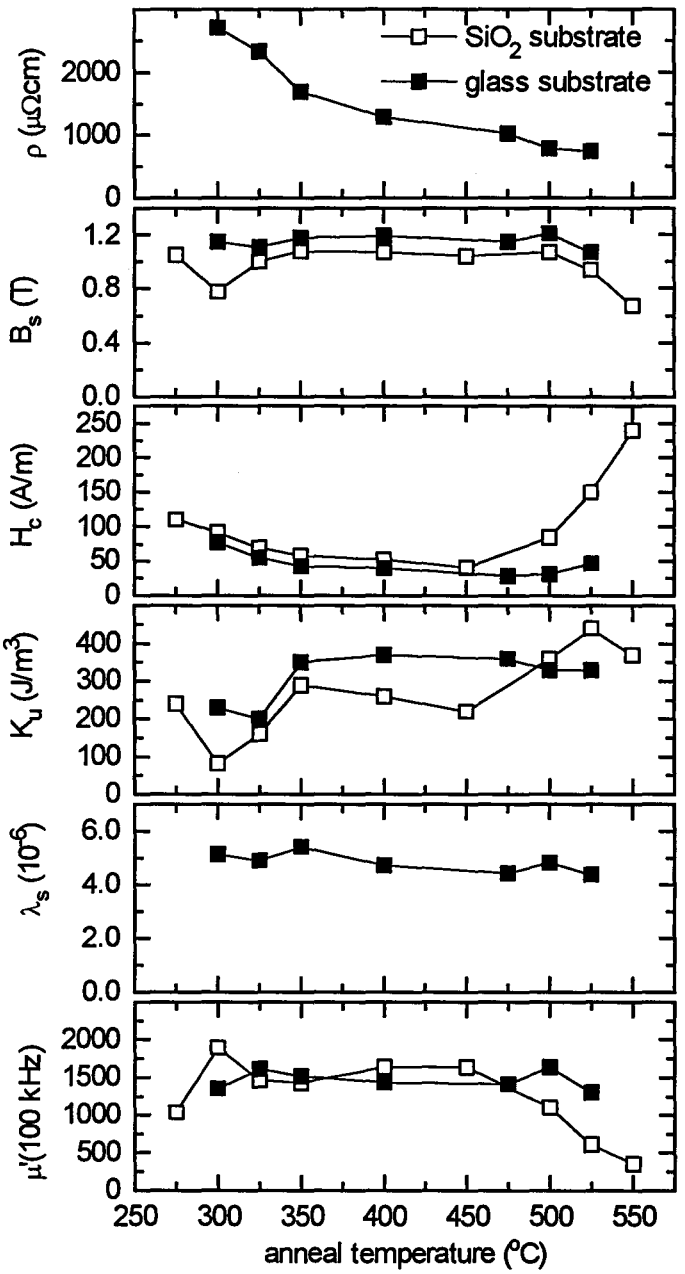

Fig 5.9 Electrical and magnetic properties of 2.1 μm FeHfO thin films RF-sputtered in an Ar/O_2 plasma with an argon flow of 42.8 sccm and an Ar/O_2 flow of 12 sccm (throttle valve opened completely) on SiO_2 and glass substrates. The resistivity ρ (a), the saturation induction B_s (b), the coercive field H_c (c), uniaxial anisotropy constant K (d), magnetostriction λ_s (e) and permeability μ at 100 kHz (f) were measured at room temperature after rapid thermal annealing treatment at various temperatures for 5 seconds in a static field of 48 kA/m.

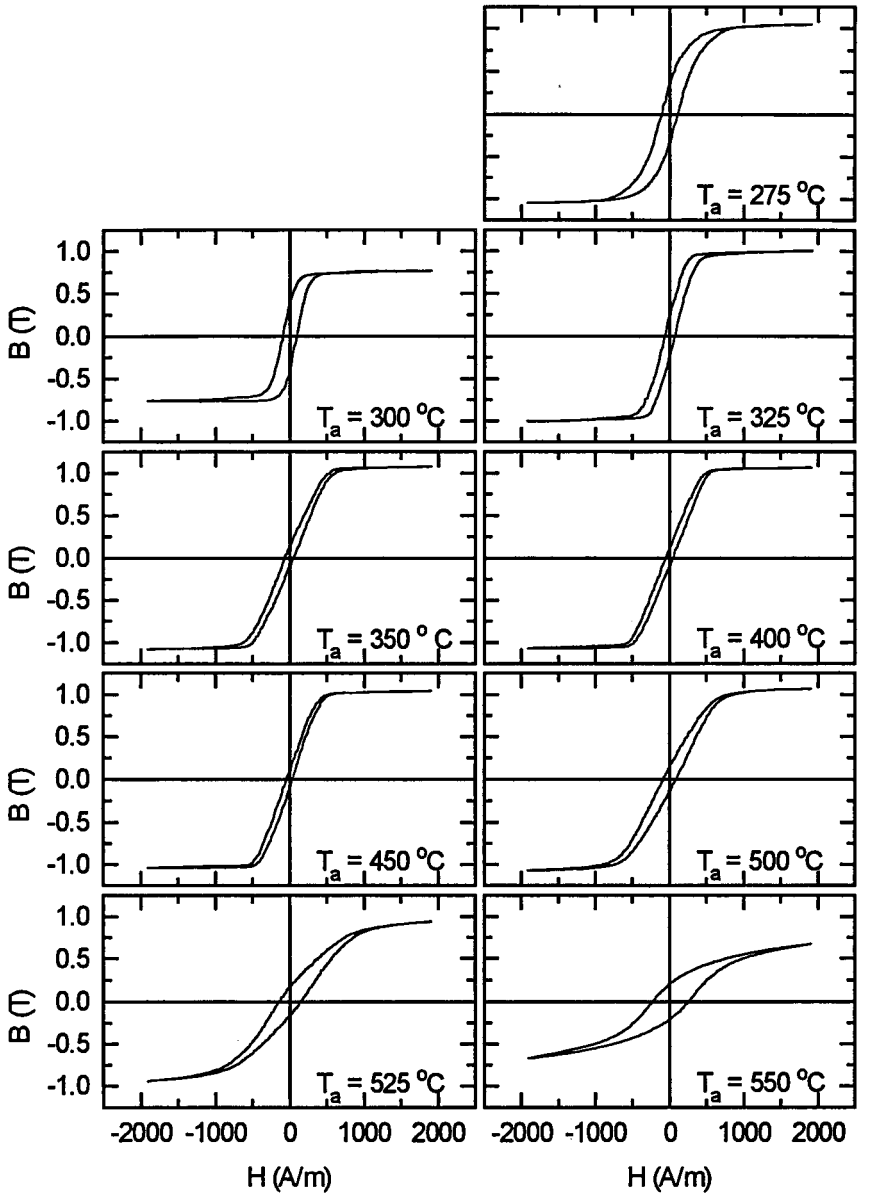

Fig. 5.10 BH loops at room temperature of a sputtered FeHfO samples on Si, RTP annealed at different temperatures.

From this figure it is immediately obvious that the FeHfO films at temperatures 350, 400 and 450 °C exhibit the desired behaviour, as distinct from the films annealed at a temperature of 525 °C, for instance. Because the magnetic properties change by annealing, it is expected that some structural changes might appear in the X-ray patterns. However, as mentioned this is not the case. The explanation therefore remains unclear. It may be related to changes in the amorphous phase since these cannot be identified by XRD.

5.4 Technological optimizing

5.4.1 Background pressure

After the former experiments it was suggested that the magnetic properties might be improved by achieving a lower background pressure in the chamber of the sputtering machine. It is possible to increase the pumping rate by enhancing the opening of the throttle valve (section 3.1). After opening the throttle valve between the turbo pump and the chamber completely, of course not only the background pressure gets lower, but also the pressure during sputtering: the Ar is pumped also more effectively. To get the same sputtering pressure, one is obliged to enhance the flows of the two gas inlets (Ar and Ar/O_2). So, the sputtering conditions where the optimum permeability was observed were adjusted from an Ar flow of 30 sccm and an Ar/O_2 flow of 9 sccm to an Ar flow of 42.8 sccm and an Ar/O_2 flow of 12.84 sccm. This was a zeroth order gess, i.e. the ratio between the two flows is taken to be the same. Because it was not excluded that this procedure is not valid, a number of samples were grown to find again the Ar/O_2 flow that maximizes the magnetic permeability. The results are presented in Fig. 5.11.

From the figure above it becomes clear that the expected optimum FeHfO thin film sample is not found at a Ar/O_2 rate of 12.84 sccm, but at a slightly lower flow of about 12 sccm. This is not so surprising when we consider the different gasses. Ar is an inert gas, while O_2 is a reactive gas which can easily be absorbed by / react with the chamber walls, the target, etc. The gas balance in the chamber may be easily determined. The supplies of O_2 gas and Ar gas to the chamber per unit time are denoted by Q_{O2} and Q_{Ar} respectively. If the pumping speed is S, then an oxygen flow equal to Q_P given by $Q_P=p_{O2}S$ will be pumped by the vacuum pump, where p_{O2} is the partial pressure of the oxygen. The flow of oxygen must be equal to the consumption by the pump and the absorption:

$$Q_{O2}=p_{O2}S+Q_{abs}. \tag{5.2}$$

The argon, on the other hand, will not be absorbed by the chamber walls, so the the pumping is in equilibruim with the supply of argon:

$$Q_{Ar}=p_{Ar}S. \tag{5.3}$$

Here, p_{Ar} is the partial pressure of Argon. Now it is clear that if the pumping speed S in Eq. (5.2) is increased by opening the throttle valve that the optimum gas flow ratio shifts to smaller Ar/O_2 flows:

$$\frac{Q_{O2}}{Q_{Ar}} = \frac{p_{O2}S+Q_{abs}}{p_{Ar}S} = \frac{p_{O2}}{p_{Ar}}+\frac{Q_{abs}}{p_{Ar}S}. \tag{5.4}$$

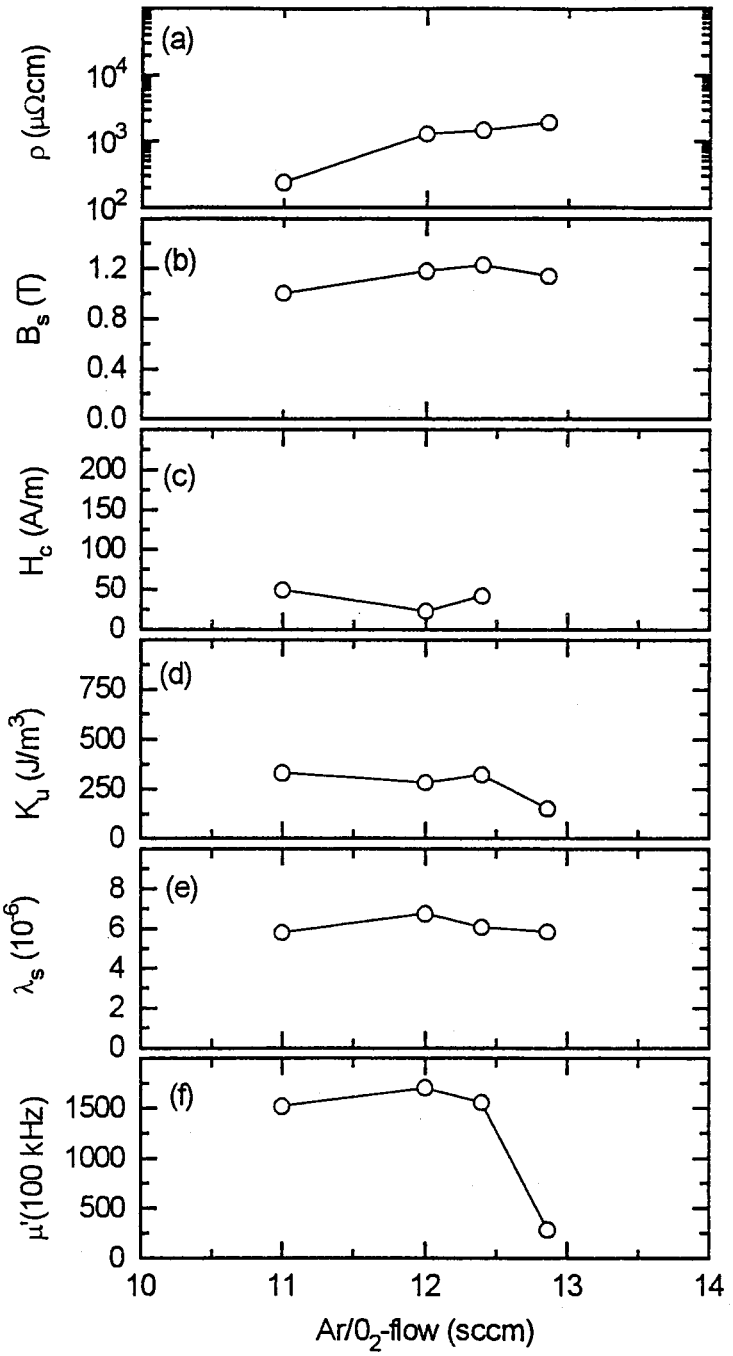

Fig. 5.11 Electrical and magnetic properties of 0.7μm FeHfO thin films RF-sputtered in an Ar/O_2 plasma at various argon/oxygen flows on SiO substrates after the throttle valve was opened completely. The resistivity ρ (a), the saturation induction B_s (b), the coercive field H_c (c), uniaxial anisotropy constant K_u (d), magnetostriction λ_s (e) and permeability μ at 100 kHz (f) were measured at room temperature after rapid thermal annealing treatment at 400 °C for 5 seconds in a static field of 48 kA/m.

5.4.2 Rotating field annealing

The magnetic permeability can be further optimised by performing rotating field annealing experiments as discussed below. Instead of using a FeHfO film which is positioned in a static magnetic field during annealing, it is also possible to rotate the film during this rapid thermal processing. Normally the annealing process takes five seconds, excluding the ramp of the annealing temperature and the decline in temperature after the treatment. Because this 5" time of constant temperature is to short to average out every direction because of limited rotation speed < 120 rpm, the present annealing experiments including rotation were carried during a somewhat longer time: 60 seconds. Because this enlargement does not influence the magnetic properties much as has been checked, there are no changes in the film to be expected from this adaptation alone. The varying parameter is the portion of the time during which the sample is rotated. For two different Ar/O_2 flows (11 and 12 sccm), the magnetic permeability is measured and presented in figure 5.12.

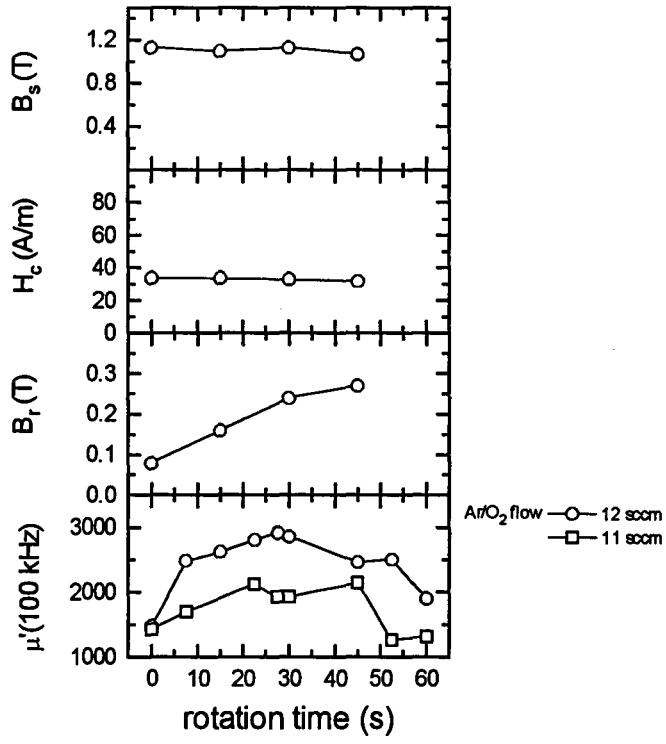

Fig. 5.12 Magnetic properties of 2.1 μm FeHfO thin films RF-sputtered in an Ar/O_2 plasma at two different argon/oxygen flows (11 and 12 sccm) on SiO_2 substrates after the throttle valve was opened completely. The saturation induction B_s (a), the coercive field H_c (b), the remanence B_r (c) and permeability μ at 100 kHz (d) were measured at room temperature after rapid thermal annealing treatment at 400 °C for 60 seconds in a field of 48 kA/m. The films were rotated for a certain part of the time of the total anneal time.

A rotation time of 0 seconds, means that the sample is annealed for 60 seconds in a static field, while 60 seconds rotating means 0 seconds annealing in a static magnetic field. Fig. 5.12 shows an increase in the permeability with the rotation time and an optimum at about 30 seconds. If the rotation time becomes even larger, the permeability appears to decline again. The ramping behaviour in the permeability can be explained by considering the uniaxial anisotropy. To obtain a high permeability, a *small* uniaxial anisotropy should be present. This implies that by increasing the rotation time and connected with this, a diminishing period in which the annealing treatment takes place in a static magnetic field, the uniaxial anisotropy is expected to decrease and the permeability which is inversely proportional to this anisotropy would increase. This is because during the rotational part of the annealing process, no uniaxial anisotropy is induced in one single preferential direction. Actually, the anisotropy is averaged out. However, this would imply that the permeability would increase through the entire time interval i.e. until the sample is rotated during the whole process time. This is not the case. The declining part may be related to the enlargement of the remanence B_r, which causes a smaller permeability. When the complete process is done without a period of static annealing, no uniaxial field induced anisotropy will remain so randomly orientated domains will determine the magnetization process. It is remarkable that the permeability is rather high for the sample which has been rotated during the whole annealing process of 60 seconds. It is expected that no uniaxial anisotropy is induced in a certain direction.

5.4.3 Addition of Cu and Si

From the considerations made in section 5.2. it became clear that the magnetic properties are good enough for the use in high frequency magnetic head, with the exception of a far too high saturation magnetostriction. As mentioned before, it is necessary that this parameter is as small as possible ($<5\cdot10^{-7}$) in combination with small internal stresses to reduce the magnetostrictive anisotropy. The lowest values reached in the experiments ($5\cdot10^{-6}$) are still about 50 times larger than desirable. Addition of other elements like Cu or Si might be helpful to diminish λ_s.

Firstly, the addition of Cu was investigated. Part of the area of the 15 cm diameter $Fe_{83.3}Hf_{16.7}$ target that has been used up till now, was covered with square shaped pieces of copper. By covering 0.5 % of the target area, the average composition of the target will be $Fe_{82.9}Hf_{16.6}Cu_{0.5}$. The motivation to use Cu to diminish the magnetostriction, is the assumption that Cu may promote nucleation of α-crystallites, see the discussion around Eq. (5.1). The magnetostriction of the Fe crystallites λ_c is small and negative ($-4\cdot10^{-6}$) compared to the magnetostriction of the amorphous phase λ_a which is large and positive (10^{-5}). Therefore it is expected that the addition of Cu would contribute to a lower total magnetostriction, because the volume fraction of Fe would increase. Figure 5.13 summarizes the electrical and magnetic properties of the FeHfCuO thin films.

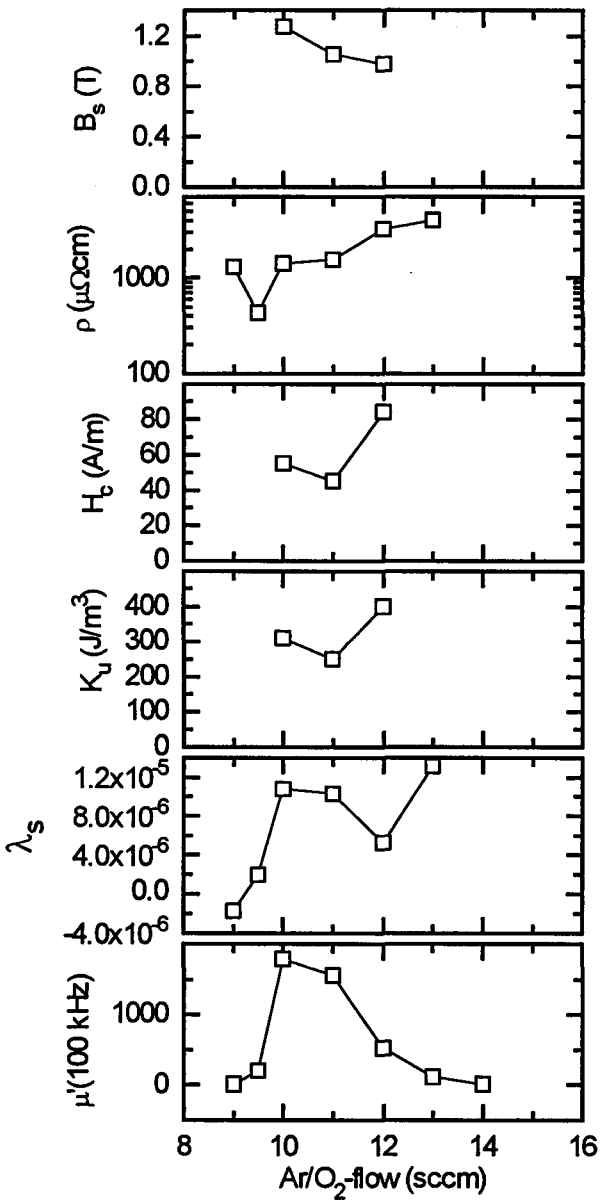

Fig. 5.13 Electrical and magnetic properties of 2.1 μm FeHfCuO thin films RF-sputtered in an Ar/O_2 plasma at various argon/oxygen flows on glass substrates after the throttle valve was opened completely. The resistivity (a), the saturation induction (b), the coercive field (c), uniaxial anisotropy constant (d), magnetostriction (e) and permeability at 100 kHz (f) were measured at room temperature after rapid thermal annealing treatment (at 400 °C for 5 seconds in a static field of 48 kA/m). The FeHf target area was covered for about 0.5% with Cu pieces.

Comparing these results with those displayed in Fig 5.8 and 5.11, it appears that the resulting permeabilities (Fig.5.13f) of the FeHfCuO are similar to those of FeHfO. The saturation magnetostriction λ_s did not reduce. This appeared in agreement with the XRD data. The crystallites size did not increase in size nor did their number: the ratio between the height of the Fe(110) peak and amorphous bumb was about the same. The addition of Cu increases the magnetostriction constant (Fig.5.13e). The resistances increase with the oxygen flow and are similar in magnitude to those of pure FeHfO. It is remarkable that the optimum is shifted slightly to a lower Ar/O_2 flow of 10 sccm instead of 11 sccm. We have no explanation for this shift.

It was suggested that Si could promote nucleation of α-Fe. The surface area of the FeHf target was covered with about 4% of the area with Si. Again the dependence of the electrical and magnetic properties was investigated, see Fig. 5.14.

The permeability shows a similar dependence on the Ar/O_2 flow. The magnetostriction is similar to that of FeHfO. It is obvious that the addition of elements such as Cu and Si do not diminish λ_s. The Ar dependence is also considered for the FeHfSiO thin films. These results are depicted in Fig. 5.15.

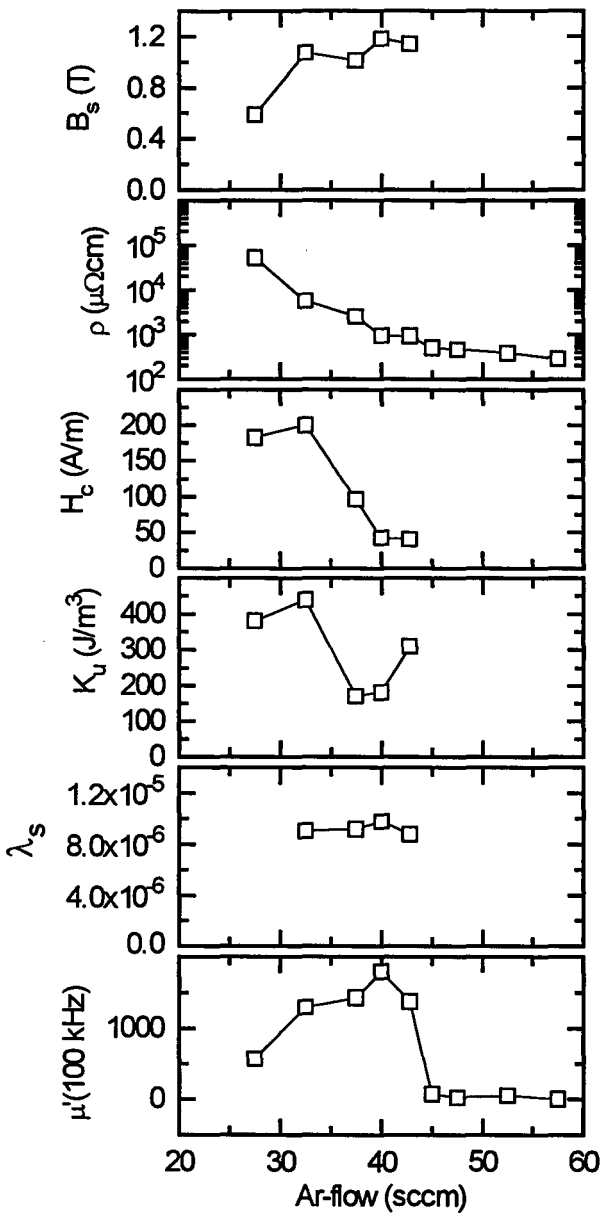

Fig. 5.14 Electrical and magnetic properties of 2.1μm FeHfSiO thin films RF-sputtered in an Ar/O_2 plasma at various argon flows on glass substrates after the throttle valve was opened completely. The resistivity ρ (a), the saturation induction B_s (b), the coercive field H_c (c), uniaxial anisotropy constant K_u (d), magnetostriction λ_s (e) and permeability μ at 100 kHz (f) were measured at room temperature after rapid thermal annealing treatment (at 400 °C for 5 seconds in a static field of 48 kA/m). The FeHf target was covered for about 4% with Si pieces.

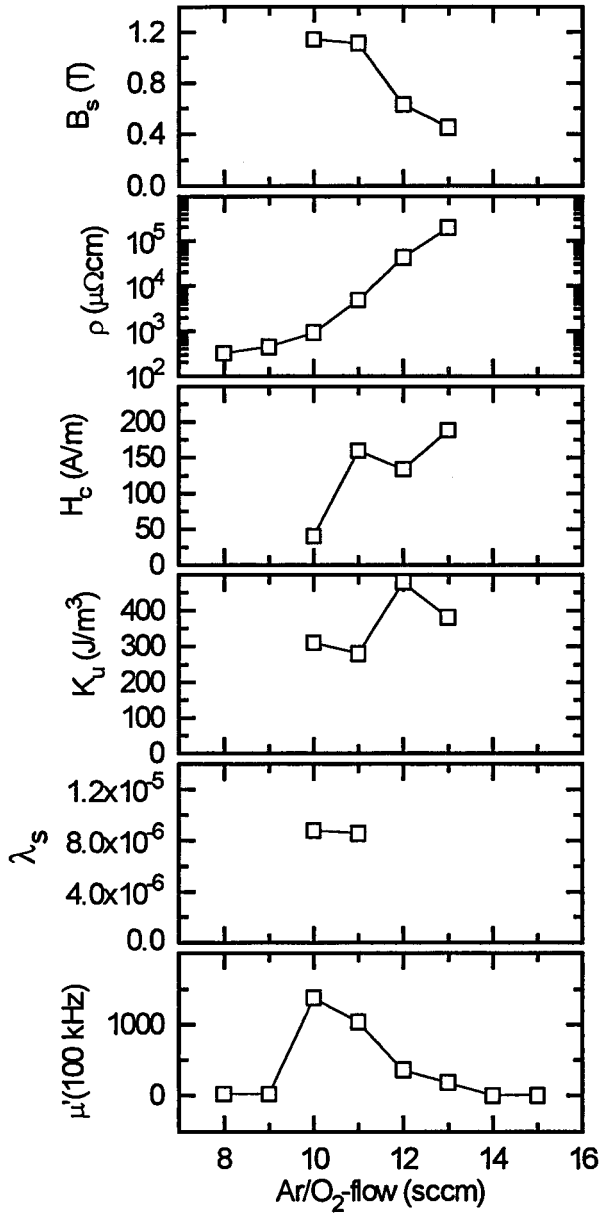

Fig. 5.15 Electrical and magnetic properties of 2.1μm FeHfSiO thin films RF-sputtered in an Ar/O_2 plasma at various argon/oxygen flows on glass substrates after the throttle valve was opened completely. The resistivity (a), the saturation induction (b), the coercive field (c), uniaxial anisotropy constant (d), magnetostriction (e) and permeability at 100 kHz (f) were measured at room temperature after rapid thermal annealing treatment (at 400 °C for 5 seconds in a static field of 0.6 kOe). The FeHf target was covered for about 4% with Si pieces.

5.4.4 Application as separation oxide

Up till now it has been shown that despite attempts to reduce the magnetostriction constant to an acceptable level has not been succeeded. It has not been possible to make FeHfO suitable for the application as a flux guide material in for example magnetic heads. However, FeHfO films with a large resistivity and still a reasonable magnetic permeability may be interesting for the application as a separation oxide. Here we will discuss this item briefly.

In Fig. 5.15 a schematic overview of a conventional yoke-type magnetoresistive head (YMRH) is depicted.

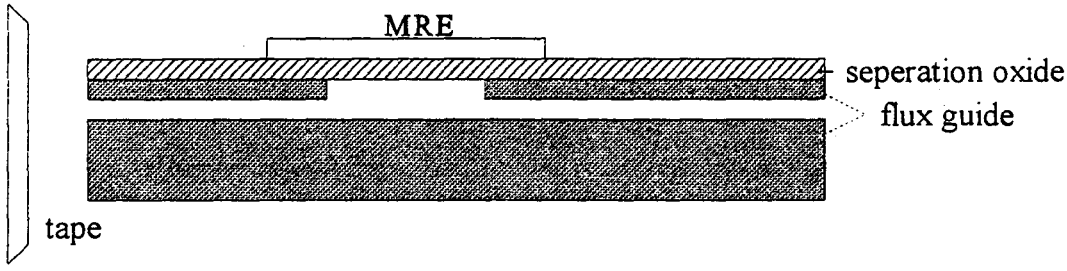

Fig. 5.16 Schematic overview of a Yoke-type magnetoresisitive head. The MRE represents the magnetoresistance element seperated from the fluxguide by a seperation oxide.

When the magnetic head is in operation, the flux guide material will guide part of the magnetic flux that originates from the tape towards a magneto resistive element (MRE), which serves as the magnetic sensor. The flux has to traverse the seperation oxide which serves as insulator. Ideally one would like as a separation layer a soft magnetic unsulating or at least high resistive layer. So far, no material has been identified that exhibits these properties and that can prepared also in thin film form at temperatures that are compatible with the currently used temperatures in head processing. Considering Fig. 5.15 FeHfSiO films may be a first candidate. As can be seen, films with a resistivity neat the required one with a magnetic permeability of 200 can be prepared. Therefore, according to calculations presented in v.d. Zaag *et al.* [32] these films offer the oppertunity to increase the efficiency of the heads considerably, viz. by a factor 5 to 6.

5.5 Frequency dependent permeability measurements

With the help of the HF permeability set-up, extensively discussed in chapter 3, it is possible to investigate the behaviour of the magnetic permeability as a function of frequeny up to 200 MHz. Especially, the role of eddy currents and ferromagnetic resonance can be considered in this frequency range. Because wall permeability is only dominant at low frequencies, the LF permeability is more usefull to investigate this mechanism.

For FeHfO thin films, the frequency dependent complex permeabilities were measured for films of several thicknesses. The results are shown in figure 5.17 The squares and circles represent the experimental data μ' and μ" repectively. The meaning of the solid lines will be discussed later on.

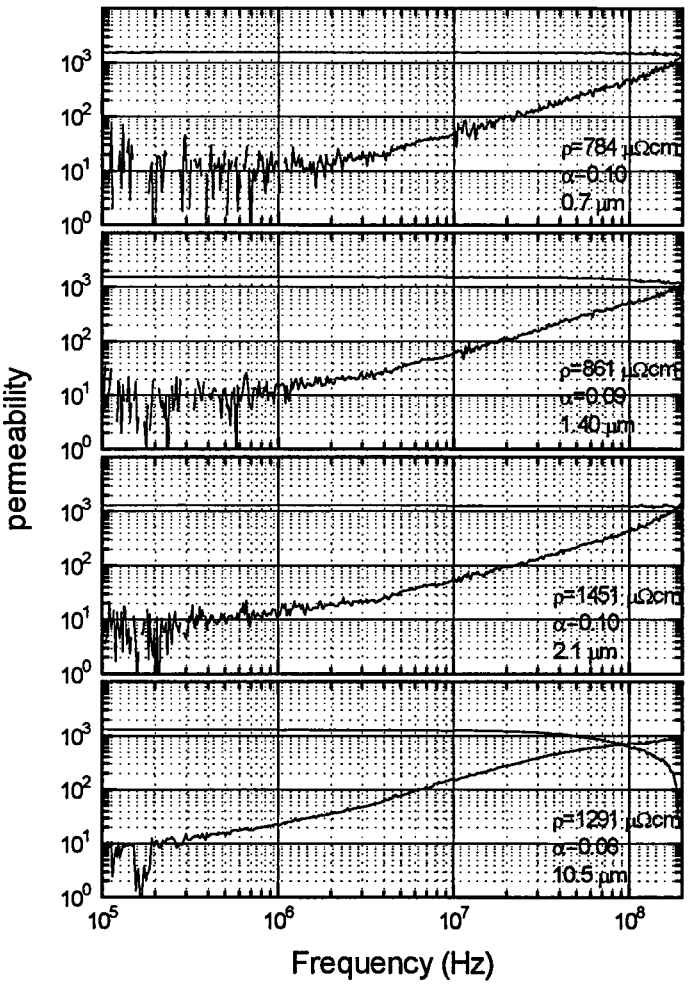

Fig. 5.17 Frequency dependence of the magnetic permeability for FeHfO thin films of different thicknesses as indicated. The solid lines are model calculations taking eddy currents effects as well as ferromagnetic resonance effects into account. The used damping parameters α and resistivities ρ are indicated also.

It is seen that the low frequency real part of the permeability is independent of thickness within the presently investigated thickness range, i.e. the uniaxial magnetic anisotropy is thickness independent. It also appears from this figure that the cross frequency f_{cross} which is the frequency where μ' equals μ'', decreases merely slightly with increasing thickness. As discussed in chapter 2 the losses measured by the magnitude μ'', might be due to the screening of the magnetic field inside the film due to eddy currents, which become increasingly important for thicker films. As we have seen, for the eddy current mechanism, the cross frequency varies inversely proportional with t^2 as described by Eq.(2.29). This implies that by enlarging the film thickness by a factor 10 for instance, and leaving all other properties (ρ and μ) constant, the cross frequency should decrease with a factor 100 if the frequency dependent behaviour of the permeability is determined by the eddy current mechanism. Considering figure 5.17, this does not seem to be the case: the cross frequencies hardly change with increasing thickness except for the 10.5 μm thick film where a small reduction in f_{cross} is observed. This is more clear from Fig. 5.18 where the cross frequency is plotted as a function of thickness (solid squares). In this figure also the expected behaviour bases on the eddy current mechanism is plotted (Eq. (2.25)): the solid line that linear decreases with slope -2 (note the logaritmic scale for the thickness). For this calculation we have taken K_u=321 J/m^3, ρ=1000 μΩcm and B_s=1.1 T. The other lines will be explained later on.

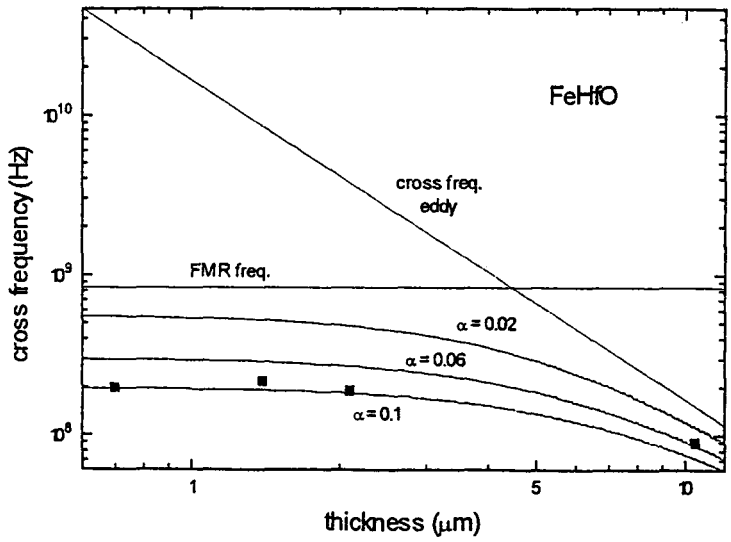

Fig. 5.18. The cross frequency as a function of film thickness. The experiment is shown with solid squares. The calculated FMR frequency (horizantal line), the eddy current behaviour (descending line) and the combination for FMR together with eddy currents is plotted.

Aparantly, eddy currents are not the limiting factor for μ in this thicknesses regime. The cross frequency that is expected from eddy current effect is much higher than the experimental cross frequency.

It is possible that the assumptions to derive the eddy current mechanism is too simple. It is derived for a thin film with uniform properties. In granular films like FeHfO the situation is more complicated: it might be possible that capacative coupling of the crystallites may result in local eddy currents within the film, which would give rise to thickness independent roll-off of the permeability. The Fe crystallites in the amorphous phase can be represented by an equivalent circuit consisting of a resistance of an Fe crytallite in series with the impedance of the amorphous phase. The latter can be regarded as a large resistance and in parallel with this a capacitor. Using such an equivalent circuit it is shown in [33] that the frequency at which this capacity effect might play a role is about 10^{14} Hz, which is much higher than typical measured cross frequencies. Moreover, if these capacitance effects would be important they should find their expression in the frequency dependent electrical impedance. The real part of the impedance Re(Z) should decrease with frequency because of the short-circuit by means of the capacity. To verify if the resisitivity is indeed independent of frequency, the complex impedance of a typical FeHfO thin film is measured and presented in Fig. 5.19.

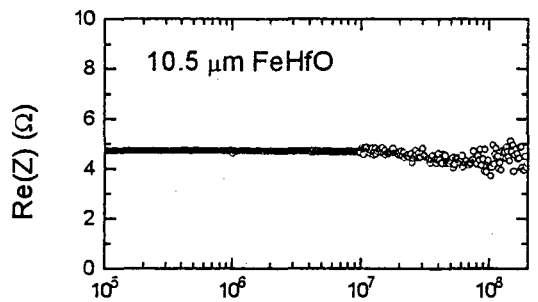

Fig. 5.19. Frequency dependence of the complex impedance of a 10.5 μm thick film.

The real part of the electrical impedance Re(Z) seems to be independent of freqency up to 200 MHz. Thus, we have shown that capacitive behaviour in the granular structure cannot account for the fact that the experimental cross frequency is much lower than expected and calculated from a model of (local) eddy currents.

Another candidate that might explain the experimental results of the frequency dependent permeability is ferromagnetic resonance (FMR). The horizontal line at 0.836 GHz represents the FMR frequency in the geometry of the permeability measurements (Fig.2.14) as determined by Eq. (2.32). The used parameters are γ=185 GHz/T and K_{eff}=300 J/m^3. This FMR resonance frequency is higher than the cross-frequency. Evidently, a certain line width determined by the damping factor α is necessary to account for the roll-off. To calculate the combined effect of

eddy currents shielding and FMR, the solution for the complex magnetic permeability caused by ferromagnetic resonanced (Eq. (2.31)) is substituted in the expression for the eddy currents (eq. (2.25)). The cross frequency was determined numerically. The curved functions in Fig. 5.18 represent the combined eddy current and Landau-Lifshitz problem for different damping factors α. The best fits are found for α between 0.06 and 0.10, and give an acceptable description of the observations.

By electron spin resonance (ESR) experiments at the Eindhoven University of Technology, we have tried to determine this damping parameter independently. The geometry of the measurement has been depicted earlier in Fig. 2.15, i.e. a variable DC magnetic field H is applied in the direction parallel to the length of the sample and a small AC microwave field $h(t)$ is applied in plane perpendicular to this direction. The field H was swept through the resonance. The used equipment was a commercial Bruker spectrometer employing a standard rectangular TE102 X-band cavity for room temperature measurements with a klystron frequency of 9.34 GHz. In figure 5.20 the field derivative of the absorbed power of a typical 0.7 μm FeHfO film is shown.

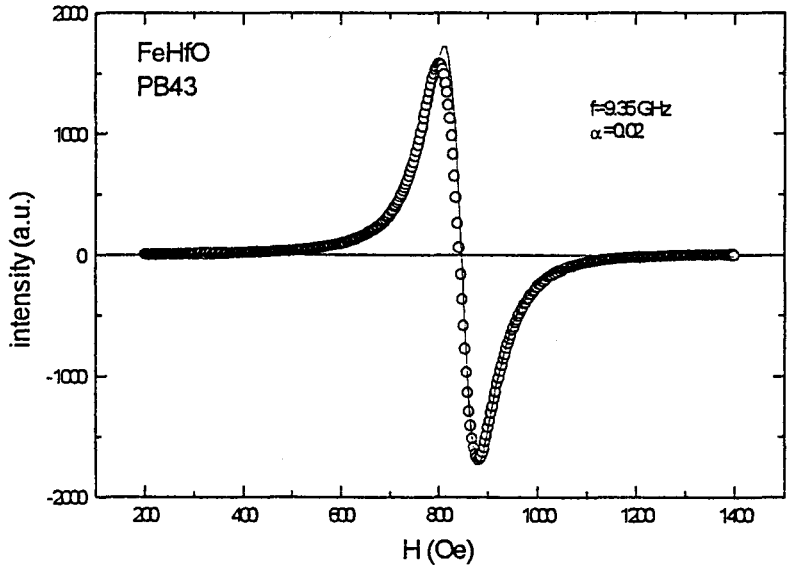

Fig. 5.20 Derivative with respect to the magnetic field of the absorbed power as a function of this field of a 0.7 μm FeHfO film. The magnetic field was directed along the film plane.

In this figure also the best fit based on Eq. (2.34) in combination with eddy currents is shown, yielding a damping factor of α=0.02. This is clearly not in good agreement with the permeability measurements, resulting in a damping factor α between 0.06 and 0.10. This discrepancy is not yet clarified: it is likely that the determination of α based on the model, where the Landau-Lifshitz equation and the Maxwell equations are decoupled then solved seperately and then combined again is too simple.

Up till now we have only fixed on one single point: the cross frequency. To infer if the permeability behaviour in the full frequency range between 100 kHz and 200 Mhz can be described by combining eddy currents and FMR we have performed some calculations. The solid lines in Fig. 5.17 represent these calculations. The values for the resistivity ρ and the damping parameter α used for the respective calculations are indicated. Here, the damping factors α were chosen such that the experimental cross frequencies were in agreement with the calculated cross frequency. The resistivity was not a fitted value but a value obtained from an independent resistance measurement. As can be seen from this figure it is possible to calculate a reasonable fit for the experiments within the whole regime.

In the frequency range below 3 MHz the calculations for μ" start to deviate considerably from the experimental data. The magnitude of the deviation increases with decreasing frequency. The losses in this regime are ascribed to wall movements as discussed in section 2.4. We investigated this behaviour more accurately by means of the LF permeability set-up, as will be discussed below.

For the 10.5 μm film we measured the permeability as a function of the frequency by making use of the LF set-up. The open square symbols in Fig. 5.21 represent this experiment. The other lines in this picture will be discussed below.

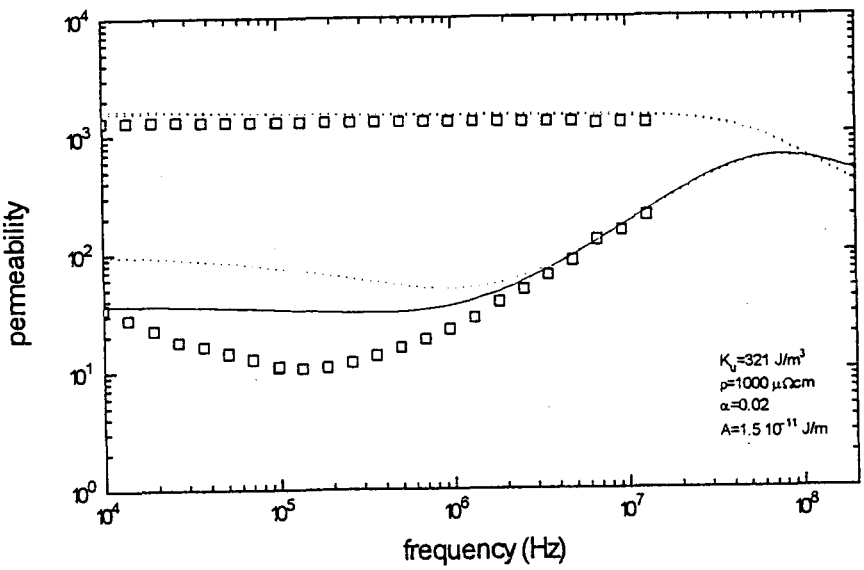

Fig. 5.21 Frequency dependence of the magnetic permeability for 10.5 μm FeHfO thin film in the low frequency range.

If the behaviour of the imaginart part of the permeability μ" would be caused by eddy currents and FMR the low frequency behaviour would be a straigth line as discussed before. As discussed in section 2.5 the decrease in μ" is caused by the domain wall movements, see Eq. (2.37). The wall permeabilty in the present case is determined by the walls of the closure domains, see Fig.2.7(c), because these walls only can lead to magnetization in this case (the walls with their plane perpendicular to the field will not move). It is possible to calculate the

domain size D_w (Fig.2.10) as discussed in appendix D. In this appendix also some expressions are given for the mobility m and the damping factor β. The parameter α, now representing the restoring coefficient of the wall as in Eq. (2.36), was chosen to be zero. All the used and calculated parameters are presented in this figure. A denotes the exchange constant. The dotted line in Fig. 5.21 shows the calculated behaviour of the permeability which is a combination of rotational permeability and the just mentioned wall permeability. For both mechanisms the permeability is frequency dependent, related to eddy currents and FMR. The calculations and the experimental data are in reasonable agreement. It must be noted that *no* fit parameters are used in the calculations. A possible explanation for the deviation between experiment might be the size of the domains D_w which is calculated to be 0.22 mm. In this calculation we assumed a macroscopic anisotropy constant. By stresses near the edges of the film the magnetostriction can cause some magneto-elastic anisotropy. This can lead to a different domain sizes. To check this, a potograph was madethe domains near the edges of the film were imaged by the Bitter method. Fig.5.22 shows the result.

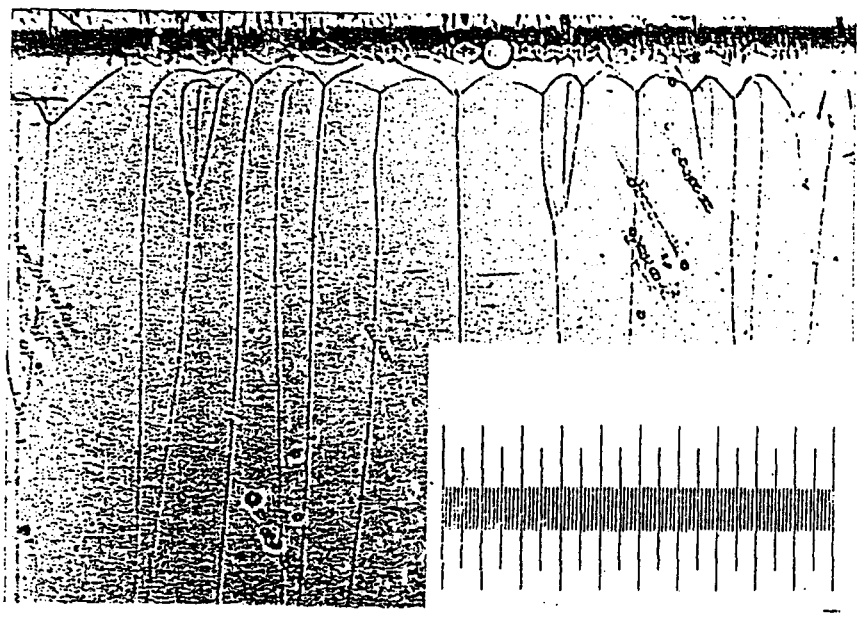

Fig. 5.22 Photograph of the domains and domain walls of a 10.5 μm FeHfO thin film near the edges of the thin film.

The observed domain size seems to be 0.079 mm which is about 3 times smaller than calculated. We used this value as input parameter and calculated again the frequency behaviour of the permeability leaving all other parameters constant. This calculation is shown in Fig. 5.21 with a solid line. As expected, this adjustment has no consequences for the permeability at large frequencies. However, the losses in the permeability μ" decreases. This improves the calculation with respect to the experiment even more. Although the calculated behaviour is not exactly the same as the experimental permeability, it is surprising that within the simple model of appendix D the behaviour can be described rather well. This is because we know that some of the proposed assumptions are not correct: the domain patterns as can be seen in the photograph do not correspond with those of the theory.

5.6 Magnetorestance and tunneling

In this section we present the main results concerning magnetoresistance and tunneling phenomena in FeHfO thin films. As already mentioned in section 2.4 the FeHfO films that exhibit GMR, contain more oxygen in the amorphous phase than the films that show good soft magnetic behaviour. The different regions are indicated in the phase diagram of Fig. 5.23.

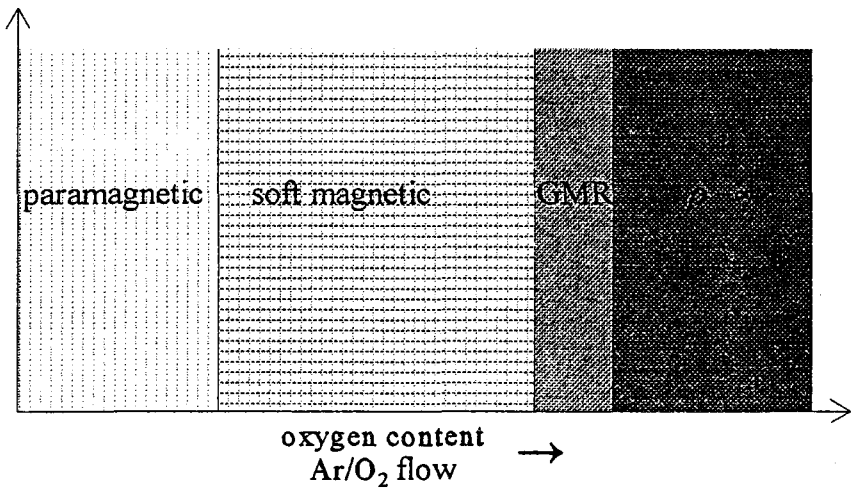

Fig. 5.23 Phase diagram of FeHfO thin films.

As can be seen from this figure, by enlarging the Ar/O_2 flow the FeHfO films change from a paramagnetic behaviour to good soft (ferro)magnetic behaviour. For larger oxygen contents the FeHfO films appear to exhibit GMR at the expence of good soft magnetic properties. The resisitivity increases as a function of the oxygen content and at very large Ar/O_2 flows the films become insulating. The transition between the paramagnetic and ferromagnetic phases and the transition between the soft magnetic and the GMR-phase are gradually as distinct from the sharp border between the GMR-phase and the insulating phase. The colour of the samples changes dramatically from deep blue to transperant red probably due to the formation of Fe_2O_3.

We measured the MR ratio at T=300 K of a FeHfO sample sputtered with an Ar/O_2 flow of 12 sccm, see Fig. 5.24 $Fe_{50.2}Hf_{10.7}O_{39.1}$

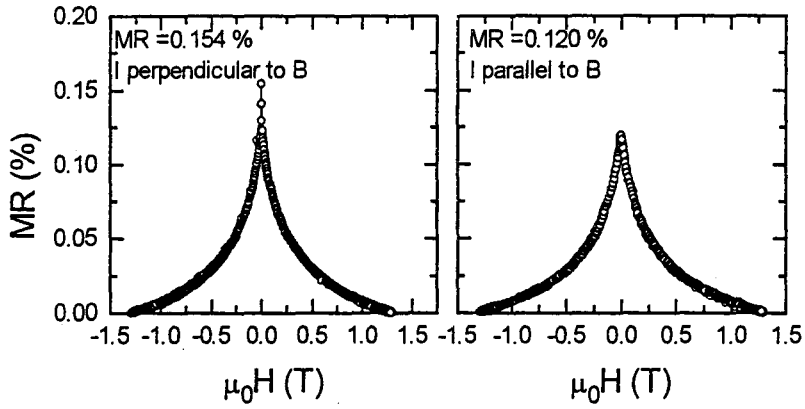

Fig. 5.24 MR ratio of $Fe_{50.2}Hf_{10.7}O_{39.1}$ thin film sputtered with a 12 sccm Ar/O_2 flow in the parallel and perpendicular configuration measured in the high field regime.

film exhibits a MR ratio of 0.15% when the magnetic field is applied parallel to the current direction, while the MR ratio in the perendicular configeration is 0.12%. The shape of the curves are comparable and shows no dependence on the direction of the applied field with respect to the current direction in the plane. However, when we zoom in field near H=0, we see the differences between the measurement in the parallel configuration and the measurements in the perpendicular configuration: the AMR contribution disappears by changing the field direction, see Fig. 5.25.

By varying the Ar/O_2 flow, the properties of the FeHfO with respect to the MR ratio changes. This is illustrated in Fig. 5.26(a).

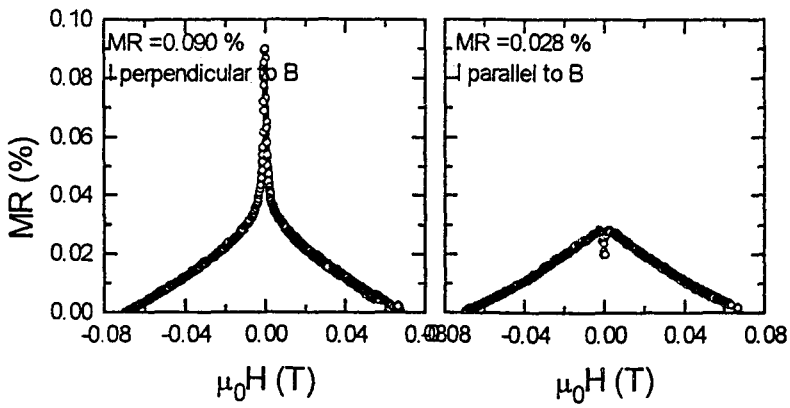

Fig. 5.25 MR ratio of $Fe_{50.2}Hf_{10.7}O_{39.1}$ thin film sputtered with a 12 sccm Ar/O_2 flow in the parallel and perpendicular configuration measured in the low field regime.

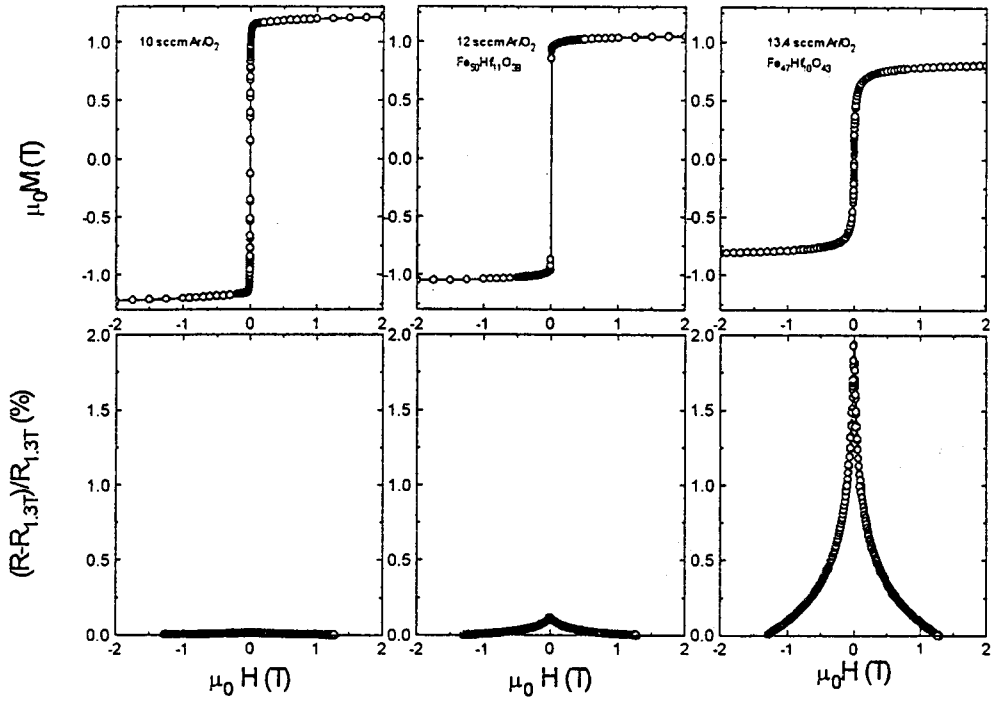

Fig. 5.26 (a) MR ratio of three different FeHfO thin film sputtered with three different Ar/O_2 flows as indicated. The magnetic field is applied perpendicular to the current and the MR is measured in the high field regime. The concentrations of the elements Fe, Hf and O are also represented in the picture. (b) Magnetization loops for the same FeHfO films.

It appears that the not only the MR ratio increases by raising the oxygen concentration in the sputter clock during but also the resistivity. By performing SQUID measurements the magnetization loops of the above discussed films were measured. These are depicted in Fig. 5.26(b). The magnetization process changes dramatically by increasing the oxygen concentration in the FeHfO alloys. The magnetization changes from a square shaped loop for an Ar/O_2 flow of 12 sccm to a more curved loop at a flow rate of 13.4 sccm. It is believed that the film becomes more amorphous at large O-concentrations. The Fe crystallites are more separated by the amorphous FeHfO phase. The MR ratio of 2% is the largest measured at room temperature for this FeHfO system. By increasing the oxygen concentrarion the films change their structure: they become brown/red and transperant, which could be due to the formation of Fe_2O_3.

The curved magnetization is due to rotation of the nano-sized Fe crystallites. If this GMR is caused by tunneling the resistivity should exhibit an exponentional behaviour with the temperature as described by Eq. (2.44). The resisitivity is measured as a function of temperature in the temperature regime between 10 K and 300 K for the three films, see Fig. 5.27.

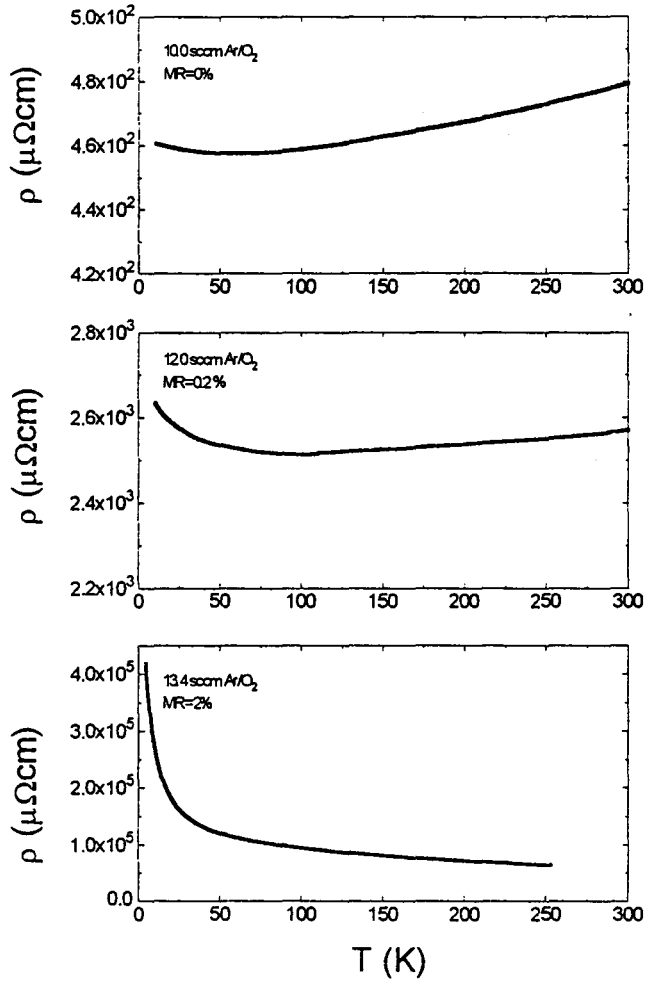

Fig. 5.27 Temperature dependent resistivity of three different FeHfO films.

Regarding Fig. 5.26 and Fig. 5.27 it is clear that not only the resistivity increases but also gets a different character for the different films as a function of temperature. For high temperatures the resisitivity of the films grown with Ar/O_2 flows of 10.0 sccm and 12.0 sccm respectively increases with temperature: this suggests a metallic conduction behaviour. The Fe crystallites form a percollating conduction path. On the contrary, the FeHfO film sputtered with a flow of 13.4 sccm Ar/O_2 shows a decreasing resisitivity with temperature. Additionally, it is seen that for small temperatures gets large. This temperature dependent behaviour could be indicative for tunneling. If the resisitivity is plotted logaritmic as function of $1/\sqrt{T}$, the resisitivity should be a straigth line according to Eq. (2.44). As can be seen in Fig. 5.28, this is not the case: tunneling can not be the only mechanism that plays a role in the conduction. We will discuss this later on.

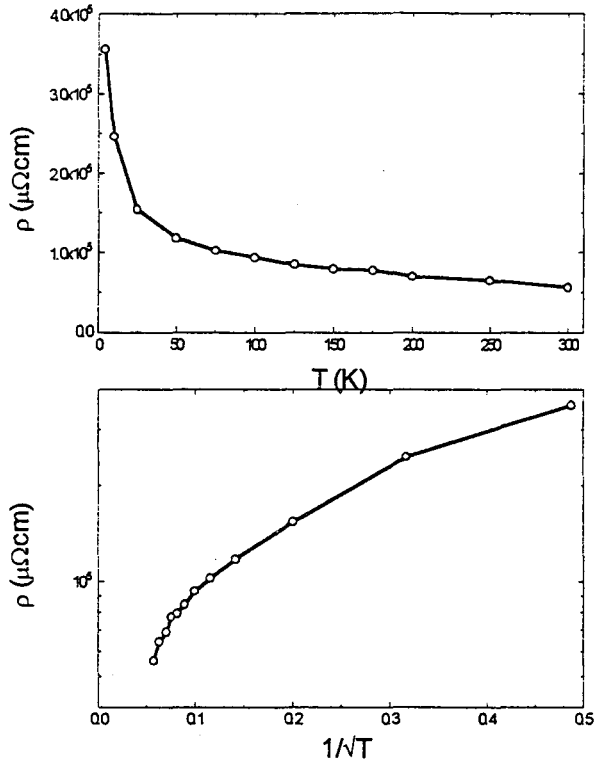

Fig. 5.28. Resisitivity of $Fe_{47}Hf_{10}O43$ thin film (13.4 sccm Ar/O_2 flow).

In Fig. 5.29 the resisitivity and the MR ratio is shown as a function of the Ar/O_2 flow during sputtering.

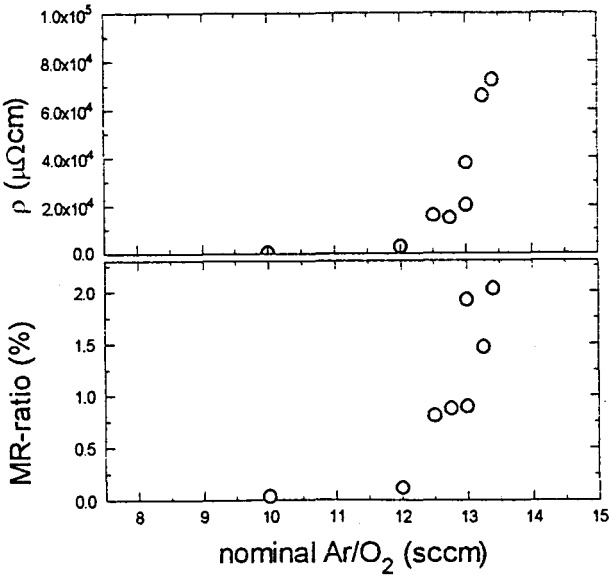

Fig. 5.29 (a) resisitivity ρ and (b) the MR-ratio for FeHfO films as a function of Ar/O_2 flow.

Both the resisitivity ρ and the MR-ratio increase rapidly above 12.0 sccm Ar/O_2. The maximum MR ratio is about 2.0% at a flow of 13.4 sccm. It is also obvious that in the regime where the MR ratio is relatively large, the soft magnetic properties of the film are bad and vice versa, see again Fig. 5.23.

As distinct from the experimental results from Fujimori *et al.*[34] the MR ratio in our FeHfO films is temperature dependent. The MR ratio as a function of temperature is shown in Fig. 5.30(b) together with the resistivity (Fig.5.30(a)). The curves will be explained below.

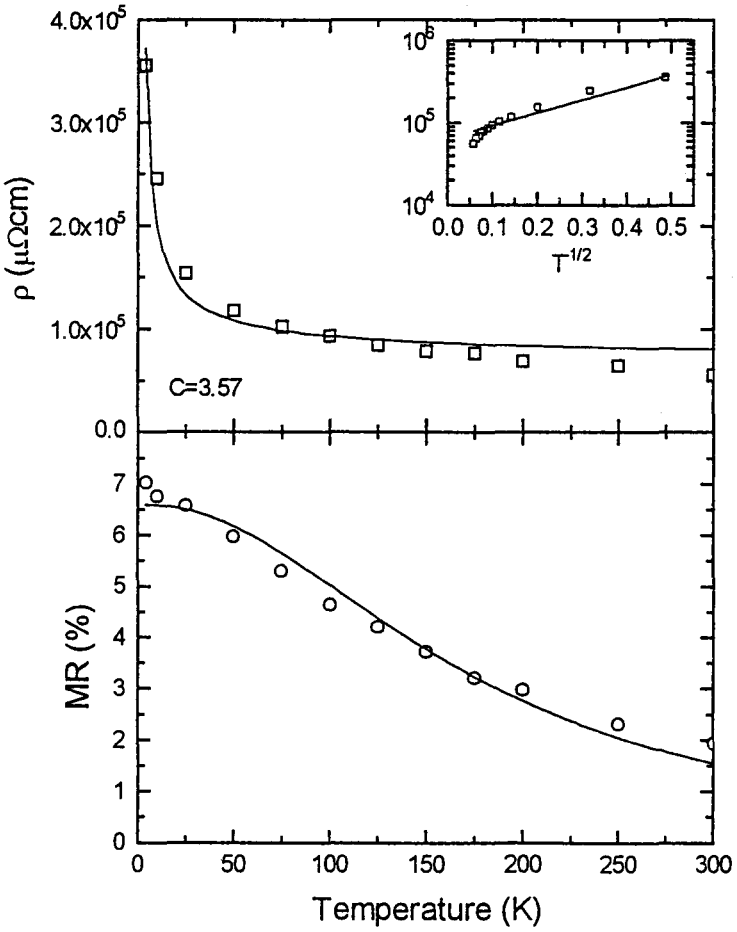

Fig. 5.30 (a) Resistivity ρ and (b) MR ratio as a function of temperature for a FeHfO film grown with a 13.4 sccm Ar/O_2 flow. The curve in (a) represents the tunneling resistivity as given by Eq. (2.44), while the curve in (b) represents the MR ratio by assuming spin-flip scattering processes. The inset in (a) shows the resistivity in a logarithmic representation.

As already discussed in chapter 2 tunneling alone can not be responsible for the temperature dependent behaviour of the MR ratio: if this would be the only mechanism the MR ratio should be independent with temperature. Spin-flip scattering processes in the amorphous phase might explain the temperature dependence behaviour of the MR ratio. By calculating the MR ratio with the resistivity now given by Eq. (2.49) which includes spin-mixing, the MR data were fitted, see the curve of Fig. 5.30(b). The input paramaters are already obtained by fitting the resistivity, see Fig. 5.30(a). The relevant fit parameters are denoted in this figure. At first the fit of the MR ratio appears to be in reasonable agreement with the experimental results. Also the calculated resisitvity seems to be a good fit, But when we consider the latter more accurately it appears that the experimental results are not a straight line in a diagram where the resistivity is plotted on a logarithmic scale as a function of $1/\sqrt{T}$, see inset Fig. 5.30(a).

To explain the deviant behaviour of the resistivity we assumed that a part of the current is able to chose a percolating path. The most simple equivalence circuit to describe this behaviour is a temperature independent resistance shunted parallel to the tunneling resistance. This schematic circuit is represented in Fig. 5.31.

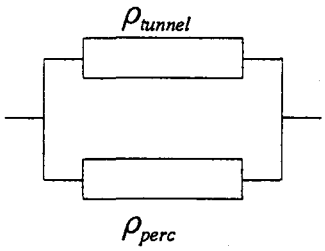

Fig. 5.31 Equivalence circuit of tunneling ρ_{tunnel} shunted parallel with a percolating path ρ_{perc}.

The resistivity is fitted again and the MR ratio is calculated and fitted again by using the fit parameters obtained from the resistivity. This is illustrated in Fig. 5.32. This figure shows that the fit that describes the experimental data of the resistivity is improved, which is rather obvious regarding the inset of Fig. 5.30(a). On the contrary, the fit that describes the data of the MR ratio is getting worse. For T=0 K the fit function even becomes zero. This also follows from the equivalence circuit of Fig. 5.31 and Eq. (2.44) describing the tunnel resistivity, which gets infinite for $T \to 0$ K. This implies that the current would flow through the magnetic field independent shunt resistance, leading to a MR ratio of 0% for very low temperatures.

Another attempt to describe the MR-ratio as a function of temperature, was by assuming a serial circuit instead of a parallel circuit. Because this did not lead to interesting results this will not be discussed here.

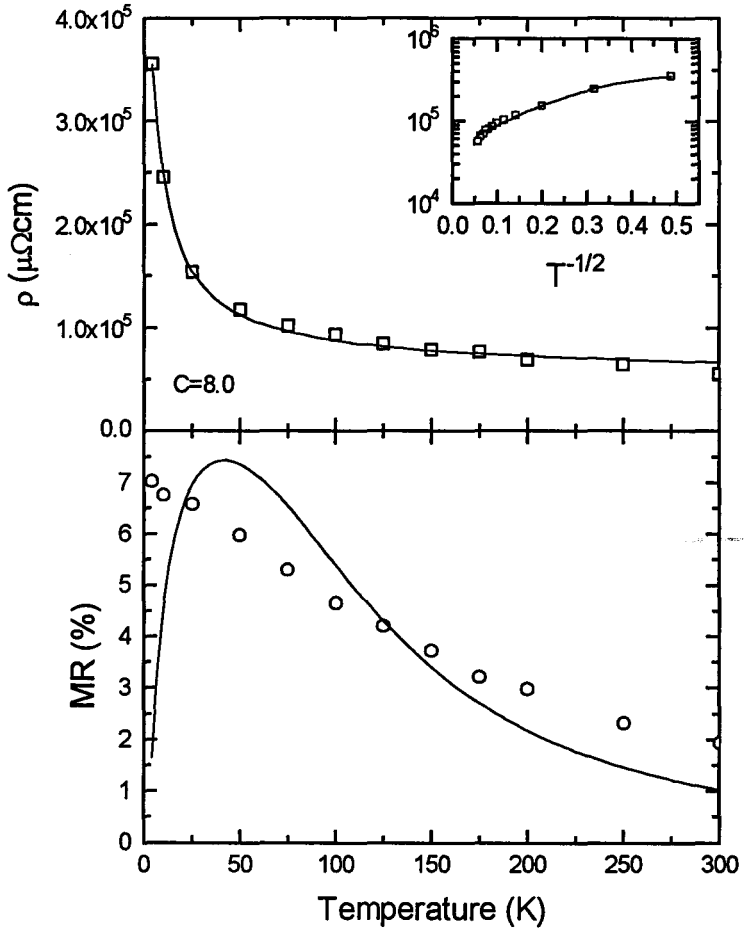

Fig. 5.32 (a) Resistivity ρ and (b) MR ratio as a function of temperature for a FeHfO film grown with a 13.4 sccm Ar/O_2 flow. The curve in (a) represents the resistivity as given by the equivalence circuit of Fig. 5.31, while the curve in (b) represents the fitted MR ratio by assuming spin-flip scattering processes. The inset in (a) shows the resistivity in a logarithmic representation.

The main conclusion concerning the temperature dependence of the MR ratio is that it can be described qualitatively by spin-flip scattering processes in the amorphous phase. The quantitative description is fairly convincing. By just assuming tunneling in combination with spin-mixing the MR ratio can be described rather accurate, in contrast with the resistivity which is not described numerically correct by the exponential behaviour of Eq. (2.44).

By calculating the MR ratio out of Eq. (2.45) or Eq.(2.49) it follows that the MR varies with $1\text{-}m^2$ at a certain temperature. This behaviour is also valid for the equavalence circuit with a resistance shunted parallel, see Fig. 5.31. This could be checked experimentally. The magnetization loop of the concerning FeHfO film was measured with a SQUID, see Fig.5.33(a). After calculating the reduced magnetization m and calculating $1\text{-}m^2$, the curve of Fig. 5.33(b) is obtained. The shape of this figure looks similar to the MR measured at 300K as a function of the magnetic field depicted in Fig. 5.33(c).

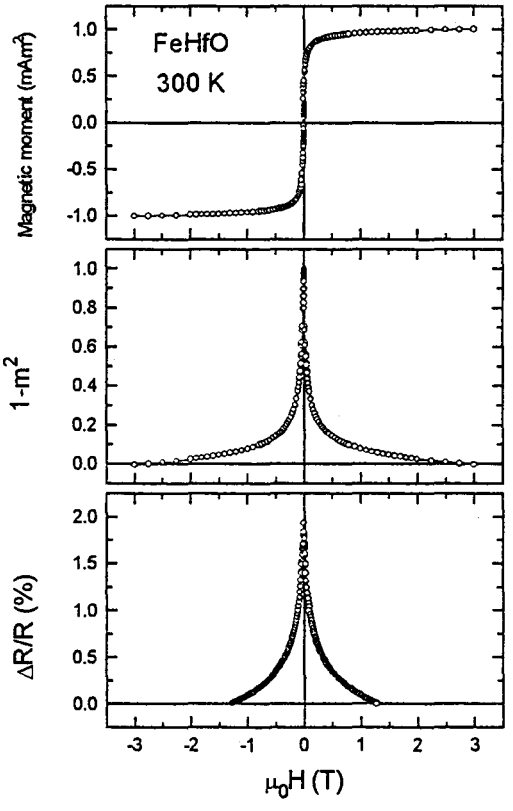

Fig.5.33 (a) The magnetization loop at 300 K of a FeHfO film measured with the SQUID. (b) Calculating curve showing $1\text{-}m^2$ where m is the reduced (c) MR as a function of the magnetic field.

When the MR curve and the curve representing $1\text{-}m^2$ is depicted in one figure it is obvious that the shapes of the curves are not completely in agreement. Fig. 5.34 gives a combined picture of the measurements performed at a temperature of 10 K and 300K.

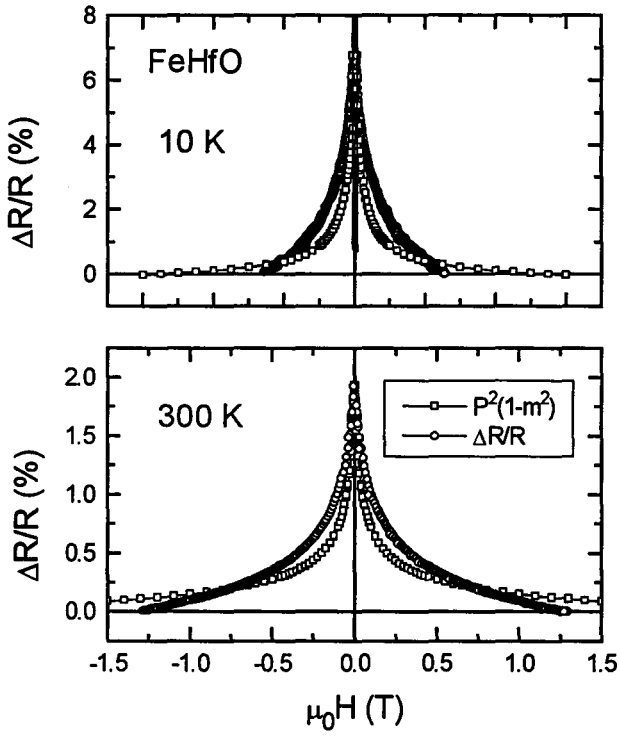

Fig.5.34 Calculating curve showing $1\text{-}m^2$ where m is the reduced magnetization and MR as a function of the magnetic field for (a) T=10 K and (b) T=300K.

The deviation can not be explained by the spin-flip scattering as discussed above, at least not in the situation were the resisitivity is described by just assuming tunnel phenomena. But it can also not be explained by assuming a percolating resistance shunted parallel to the tunnel resistance. This confirms that the granular structure of FeHfO is rather complicated and can not be described quantitatively to a satisfatorily degree by very simple equivalence circuit models.

6 Application: the thin film inductor[1]

6.1 Introduction

In the passive integration project within the group Microsystems technology, research is performed on planar inductors. These are thin film devices that basically consist of a square coil of Au or Al typically covering an area of 3 mm^2 or less on a Si substrate. Generally speaking the devices may serve as inductances in LCR-circuits for application in resonators or band filters, sensors, dc-dc converters [34] , micro actuators [35], planar micro transformers for use in micro switching converters [36] and magnetic integrated circuits [37]. At Philips research one of the applications that one currently focusses on are inductors for use in front-end filters in FM-radio typically operating at 100 MHz. The principle aim is to develop inductors combining

- an as high as possible inductance L per unit area
- an as high as possible quality factor Q[2]
- the lowest possible costs

For a solonoidal coil it is well known that if one fills the inner part with a soft-magnetic material having relative magnetic permeability μ_r that the inductance L increases by a factor μ_r. The reason is that the magnetic reluctance (resistance) R that the flux experiences, drops by a factor μ_r: $R=l/\mu_0\mu_r A$ with l and A he length and cross-sectional area of the coil, respectively. For a solonoidal coil the inductance L is given by $L=N^2/R$ with N denoting the number of windings. Returning to the planar inductor it may be clear that by applying a soft magnetic layer above and below the square coil, the magnetic reluctance of the flux path around the conductor is reduced resulting in an enhancement of the inductance L. In turn, this enhancement may offer the opportunity to lower the costs of the inductor or alternatively to miniaturize it further.

It is the aim of the present work to investigate to what degree the inductance can be enhanced. The idea to enhance L of planar inductors using soft-magnetic layers is not new: in several industrial labs. research on this subject is being performed. This research does not only focus on the mere application of magnetic layers but is also directed at finding new geometries (see e.g. [38]-[66]), other than that of the square coil considered here. In the present work we focus on the square coil with a soft-magnetic layer at a certain distance above and below it. The soft-magnetic layers where chosen of MnZn-ferrite and FeHfO. This is because of the

[1]This chapter is a part of a Nat. Lab Techn. Note by Bloemen *et. al.* [33]

[2]The quality factor Q is defined as $\mathrm{Im}(Z)/\mathrm{Re}(Z)$ with $\mathrm{Re}(Z)$ and $\mathrm{Im}(Z)$ the real and imaginary parts of the complex impedance Z of the coil. Neglecting capacitive effects the quality factor is given by $Q=\omega L/R$ with R the electrical resistance of the coil and ω the angular frequency.

presently available materials these exhibited the highest electrical resistances[3]. The latter property is important since the inductors should operate up to the highest possible frequencies. If low resistive magnetic layers would have been used, the rf coil fields would be shielded by eddy currents that run within the magnetic layers. This screening causes the magnetic permeability to drop and hence eliminates the enhancement of L. Though this eddy current effect is unwanted for planar inductors, such low resistance, high permeability soft-magnetic layers may be exploited successfully in shielding applications where one wants to limit disturbing rf-fields on the environment. However, this is not subject of the present work.

6.2 Experimental

A schematic representation of the inductors studied in this work is given in Figure 6.1.

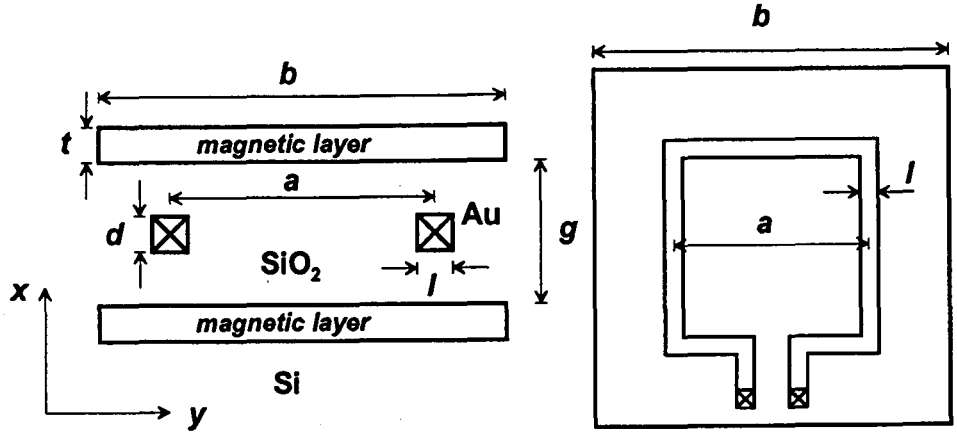

Fig. 6.1 Schematic representation of a planar inductor defining the used symbols; cross-section (left) top view (right).

The inductors have been prepared on 40 × 40 mm^2 Si substrates terminated with a 2 μm SiO_2 layer. SiO_2 deposited at 300°C with CVD has been used to insulate the conducting coil (made of Au) from the soft-magnetic layers. On one wafer six coils are present having different sizes i.e. the side length assumes the values 420, 670, 920, 1170, 1420 and 1670 μm. The width l and thickness d of the conductors is in all cases 80 μm and 0.3 μm, respectively. The gap g determined by both the thickness of the conductor as well as the SiO_2 was in the present design 1.3 μm. The magnetic layers all have a thickness t of 0.8 μm.

The complex frequency dependent magnetic permeability has been measured using the mutual inductance method by means of a HP4129A impedance analyzer or with a single coil inductance method using a HP4195A network spectrum analyzer. Here, the rf field was directed along the long axis of the strip parallel to the film plane. See chapter 3 for a description of this technique. The complex frequency dependent electrical impedance of the inductors has been measured using the s-parameter technique described elsewhere [67].

[3]Here, available means: that could be readily sputtered. Other soft-magnetic materials such as NiZn-ferrite have considerably higher resistances.

6.3 Relevant properties of the used soft-magnetic layers FeHfO and MnZn-ferrite layers

In this section we briefly discuss the most relevant magnetic and electric properties of the FeHfO and MnZn-ferrite layers. For an extensive discussion regarding FeHfO we refer to chapter 5. Here, we will focus on the electrical resistivity and the magnetic permeability. These quantities have been measured either from strips that have been cut form the 40 × 40 mm^2 Si wafers *after* complete processing of the inductor or on other strips on which the soft- magnetic layers have been deposited under the same conditions. It may be clear that the magnitude of the magnetic permeability plays an essential role in the enhancement of the self-inductance L of the coil whereas the resistivity plays a role to what degree eddy current and displacement losses occur. In Table X the dc resistivities and the low frequency magnetic permeabilities of the FeHfO and MnZn-ferrite layers are collected.

Table X: DC resistivity and magnetic permeability μ of sputtered MnZn-ferrite and FeHfO thin films. For the latter μ is anisotropic when the film is annealed in magnetic field.

film composition	*ρ ($\mu\Omega$cm)*	*μ($\leq$13 MHz)*
Mn-Zn-ferrite	1-2 ·10^6	15
FeHfO (as deposited)	2000	530
FeHfO (hard axis)	1000	1400
FeHfO (45°)	1000	750

Contrary to FeHfO, in the case of MnZn-ferrite no uniaxial magnetic anisotropy has been induced by a magnetic anneal treatment. The FeHfO layers have been annealed with rapid thermal processing (RTP) at 400°C for 5" in magnetic field along the short axis of the strip (3rd row in the table) and at an angle of 45° with respect to the long axis of the strip (4th row in the table). It is clear that the permeability depends on the direction of the rf field relative to the magnetic hard direction. Figure 6.2 on the next page displays the full angular dependence of the permeability measured at 100 kHz for FeHfO. Here, the angle (ϕ) that has been avried is the angle between the direction of the rf measuring field and the magnetic hard direction.

The solid line represents a fit of Eq. (2.20). Knowledge of this anisotropic behavior is relevant to our inductor since in the present case of a rectangular coil, flux transport occurs in *two* mutually perpendicular directions viz. locally perpendicular to the conductor. This draws on the question which case would yield the highest inductance: (a) the parallel case in which the annealing is performed with the field parallel to one of the conductor sides (see Fig 6.3) or (b) the case of annealing at an angle of 45° relative to the conductor sides.

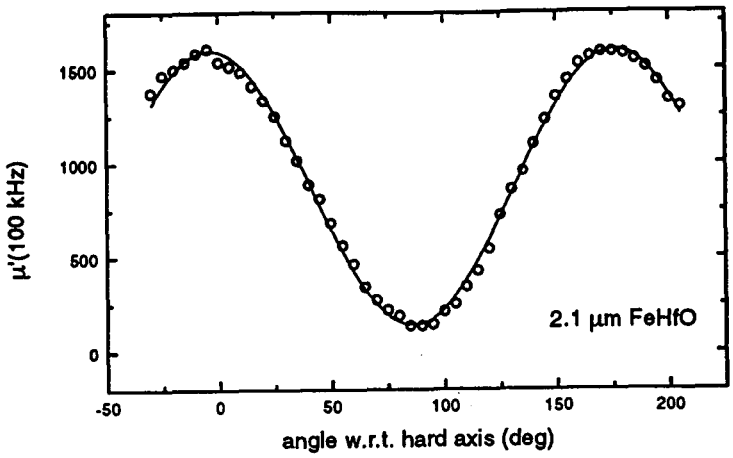

Fig. 6.2 Magnetic permeability as a function of the angle between the measuring direction of the rf-field and the hard axis direction.

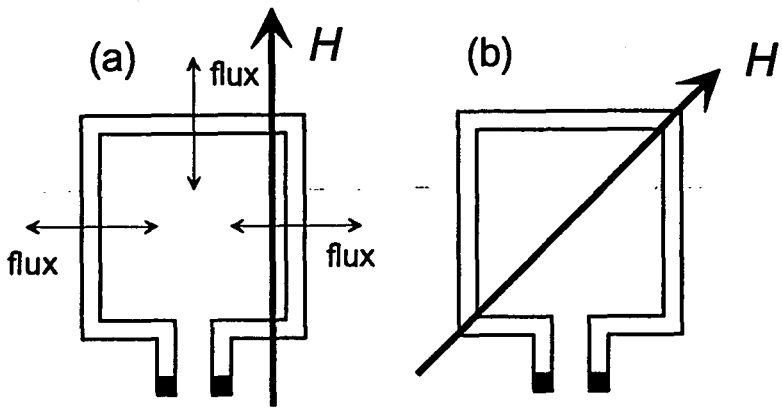

Fig 6.3 Two different possibilities to anneal the inductors (a) with the applied magnetic field parallel to one of the conductor sides or (b) with the field at 45° with the conductors.

In the parallel case one has the highest permeability for two conductors whereas the other two conductors ('with low permeability') will contribute considerably less to the inductance. On the other hand for the 45° case all conductors contribute equally to L but with a permeability that is roughly half of the maximum achievable permeability (neglecting μ_{wall} in first approximation). This question will be answered later on. In the case of MnZn-ferrite this issue does not play a role.

Apart from the dc properties the frequency dependent properties are also of interest since the inductors have to operate at high frequencies. Fig. 6.4 shows the frequency dependence of the magnetic permeability of a strip that has been cut from that part of the Si wafer that

contained no inductors i.e. the measurement is basically performed on a 0.8 μm FeHfO /spacer/0.8 μm FeHfO sandwich.

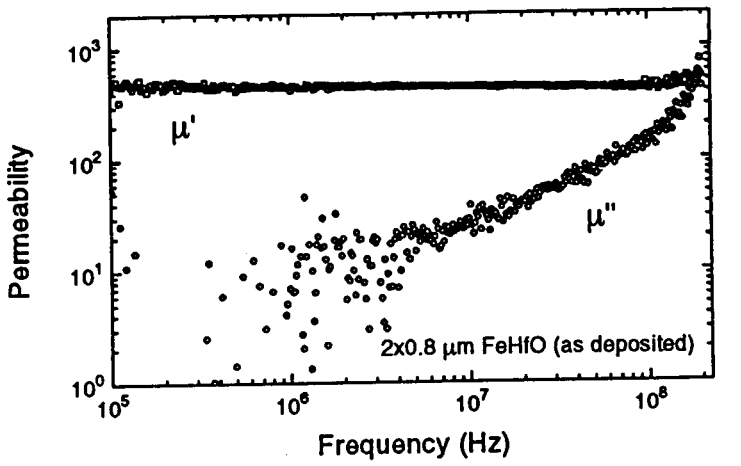

Fig. 6.4 Frequency dependence of a 0.8 μm FeHfO/spacer/0.8 μm FeHfO sandwich in the as-deposited state. The spacer consists of 0.5 μm SiO_2/0.3 μm Au/0.5 μm SiO_2.

Here, the spacer consists of 0.5 μm SiO_2 /0.3 μm Au/0.5 μm SiO_2. The sample has thus received the same (thermal) treatments as the inductors. For the present case the sample was measured in the as-deposited state (no magnetic anneal treatment). It is seen that the real part of the complex magnetic permeability μ' is constant up to a frequency of 190 MHz. Based on the behaviour of μ'' it is expected that just above 200 MHz the permeability will roll-off. The behavior for the annealed sample is similar except for the magnitude of the permeability (see Table X).

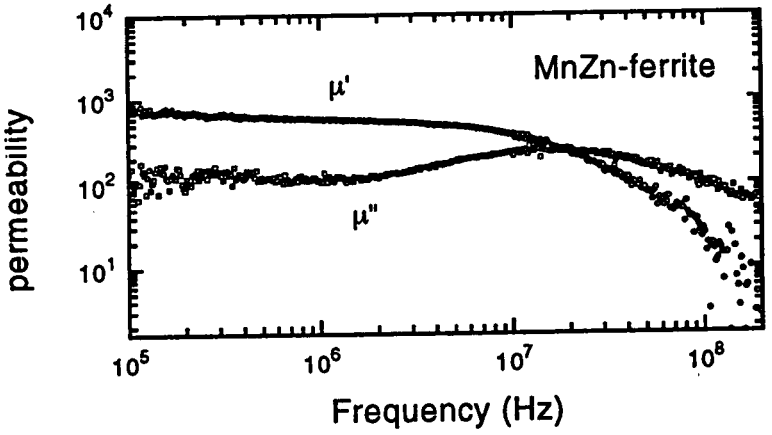

Fig. 6.5 Frequency dependence of a bulk 500 μm MnZn-ferrite film. The ferrite is not sputtered: it is the same as the ferrite used in the yokes of video heads.

The behavior of the MnZn-ferrite is as follows. The permeability (μ') of the 0.8 μm thick films remains constant and equal to 15 up to frequencies of 13 MHz. Above this frequency no reliable measurements have been performed. For a bulk sample (500 μm thick) a measurement is shown in Fig. 6.5. We have to note however that this does not correspond to sputtered MnZn-ferrite but to ferrite used in the yokes of discrete sandwich video heads. It is seen that although the resistance of the ferrite is relatively high, the permeability rolls off at already 10 MHz. It is well known that the behavior is not determined by eddy currents but by ferromagnetic resonance. Since the bulk film has a considerably higher permeability (about 800) than the 0.8 μm thick MnZn-ferrite film used in the inductors (μ=15) it is expected (based on Snoeks limit) that the roll-off for our film will occur at a frequency that is much higher: based on Snoeks limit at 800/15=53 MHz = 530 Mhz.

6.4 Magnetic transmission line modelling

In this section an analytical expression is derived for the inductance of a Hoop-type planar inductor in terms of its dimensions and the magnetic permeability of the magnetic layers. The result can be used to analyze and understand the experiments and provides insight that enables us to indentify bottle necks in the inductor design and thereby provides a basis for future better designed inductors.

Since magnetic transmission line models have proven to describe thin film heads with very good accuracy we have adopted the same approach to derive an expression for L. Earlier this has also been done by Sato *et al.* [68] for circular shaped multi-turn coils and not for the general case of a finite fringing resistance (see below). Roshen *et al.* [69] also considered the problem but again considered the case of circular coils. Furthermore his derivation employing the method of current images does not give simple formulas from which the relation between the inductor characteristics and the coil parameters are clear. Below we apply the magnetic transmission line model on a rectangular coil. It will appear that this will result in a relatively simple formula for the inductance and consequently leads to a very transparent physical picture.

The magnetic transmission line model is actually nothing else than solving the magneto-static problem with the correct boundary conditions i.e. applying the classical laws of electromagnetism neglecting time dependencies i.e. applying Ampère's law and demanding conservation of magnetic flux and continuity of magnetic potential.

To calculate the inductance L we need to calculate how the magnetic flux, generated by a current through the coil, flows through the layers. The inductance L is defined as the ratio between the flux enclosed by the current and the magnitude of this current:

$$L=\Phi_{encl.}/I. \tag{6.1}$$

Our coil consists of four indentical conductors arranged in a square, see Fig. 6.1. The sides have a length denoted by a. The two magnetic layers have both a thickness t and are at mutual distance g symmetrically with respect to the coil. The surface area that the magnetic layers

cover is preferably larger than the coil area and is for the present model assumed to be of square shape with side lengths denoted by b ($b>a$). Another relevant parameter for the behavior is the width of the conductor making up the coil. This width is denoted by l. The thickness of the conductor is represented by d. Since the essential physics is already fully contained in the simpler problem of one straight conductor between two magnetic layers it is sufficient to solve this problem first. The solution of the full problem including the four conductors forming the square loop is simply constructed from the solutions of the simpler problem.

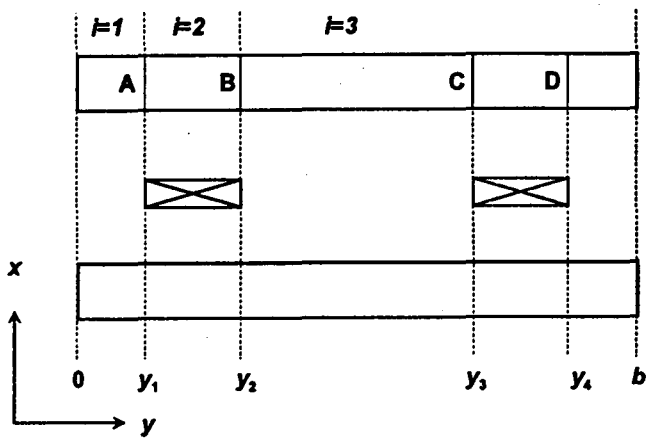

Fig. 6.6 Schematic representation of the cross-section of a planar inductor defining the coordinates and three regions denoted by i=1,2 and 3.

For a given conductor with a current I flowing in the z-direction (see Fig.6.6) it can be shown that the magnetic flux Φ flowing in the magnetic layers satisfies the following differential equation [70]:

$$\frac{\partial^2 \Phi}{\partial y^2} - \frac{1}{\lambda^2}\Phi = -\frac{\alpha}{\lambda^2} I. \tag{6.2}$$

Here, the following assumptions have been made: (i) the flux Φ is travelling solely in the y-direction within the magnetic layers, (ii) there is no x-dependence, (iii) the leakage fluxes from one magnetic layer to the other are normal to the plane of the layers and (iv) time dependencies i.e. eddy current effects are left out.

The parameters λ and α that have been introduced in Eq. (6.2) are defined as:

$$\lambda = \sqrt{\frac{\mu_r t g}{2}}, \tag{6.3}$$

$$\alpha = \frac{\mu_0 \mu_r t a}{2l}. \tag{6.4}$$

These parameters are the two important physical constants of the device. The constant λ is a characteristic decay length for magnetic flux. It sets the length scale at which important

dependencies and effects will occur. The constant α represents a characteristic magnetic permeance or in other words a specific conductivity for magnetic flux. In the present case it is the inverse magnetic reluctance[4] of a magnetic layer with cross section *ta* and magnetic path length $2l$. This parameter will set the order of magnitude of the inductance.

The general solution of Eq. (6.2) assumes the form:

$$\Phi(y)=A_i\exp(y/\lambda)+B_i\exp(-y/\lambda)+\alpha I, \tag{6.5}$$

where the subscript i denotes a particular region of the inductor. Here, it is to be noted that at positions where no conductor is present the current term in Eqs. ( ) and ( ) should be left out (I=0).

Three regions depending on the location of the conductor need to be discerned. They are labeled with i =1, 2 and 3 as indicated in Fig. 6.6 on the preceding page. The y coordinate for region 1 ranges from 0 to y_1. Similarly regions 2 and 3 are determined by $y_1 \le y \le y_2$ and $y_2 \le y \le b$, respectively. Here, $y_1=(b-a-l)/2$ and $y_2=(b-a+l)/2$. As mentioned, for the solution in region 1 and 3 one needs to set I=0 in Eq. (6.5). The boundary conditions which the flux in the several regions has to satisfy are:

1. At y=0 and y=b:

$$g\frac{\partial \Phi}{\partial y}=R\Phi. \tag{6.6}$$

This expresses that the magnetic potential difference at the edges of the magnetic layers is equal to the magnetic resistance R for the flux to cross from one side of the magnetic layer through air to the other magnetic layer times this flux. This is the magnetic analogon of Ohm's law.

2. At y_1 and y_2 the flux as well as the derivative of the flux should be continuous across the boundaries. Here, continuity of the derivative is a result of the fact that the magnetic potential is continuous.

These boundary conditions result in six linear equations for the the six unknown coefficients and A_i and B_i. It is a straightforward matter to solve these equations. As an example we give the expression for B_2 in the case of an infinite fringing resistance R i.e. no fringing flux at the faces of the magnetic layers.

$$B_2=\frac{\alpha I}{2\sinh(b/\lambda)}\left[\cosh\left(\frac{b+a-l}{2\lambda}\right)-e^{b/\lambda}\cosh\left(\frac{b-a-l}{2\lambda}\right)\right]. \tag{6.7}$$

[4]The magnetic reluctance R of a piece of magnetic material of length l, relative magnetic permeability μ and cross-sectional area A is defined in complete analogy with the electrical resistance as $R=l/\mu_0\mu_r$.

The other coefficients, also for the more general case of a finite fringing resistance, are listed in appendix B. Using these expressions the flux generated as a function of position y by a single conductor carrying a current I can now be calculated straightforwardly.

In an inductor the four current conductors making up the coil behave identically and will generate a flux having the same spatial dependence. The total flux is thus simply the sum of the fluxes of each conductor. To calculate the contribution of one conductor to the enclosed flux $\Phi_{encl.}$ we consider again Fig. 2.6. The vertical lines A-D at the boundaries between the several regions denote imaginary cross sections through which flux enters and leaves a region. For example, the flux that crosses the inside area of the coil must be equal to the flux leaving the magnetic layer. The latter is equal to $\Phi(y_2)$-$\Phi(y_3)$. One may be tempted to assign this to the enclosed flux $\Phi_{encl.}$ in Eq. (6.1). However, this is not correct since flux also crosses the current conductor itself and is thus enclosed by part of the current. Obviously this also contributes to and should be taken into account in the calculation of L. In appendix C it is argued that the correct expression for $\Phi_{encl.}$ is given by:

$$\frac{1}{4}\Phi_{encl.}=\frac{1}{l}\int_{y_1}^{y_2}\Phi_2(y)dy. \tag{6.8}$$

This becomes a rather cumbersome formula if one substitutes Eq. (6.5) with for A_2 and B_2 the expressions given by Eqs. (B.2) and (B.3). A convienient expression can be obtained by taking the limit $b/\lambda\rightarrow\infty$. It is an easy matter to show that the resulting expression is given by:

$$L_{b=\infty}=4\alpha\{1-\frac{\lambda}{l}[1-\exp(-l/\lambda)]\} \tag{6.9}$$

or alternatively after substituting for λ and α the expressions given by Eqs. ( ) and ( ):

$$L_{b=\infty}=4\frac{\mu_o\mu_r ta}{2l}\{1-\frac{1}{l}\sqrt{\frac{\mu_r tg}{2}}[1-\exp(-l/\lambda)]\} \tag{6.10}$$

For the present experiment this limit is appropriate since the magnetic layers extend across the entire Si wafer except where the contacts have been made to facilitate impedance measurements. Considering Eq. (6.10), a number of remarks can be made. The inductance can be viewed as the product of three factors (i) a geometry dependent factor between braces involving the characteristic dimensions and the permeability dependent magnetic decay length (ii) a factor representing the (inverse) magnetic resistance that flux experiences within the magnetic layers when flowing around a single conductor ($\mu_0\mu_r ta/2l$) and (iii) a factor 4 counting the number of conductors. The factor between braces can be seen as a factor that reduces the enhancement of the magnetic resistance due to the presence of air gaps in the inductor. It accounts for the fact that L is not proportional to μ_r but rather to $\sqrt{\mu_r}$: it can be shown rather easily that in the limit of large Eq. (6.10) transforms into:

$$L_{(\mu_r b)=\infty}=4\mu_0 a\sqrt{\frac{\mu_r t}{8g}} \tag{6.11}$$

Furthermore, note that the inductance, unlike for the case of the conventional solonoidal coil does not scale with the area a^2 enclosed between the conductors but scales with the side length a. Ofcourse the latter is due to the fact that the decay length is much smaller than the side length a i.e. the majority of the flux is concentrated in a region λ around the conductor. To conclude this section we remark that the factor 4 only applies if all four conductors contribute equally to the enclosd flux i.e. if the magnetic permeability is isotropic. This is generally not the case certainly for materials where the large permeabilities are obtained by magnetic annealing. This issue has already been mentioned in section 6.3 where the question has been raised what the optimum direction of the magnetic field during the anneal treatment should be. This question can now be answered. If one anneals with the field parallel to one pair of the conductors then one pair of conductors does in first approximation not contribute to L because μ_r is relatively low for that pair whereas the other pair contributes maximally:

$$L_{\parallel}=2\mu_0 a\sqrt{\frac{\mu_r t}{8g}} \tag{6.12}$$

Annealing at an angle of 45° yields the case that all four conductors contribute equally but with 1/2 the maximum permeability:

$$L_{\parallel}=4\mu_0 a\sqrt{\frac{\mu_r t}{16g}} \tag{6.13}$$

It is now clear that the latter case, i.e. annealing at 45°, is preferred since it yields a factor $\sqrt{2}$ larger inductance than in the parallel case (Eq. (6.12)).

6.5 Results and Discussion

In this section the results of the impedance measurements of the planar inductors are presented. The complex impedance Z of the inductor will be frequency dependent simply because of its inductance L and also because of the stray capacitance C of the device i.e. the coil is capacitively coupled to the magnetic layers and to the substrate so that displacement currents may flow through these and therby short circuit the coil. In Fig. 6.7 this situation is schematized in a cross-section for part of the inductor.

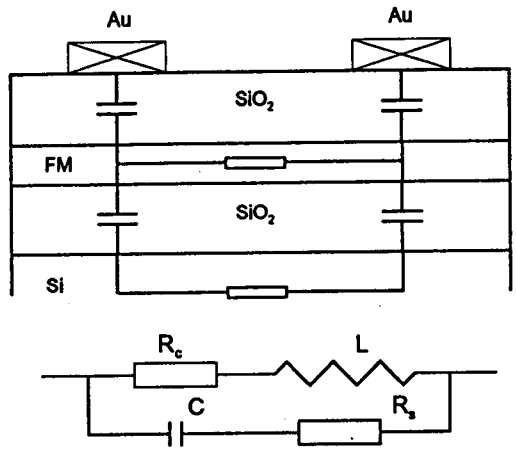

Fig 6.7 Schematic representation of part of the inductor and an equivalent electrical circuit. The Au coil is capacitively coupled to the ferromagnetic (FM) layer and to the Si substrate via the dielectric SiO_2 layers.

The figure also shows an equivalent electrical circuit that simplifies the situation further. Based on this circuit the electrical impedance of the inductor may be written (approximated) by

$$\frac{1}{Z}=\frac{1}{R_c+j\omega L}+\frac{1}{R_s+1/j\omega C}. \qquad (6.14)$$

Here, R_c represents the coil resistance, R an$_s$ equivalent resistance determined by the thicknesses and resistivities of the magnetic layers and the substrate, and C a capacitance determined by the thickness and relevant area of the SiO layers. The inductance L is in general complex and frequency dependent because the permeability is. However, at low angular frequencies ω capacitive effects can be neglected and the permeability is to a good approximation frequency independent so that Z equals $R+j\omega L$. In this limit the inductance can be obtained from the slope of the imaginary part of Z with ω.

The frequency dependence of Z has been measured for several coil sizes a and for each measurement L has been determined as just discussed. The results are collected in Fig. 6.8 displaying the inductance L versus a for coils were no magnetic layers have been used (open squares), for the case that MnZn-ferrite was used as a magnetic material (solid up triangles), for the case that FeHfO was used as a magnetic material in the as-deposited state (solid circles) and for the case of FeHfO annealed in a magnetic field directed at an angle of 45° relative to the sides of the coil (solid down triangles). The solid lines are calculations based on the transmission line formula (Eq. (6.10)). Here, the only free parameter to be chosen was the magnetic permeability. The values that have been used in the calculation are indicated in the figure also. The line labeled with 'air' is a calculation for the situation that no magnetic layers are present, from here on referred to as the air-coil or air case. For this case we have used the expression

$$L(air)=\mu_0\frac{a}{2\pi}\{\ln(\frac{4a}{\pi ld})-\frac{7}{4}\},$$

which was obtained from Becker *et.al.* [71][5] .

Here, a is again the side length of the rectangular coil, l is the width of the conductor and d its thickness.

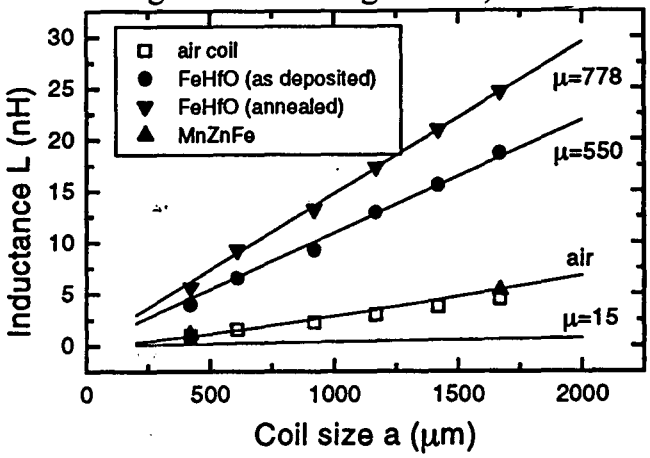

Fig. 6.8. Inductance L as a function of the side length a for the case of an 'air-coil' (open squares), for the case of MnZn-ferrite layers (solid up triangles), for the case of as-deposited FeHfO layers (solid circles) and for the case of annealed FeHfO layers (solid down triangles). The lines represent calculations (see text).

Regarding this figure several remarks can be made.

1. Eq. (6.15) describes the situation of an air-coil rather well, note that no adjustable parameters are involved.

2. The linear dependence of the inductance on the side length of the coil is predicted well by the transmission line model (see Eq. (6.10)).

3. In the case of FeHfO the enhancement of the inductance L relative to the air case is certainly not by a factor equal to the magnetic permeability but much smaller, a factor 6 at best, compared to about 750 based on the permeability.

4. The magnetic permeabilities used in the calculations for the as-deposited (μ=550) state as well as for the annealed state (μ=778) are rather close to the experimental values (μ=530 and

[5]The in [71] derived formula was for a circularly shaped coil. We have transformed this formula to the present one for a rectangular coil by replacing the radius of the conductor wire by $\sqrt{(ld/\pi)}$ (i.e. keeping the cross-sectional area through which the current flows within the conductor wire the same) and by replacing the coil radius by $4a/2\pi$ i.e. keeping the circumference (of the area enclosed by the current) the same.

μ=750, respectively).

5. Application of the MnZn-ferrite layers (with μ=15) does not yield any significant enhancement at all.

The reason for the rather limited enhancement (factor 6) is understood from and correctely described by the transmission line model. The small enhancement is due to the presence of the air gaps. As discussed, these effectively dominate the magnetic reluctance and cause the inductance to be proportional to $\sqrt{\mu}$ rather than to μ.

For the low permeability case of MnZn-ferrite, the magnetic transmission line model fails to describe the experiments. The calculated line (labeled with μ=15) gives considerably lower values than found experimentally (solid up triangles). The reason for this discrepancy originates in one of the assumptions made in the model viz. it was assumed that the magnetic flux lines cross the air gap perpendicularly to the plane of the layers. Ofcourse at low magnetic permeabilities this will no longer be the case i.e. other flux paths, more resembling the curved paths in case of an air coil, will exhibit a lower reluctance. Therefore, the transmission line model calculates a too high effective magnetic reluctance and thus underestimates the inductance. Finite element calculations would be needed to predict the behavior in this low permeability regime.

So far we have limited the discussion to the static situation in particular to the inductance. For applications the quality factor and the frequency dependence are also important. Fig.6.9 shows the frequency dependence of the real (Re(Z)) and imaginary part (Im(Z)) of the complex impedance Z. Also the inductance calculated as L=Im(Z)/2πf and the quality factor calculated as Q=Im(Z)/Re(Z) are shown. The data pertain to planar inductors with or without the application of a soft-magnetic layer and all have a coil side length a of 420 μm.

It is seen for all cases i.e. the air coil (open circles) as well as for the coils with the FeHfO (solid squares) and MnZn-ferrite layers (open triangles) that the real part of increases with frequency. This is attributed to dissipation mechanisms related to displacement currents running across the SiO_2 layers and subsequently within the magnetic layers and or the substrate and to ferromagnetic resonance losses within the magnetic layers. For the FeHfO case the increase of Re(Z) occurs at a lower frequencies for three reasons: (i) because the inductance is higher causing the electronic resonance frequency (roughly given by ω=1/$\sqrt{LC}$) to shift to lower values, (ii) because the resistivity of the FeHfO is lower than that of the MnZn-ferrite thus facilitating an easier flow of displacements currents and (iii) because of the larger dissipation related to ferromagnetic resonance in the FeHfO. Note with respect to the latter effect that the imaginary part of the magnetic permeability will appear as a resistance and that this imaginary part continuously increases with frequency, see Fig. 6.4.

What is also seen from the figure is that the inductance starts to roll-off already at about 100 MHz. This is lower than the frequency (190 MHz, see Fig. 6.4) at which the magnetic permeability rolls off. The difference is attributed to capacitive effects: since L is calculated from Im(Z)/2πf all parts of the device that give rise to a contribution to Z having an imaginary component will enter in the behavior of L[6].

[6]Only at low frequencies it is correct to interpret Im(Z)/2 as a true inductance and thus only at low frequencies the behavior of L will mimic the behavior of the magnetic permeability

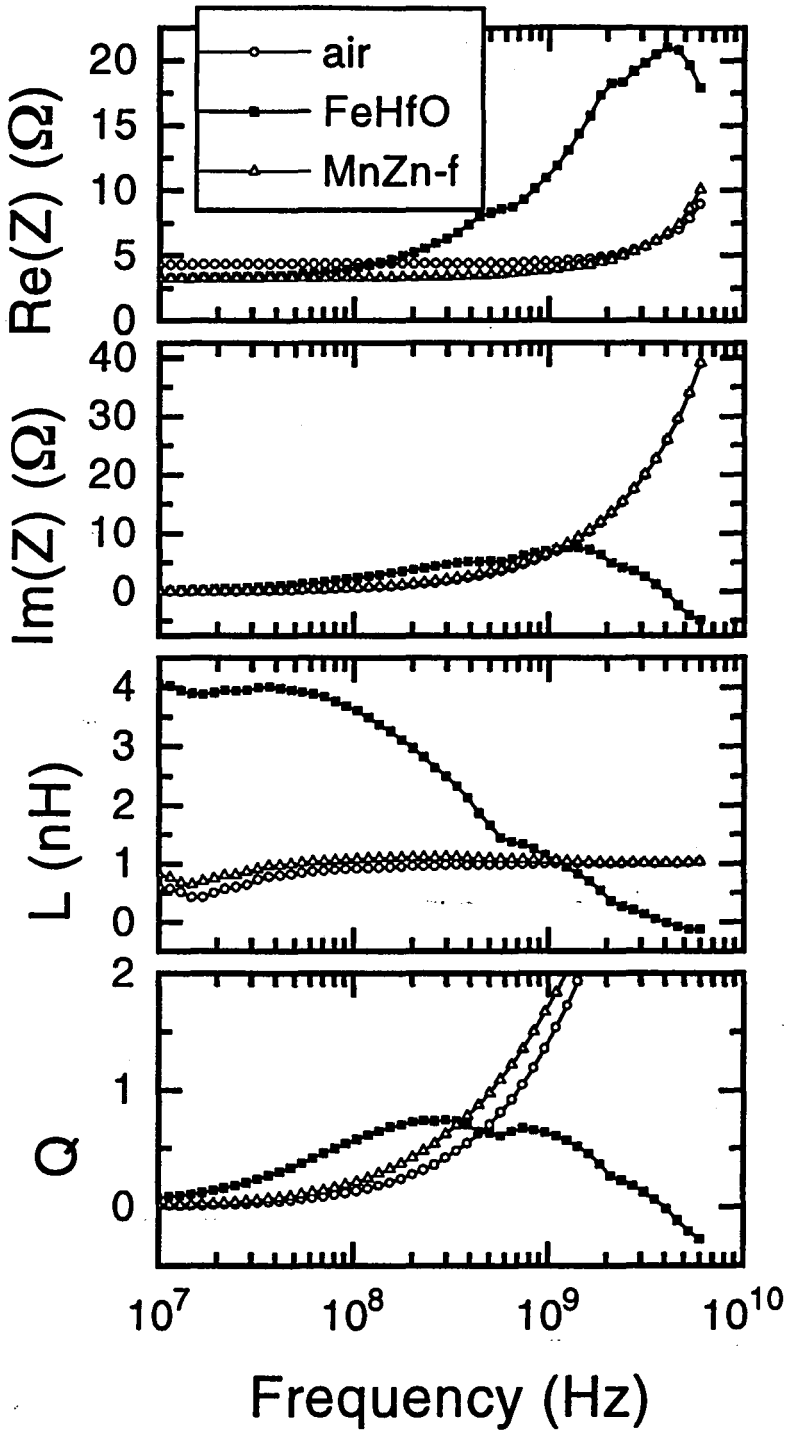

Fig. 6.9. The frequency dependence of the real (Re(Z)) and imaginary part Im(Z)) of the complex impedance Z and of the inductance L=Im(Z)/2πf and quality factor Q=Im(Z)/Re(Z) of three types of planar inductors with a=420 μm, the air case (open circles), the case of as deposited FeHfO layers (solid squares) and the case of MnZn-ferrite layers (open squares).

7 Summary and conclusions

By reactive sputter deposition in an Ar/O_2 gas mixture FeHfO thin films with thicknesses between 0.7 μm and 10.5 μm have been prepared. The parameter to which the soft magnetic properties are most sensitive seems to be the oxygen flow. For the optimum conditions, good soft magnetic behaviour can be achieved: a saturation magnetization B_s of 1.1 T, a (relative) magnetic permeability μ_r at 100 kHz of 1500 and a resisitivity ρ of about 1000 μΩcm. The remaining problem is the relatively large magnetostriction constant λ_s of $5 \cdot 10^{-6}$ which is a factor 10 too large. This is the main reason why this material is not suitable for application as flux guide material in magnetic recording heads.

The HF-permeability set-up is automatized and optimized to measure permeabilities up to 200 MHz. It is demonstrated that it is necessary to take into account a capacity correction. This is because at large frequencies the coil starts to resonate. By making use of the HF permeability set-up, the permeability as a function of frequency of several FeHfO films is measured up to 200 MHz. It is shown that the roll-off of the permeability at frequencies near those that are presently accessed in experiment and in application is mainly determined by ferromagnetic resonance. Further increasing the resistivity in the future is therefore ineffective. Additionally, it is shown that local eddy currents instead of currents which flow through the entire film will not give rise to a decrease in the permeability at large frequencies. At low frequencies the permeability is determined by a combination of rotation magnetization and domain wall processes. The latter contribution has been calculated also. The fits are in reasonable agreement with the experimental data.

FeHfO films sputtered with a larger oxygen flow appear to exhibit a very large resistivity near 10^5 μΩcm combined with a moderate magnetic permeability (≈200). Such FeHfO films are therefore candidates for use as seperation oxide between the fluxguide and the MRE in a read head. This may improve the efficiency of the thin film head considerably. By increasing the amount of oxygen in the sputter clock during the reactive sputter process, the properties of the FeHfO thin films change from good soft magnetic behaviour exhibiting neglegibly small magnetoresistance to films with a relatively large magneto-resistance ratio and poor soft magnetic properties. This implies that good soft magnetic behaviour is not compatible with a sufficient GMR behaviour in view of applications. It has been observed that the GMR ratio of the FeHFO is strongly temperature dependent. This can not be explained by assuming that spin dependent tunneling is the only phenomenon that takes place. It is shown that an acceptable description of this temperature behaviour can be obtained by assuming a certain amount of spin-flip scattering.

Finally, a magnetic transmission model has been developed and gives a usefull mathematical description of a thin film inductor. The model has provided considerable insight. The effect of different parameters and dimensions on the behaviour of the impedance and the inductance of this inductor is well understood and described. It is demonstrated that the inductance increases proportional with $\sqrt{\mu}$ as distinct from a normal coil with a magnetic core where the inductance increases proportional with the permeability. Furthermore, it is shown that the inductance scales with the side length a of the coil instead of the enclosed area a^2 fore a normal coil. This is because the flux is concentrated near the conductor wires. By making use of soft magnetic layers the quality factor and inductance are increased relative to an air coil.

References

[1] H.J. de Wit, *Rep. Prog. Phys.* **55** (1992) 113.

[2] Y. Hayakawa, N. Hasegawa, A. Makino, S. Mitani and H. Fujimori, *J. Magn. Magn. Mater.* **154** (1996) 175.

[3] A. Makino and Y. Hayakawa, *Mat. Sci. Eng.*, **A181/A182** (1994) 1020.

[4] A. Makino and A. Kojima, *IEEE Trans. Magn. Jpn.*, Vol. 9, No. **4** (1994) 92.

[5] H. Fujimori, *Scripta Metallurgica et Materialia*, Vol. 33, Nos. **10/11**, (1995) 1625.

[6] Y. Hayakawa, N. Hasegawa, A. Makino, S. Mitani and H. Fujimori, *J. Magn. Soc. Jpn.* **20** (1996) 425.

[7] S. Furukawa, S. Ohnuma, F. Matsumoto, H. Fujimori and T. Masumoto, *IEEE Trans. Magn. Jpn.*, Vol. 9, No. **5** (1994) 80.

[8] N. Kobayashi, S. Ohnuma, H. Fujimori and T. Masumoto, *J. Magn. Soc. Jpn.* **20** (1996) 469.

[9] N. Kobayashi, S. Ohnuma, H. Fujimori and T. Masumoto, *J. Magn. Soc. Jpn.* **20** (1996) 473.

[10] W.D. Li, O. Kitakami, Y. Shimada, K. Ishiyama and K.I. Arai, *J. Magn. Soc. Jpn.* **20** (1996) 461.

[11] W.N. Wang, Z.S. Jiang and Y.W. Du, *J. Appl. Phys.*, **78** (1995) 6679.

[12] C. Kittel, *Rev. Mod. Phys*, Vol. 21 nr. **4** (1949) 541.

[13] Becker, R. & Döring, W. 1939 *Ferromagnetismus*. Berlin: Springer (Photo-lithoprint reproduction, 1943, Ann Arbor, Michigan: Edwards).

[14] E.C. Stoner, F.R.S. and E.P.Wohlfarth, *IEEE Trans. Magn.*, Vol. 27, No. **4** (1991).

[15] S. Chikazumi, *Physics of magnetism*, Robert E. Krieger Publishing Co., Malabar (1964).

[16] <K>

[17] rho O > N

[18] A. Fert and I.A. Campbell

[19] P. Sheng, B. Abeles, and Y. Arie, *Phys. Rev. Lett.* **31**, 44 (1973).

[20] J. Iinoue and S. Maekawa, *Phys. Rev. B*, Vol 53, Nr. **18** (1996) 927

[21] J.F.C. Bernards, A.E.T. Kuiper and H.J. de Wit, Nat. Lab. Technical Note 307 (1993).

[22] E. van de Riet, Nat. Lab. Technical Note 238 (1995)

[23] J.M. Huijbregtse, *Soft magnetic FeHfO films with high resistivity*, Graduation thesis (1996).

[24] J.L. Vossen and J.J. Cuomo, *Thin film processes* ed. J.L. Vossen and W. Kern, Academic Press, Inc., Orlando (1978).

[25] F. Roozeboom, J.J.M. Ruigrok, W. Klaassens, H. Kegel, M.Falter and H. Walk, *Mat. Res. Soc. Symp. Proc.* **429** (1996) in press.

[26] Schmidt et al.

[27] E. van de Riet. *J. Appl. Phys* **76** (1994) 584.

[28] $R_s=CV/I$.

[29] Scherrer Eq.

[30] v.d . Zaag, Nat. lab. Tech. Note

[31] Bloemen, Rulkens, srt. in prep.

[32] Fujimori

[33] T. Sato, H. Tomita, A. Sawabe, T. Inoue, T. Mizguchi and M. Sahashi, A magnetic thin film inductor and its application to a MHz switching dc-dc converter, IEEE Trans. Magn. 30 , 217 (1994).

[34] C.H. Ahn and M.G. Allen, A new toroidal-meander type integrated inductor with a multilevel meander magnetic core, IEEE Trans. Magn. 30 , 73 (1994).

[35] M. Mino, T. Yachi, A. Tago, K. Yanagisawa and K. Sakakibara, A new planar microtransformer for use in micro switching converters, IEEE Trans. Magn. 28 , 1969 (1992).

[36] K. Shirakawa, K. Yamaguchi, M. Hirata, T. Yamaoka, F. Takeda, K. Murakami and H. Matsuki, Magnetic Integrated Circuit, IEEE Trans. Magn. ?? , 2662 (1990).

[37] K. Kawabe, H. Koyama and K. Shirae, Planar Inductor, IEEE Trans. Magn. 20, 1804 (1984).

[38] I. Sasada, T. Yamaguchi, K. Harada and Y. Notohara, Planar inductors using NiZn ferrite thin plates and the application to high frequency dc-dc converters, IEEE Trans. Magn. 29, 3231 (1993).

[39] M. Ymaguchi, M. Matsumoto, H. Ohzeki and K. Arai, Fabrication and basic characteristics of dry-etched micro inductors, IEEE Trans. Magn. 26 , 2014 (1990).

[40] P. Ciureanu and H. Gavrila, Magnetic Heads for Digital Recording, Elseview, Amsterdam-Oxford-New York-Tokyo-1990, Chapt.6, pp.510.

[41] T. Sato, M. Hasegawa, T. Mizoguchi and M. Sahashi, Study of high power planar inductor, IEEE Trans. Magn. 27 , 5277 (1991).

[42] W.A. Roshen, Analysis of planar sandwich inductors by current images, IEEE Trans. Magn. 26, 270 (1990).

[43] reference for description s-parameter technique to measure impedances

[44] R. Becker, Theorie der Elektrizität, B.G. Teubner Verlagsgesellschaft mbH, Stuttgart 1957.

Acknowledgement

I would like to thank a number of persons for their support and advises during this graduation project, namely:

- prof. W.J.M. de Jonge and dr. F.J.A.M. Greidanus for giving me the opportunity to graduate in the group Magnetism at Philips Research (Nat.Lab.).
- ir. J.P.G. Morel and A. Geven for their support with LABVIEW.
- ing. J.T. Oostveen for his advises regarding the hardware equipment for magnetic permeability measurements, in particular the HP4195A Network Spectrum Analyser.
- ir. G.L.J. Verschueren R. Bitter and dr.ir. H.J.M Swagten for their help with the temperature dependent and magnetoresistance measurements and the many discussions.
- ir. M. Willekens for the SQUID measurements.
- dr.ir. C. Swüste and Liu for the FMR measurements.
- ing. W. Klaassens for a lot of discussions concerning the magnetic properties of the FeHfO thin films.
- ing. M.H.W. van Delden for the frequency dependent impedance measurements of the inductor.
- dr. F. Roozeboom for the rotational annealing experiments.
- dr.ir. A. Kuiper, who performed Auger electron spectroscopy (AES) and Rutherford backscattering (RBS) experiments to determine the composition of the films.
- All members of the group Magnetism of PHILIPS Nat. Lab and the group Cooperative Phenomena at the Eindhoven University of Technology for their good company.

And last but not least:

- dr.ir. P.J.H. Bloemen for his enthusiastic supervising, advising, supporting and discussing the measurement results during my work. He showed me the principles of magnetism, as well in theory, experiment as in applications.

Appendix A: Rotation of magnetization.

Let us consider a domain with a certain easy axis in a magnetic field. In magnetic materials the state of equilibrium is determined in a way that the total energy is minimized. The total energy E_t is the sum of the field energy E_f and the magnetic anisotropy energy E_K

$$E_t=E_f+E_K=-\mu_0 M_s H\cos(\phi_H-\phi_M)+K_u\sin\phi_M, \tag{A.1}$$

per unit of volume, where ϕ_H is the angle between the easy axis and the direction of the magnetic field H (Fig. AB.1). K_u is the constant of uniaxial anisotropy and ϕ_M is the angle between the magnetization and the magnetization direction.

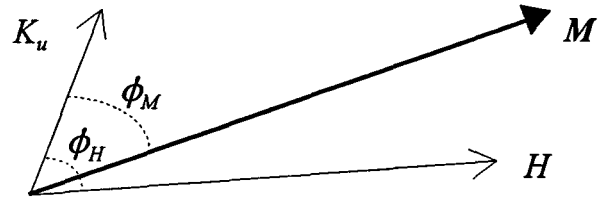

Fig. A.1 Rotation of magnetization in a single domain.

The stable direction of magnetization can be determined by minimizing Eq. (A.1):

$$\frac{\partial E}{\partial \phi_M}=K_u\sin 2\phi_M-\mu_0 M_s H\sin(\phi_H-\phi_M)=0. \tag{A.2}$$

For a weak magnetic field ($H << 2K_u/\mu_0 M_s$), the direction of the magnetization is almost parallel to the easy axis ($\sin\phi_M \approx \phi_M$). Using this assumption and calculating the derivative with respect to the magnetic field H of Eq. (A.2) gives the following expression:

$$\frac{\partial \phi_M}{\partial H}=\frac{\mu_0 M_s\sin(\phi_H-\phi_M)}{2K_u+\mu_0 M_s H\cos(\phi_H-\phi_M)}\approx\frac{\mu_0 M_s\sin\phi_H}{2K_u}. \tag{A.3}$$

The component of the magnetization parallel to the applied field is

$$M=M_s\cos(\phi_H-\phi_M). \tag{A.4}$$

The magnetic susceptibility χ is the derivative of the magnetization with respect to the magnetic to magnetic field H:

$$\chi=\frac{\partial M}{\partial H}=M_s\sin(\phi_H-\phi_M)\frac{\partial \phi_M}{\partial H}\approx M_s\sin\phi_H\frac{\partial \phi_M}{\partial H}. \quad \text{(A.5)}$$

The magnetic permeability $\mu_{r,\mathrm{rot}}$ can thus be calculated as $\mu_r=1+\chi$:

$$\mu_{r,rot}=1+\frac{\mu_o M_s^2}{2K_u}\sin^2\phi_H. \quad \text{(A.6)}$$

Appendix B: Complete expressions for the magnetic flux

The general solution of Eq. (6.2) assumes the form:

$$\Phi(y)=A_i\exp(y/\lambda)+B_i\exp(-y/\lambda)+\alpha I. \tag{B.1}$$

As discussed in section 6.4 three regions are discerned so there are six unknown coefficients. These have to fullfill the boundary conditions given in section 6.4. These result in six linear equations for six unknowns which can be solved using elementary algebra. Assuming an infinite fringing resistance R i.e. no fringing flux at the faces of the magnetic layers, this yields the following expressions for the coefficients:

$$A_1=-\frac{\alpha I}{2\sinh(b/\lambda)}\left[\cosh\left(\frac{b+a-l}{2\lambda}\right)-\cosh\left(\frac{b+a-l}{2\lambda}\right)\right]. \tag{B.2}$$

$$B_1=\frac{\alpha I}{2\sinh(b/\lambda)}\left[\cosh\left(\frac{b+a-l}{2\lambda}\right)-\cosh\left(\frac{b+a-l}{2\lambda}\right)\right]. \tag{B.3}$$

$$A_2=\frac{\alpha I}{2\sinh(b/\lambda)}\left[\cosh\left(\frac{b+a-l}{2\lambda}\right)-e^{-b/\lambda}\cosh\left(\frac{b-a-l}{2\lambda}\right)\right]. \tag{B.4}$$

$$B_2=\frac{\alpha I}{2\sinh(b/\lambda)}\left[\cosh\left(\frac{b+a-l}{2\lambda}\right)-e^{b/\lambda}\cosh\left(\frac{b-a-l}{2\lambda}\right)\right]. \tag{B.5}$$

$$A_3=-\frac{\alpha I}{2\sinh(b/\lambda)}e^{-b/\lambda}\left[\cosh\left(\frac{b-a+l}{2\lambda}\right)-\cosh\left(\frac{b-a-l}{2\lambda}\right)\right]. \tag{B.6}$$

$$B_3=\frac{\alpha I}{2\sinh(b/\lambda)}e^{b/\lambda}\left[\cosh\left(\frac{b-a+l}{2\lambda}\right)-\cosh\left(\frac{b-a-l}{2\lambda}\right)\right]. \tag{B.7}$$

For the general case of a finite fringing resistance R the following coefficients are obtained:

$$A_1 = -\frac{\alpha I}{4f\sinh(b/\lambda)}[e^{-y_3/\lambda} + fe^{y_3/\lambda} - (e^{-y_4/\lambda} + fe^{y_4/\lambda})]. \tag{B.8}$$

$$B_1 = \frac{\alpha I}{4\sinh(b/\lambda)}[e^{-y_3/\lambda} + fe^{y_3/\lambda} - (e^{-y_4/\lambda} + fe^{y_4/\lambda})]. \tag{B.9}$$

$$A_2 = -\frac{\alpha I}{4f\sinh(b/\lambda)}[e^{-y_3/\lambda} + fe^{y_3/\lambda} - e^{-b/\lambda}(e^{y_1/\lambda} + fe^{-y_1/\lambda})]. \tag{B.10}$$

$$B_2 = \frac{\alpha I}{4\sinh(b/\lambda)}[e^{-y_3/\lambda} + fe^{y_3/\lambda} - e^{b/\lambda}(e^{y_1/\lambda} + fe^{-y_1/\lambda})]. \tag{B.11}$$

$$A_3 = -\frac{\alpha I}{4f\sinh(b/\lambda)}e^{-b/\lambda}[e^{y_2/\lambda} + fe^{-y_2/\lambda} - (e^{y_1/\lambda} + fe^{-y_1/\lambda})]. \tag{B.12}$$

$$B_3 = \frac{\alpha I}{4\sinh(b/\lambda)}e^{-b/\lambda}[e^{y_2/\lambda} + fe^{-y_2/\lambda} - (e^{y_1/\lambda} + fe^{-y_1/\lambda})]. \tag{B.13}$$

Here we have defined f by:

$$f = \frac{R - g/\lambda}{R + g/\lambda} \tag{B.14}$$

An expression for the fringing resistance R can be obtained rather easily if one assumes that the flux takes a circular path from one to the other face of the magnetic layer:

$$\frac{1}{R} = \frac{\mu_0 a}{\pi}\ln(1 + 2t/g) \tag{B.15}$$

It can be verified easily that for $R \to \infty$ i.e. for $f=1$ Eqs. (B.8) - (B.13) transform into Eqs. (B.2) - (B.7).

Appendix C Expression for the enclosed flux

As mentioned in section 6.4 in the calculation of the inductance the relevant flux enclosed by the current is not equal to the flux that crosses the inside area of the coil i.e. crossing the region between y_3 and y_2 (see Fig 6.6). This is because also flux crosses *through* the current conductors itself. To account for this effect we consider an infinitely small current element of width dy at position y located between y_1 and y_2. This element encloses a flux equal to $\Phi_2(y)$dy/l minus the flux that remains at a similar infinitely small element of the opposite conductor between y_3 and y_4. Here, dy/l is the factor taking into account that the contribution results from only a part of the conductor. Since the flux $\Phi_3(y)$ at the opposite conductor due to the first conductor can be neglected ($\lambda << a$) it follows immediately that the flux enclosed by the total coil is given by (see also [40]):

$$\frac{1}{4}\Phi_{encl.} = \frac{1}{l}\int_{y_1}^{y_2} \Phi_2(y)dy. \qquad \text{(C.1)}$$

Here, the factor four is a result of the fact that the coil consists of four indentically behaving conductors. Substitution of Eq. ( ) yields for the inductance L the expression:

$$L = 4\alpha + \frac{4\lambda}{ll}\left[A_2 e^{y_2/\lambda} - B_2 e^{-y_2/\lambda} - A_2 e^{y_1/\lambda} + B_2 e^{-y_1/\lambda}\right] \qquad \text{(C.2)}$$